

**PL-TR-96-2027**

**DEVELOPMENT OF IMPROVED GEOPHYSICAL  
IMAGING TECHNIQUES FOR ENVIRONMENTAL  
SITE CHARACTERIZATION**

**Robert J. Greaves  
Matthijs W. Haartsen  
Daria L. Kutrubes  
Jung Mo Lee  
David P. Lesmes**

**Steve Pride  
Weiqun Shi  
M. Nafi Toksöz  
Jie Zhang**

**Massachusetts Institute of Technology  
Earth Resources Laboratory  
Department of Earth, Atmospheric, and  
Planetary Sciences  
42 Carleton Street  
Cambridge, MA 02142**

**31 December 1995**

**Final Report  
1 July 1993–1 October 1995**

**Approved for Public Release; Distribution Unlimited**

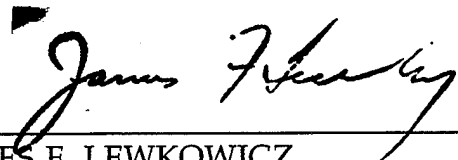
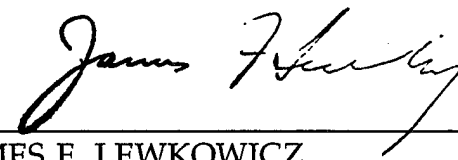


**PHILLIPS LABORATORY  
Directorate of Geophysics  
AIR FORCE MATERIEL COMMAND  
HANSCOM AFB, MA 01731-3010**

**19960524 005**

**DTIC QUALITY INSPECTED 1**

"This technical report has been reviewed and is approved for publication."

  
\_\_\_\_\_  
JAMES F. LEWKOWICZ  
Contract Manager  
\_\_\_\_\_  
JAMES F. LEWKOWICZ  
Director  
Earth Sciences Division

This report has been reviewed by the ESD Public Affairs Office (PA) and is releasable to the National Technical Information Service (NTIS).

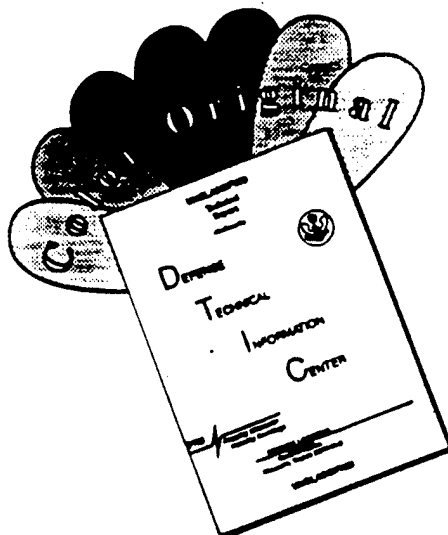
Qualified requestors may obtain additional copies from the Defense Technical Information Center. All others should apply to the National Technical Information Service.

If your address has changed, or if you wish to be removed from the mailing list, or if the addressee is no longer employed by your organization, please notify PL/IM, 29 Randolph Road, Hanscom AFB, MA 01731-3010. This will assist us in maintaining a current mailing list.

Do not return copies of this report unless contractual obligations or notices on a specific document requires that it be returned.

REPORT DOCUMENTATION PAGE			Form Approved OMB No. 0704-0188	
Public reporting burden for this collection of information is estimated to average 1 hour per response, including the time for reviewing instructions, searching existing data sources, gathering and maintaining the data needed, and completing and reviewing the collection of information. Send comments regarding this burden estimate or any other aspect of this collection of information, including suggestions for reducing this burden, to Washington Headquarters Services, Directorate for Information Operations and Reports, 1215 Jefferson Davis Highway, Suite 1204, Arlington, VA 22202-4302, and to the Office of Management and Budget, Paperwork Reduction Project (0704-0188), Washington, DC 20503.				
1. AGENCY USE ONLY (Leave blank)		2. REPORT DATE 31 DEC 1995	3. REPORT TYPE AND DATES COVERED Final Technical 7/1/93-10/1/95	
4. TITLE AND SUBTITLE Development of Improved Geophysical Imaging Techniques for Environmental Site Characterization			5. FUNDING NUMBERS F19628-93-K-0027	
6. AUTHOR(S) Robert J. Greaves      Jung Mo Lee      Weiqun Shi Matthijs W. Haartsen      David P. Lesmes      M. Nafi Toksöz Daria J. Kutrubes      Steve Pride      Jie Zhang			PE 62101F PR 7600 TA GN WU AD	
7. PERFORMING ORGANIZATION NAME(S) AND ADDRESS(ES) Earth Resources Laboratory Dept. of Earth, Atmospheric, and Planetary Sciences Massachusetts Institute of Technology 42 Carleton Street Cambridge, MA 02142			8. PERFORMING ORGANIZATION REPORT NUMBER 60454	
9. SPONSORING/MONITORING AGENCY NAME(S) AND ADDRESS(ES) Phillips Laboratory 29 Randolph Road Hanscom AFB, MA 01731-3010 Contract Manager: James F. Lewkowicz/GPE			10. SPONSORING/MONITORING AGENCY REPORT NUMBER PL-TR-96-2027	
11. SUPPLEMENTARY NOTES				
12a. DISTRIBUTION/AVAILABILITY STATEMENT Approved for Public Release; Distribution Unlimited			12b. DISTRIBUTION CODE	
13. ABSTRACT (Maximum 200 words) The objective of this research was to develop geophysical techniques for environmental site characterization: (1) a multi-offset ground penetrating radar profiling technique; (2) a nonlinear seismic refraction traveltime tomography; (3) a 3-D d.c resistivity tomography; and (4) an electroseismic method. The goals of this project were accomplished successfully and a large amount of field data were collected and modeled for characterizing actual environmental sites. Specifically, we demonstrate that performing GPR surveys with multi-offset geometry can improve the signal-to-noise ratio of subsurface radar reflections. We formulate a nonlinear seismic refraction traveltime tomography to precisely delineate bedrock topography that fits not only traveltime data but also the gradients of traveltime curves. A 3-D d.c. resistivity tomography technique is described for characterizing conductivity distribution in the shallow earth that can map surface measurements to the subsurface. Finally, we present theoretical and numerical techniques for modeling electroseismic waves from a point source by solving coupled equations of seismic wave propagation, fluid flow, electrical streaming current, and the resulting electromagnetic field. The usefulness of these four techniques for characterizing environmental sites is demonstrated by applications to field data from various sites. The new approaches and algorithms introduced for GPR, seismic refraction tomography, and 3-D resistivity inversion have received wide interest from both the scientific and user communities. The electroseismic method is still a new and potentially powerful technique for subsurface characterization. The theoretical modeling that was done is the first of its kind in this field.				
14. SUBJECT TERMS Ground penetrating radar; environmental site characterization; traveltime tomography; resistivity tomography; vertical electroseismic profiling			15. NUMBER OF PAGES 180	
			16. PRICE CODE	
17. SECURITY CLASSIFICATION OF REPORT UNCLASSIFIED	18. SECURITY CLASSIFICATION OF THIS PAGE UNCLASSIFIED	19. SECURITY CLASSIFICATION OF ABSTRACT UNCLASSIFIED	20. LIMITATION OF ABSTRACT SAR	

# DISCLAIMER NOTICE



THIS DOCUMENT IS BEST QUALITY AVAILABLE. THE COPY FURNISHED TO DTIC CONTAINED A SIGNIFICANT NUMBER OF COLOR PAGES WHICH DO NOT REPRODUCE LEGIBLY ON BLACK AND WHITE MICROFICHE.



## TABLE OF CONTENTS

List of Contributing Scientists .....	v
List of Previous and Related Contracts .....	v
Bibliography of Publications Totally or Partially Supported by the Contract .....	v
Preface .....	vi
Velocity Variations and Water Content Estimated From Multi-Offset Ground Penetrating Radar .....	1
Summary .....	1
1. Introduction .....	2
2. Multi-Offset Data .....	4
3. Normal Moveout Velocity Estimation .....	6
4. Stacked Radar Profiles .....	9
5. Radar Propagation Approximations .....	12
6. Interval Velocity and Water Content .....	15
7. Conclusions .....	25
References .....	27
High-Resolution Shallow Seismic Structure Imaging Using Grid-Based Nonlinear Refraction Traveltime Tomography .....	39
Summary .....	39
1. Introduction .....	40
2. Traveltime and Raypath Calculations .....	42
3. Inversion Method .....	43
4. Field Data .....	46
5. Conclusions .....	47
References .....	48

3-D D.C. Electrical Resistivity Inversion With Applications to Image the Aberjona Watershed .....	53
Summary .....	53
1. Introduction .....	54
2. Theory .....	60
3. Comparison of Stabilizing Functionals .....	64
4. Comparison of the Minimization Algorithm .....	67
5. Application fo Field Data: 3-D Resistivity Survey at the Aberjona Watershed, Woburn, Massachusetts .....	73
6. Conclusions .....	78
References .....	79
Electroseismic Waves From Point Sources in Layered Media .....	100
Summary .....	100
1. Introduction .....	101
2. Macroscopic Coupled Electromagnetic and Poro-Elastic Field Equations	104
3. Electroseismic Wavefield Description in an Isotropic Porous Layered Material .....	107
4. The Global Matrix Method .....	113
5. Point Forces in a Poro-Elastic Stratified Medium .....	123
6. Transformation Back to the Space Time Domain .....	129
7. Numerical Electroseismogram Examples .....	133
8. Conclusions .....	143
References .....	146
Appendix A: Electroseismic Field-Vector Formalism with Powerflow Normalized Eigenvectors .....	148
Tables .....	153

## List of Contributing Scientists

Robert J. Greaves, Graduate Research Assistant, Massachusetts Institute of Technology  
Matthijs W. Haartsen, Postdoctoral Associate, Massachusetts Institute of Technology  
Daria L. Kutrubes, Hager Geoscience, Waltham, Massachusetts  
Jung Mo Lee, Postdoctoral Associate, Massachusetts Institute of Technology  
David P. Lesmes, Postdoctoral Associate, Massachusetts Institute of Technology  
Steve Pride, Postdoctoral Associate, Massachusetts Institute of Technology  
Weiqun Shi, Graduate Research Assistant, Massachusetts Institute of Technology  
M. Nafi Toksöz, Professor of Geophysics, Massachusetts Institute of Technology  
Jie Zhang, Graduate Research Assistant, Massachusetts Institute of Technology

## List of Previous and Related Contracts

NIEHS Grant NIH-5P42ES0465-08, Geophysical site characterization of the Aberjona Watershed.  
EPA Grant CR821516-01-0, Four-dimensional electrical imaging of subsurface contaminants with applications to a controlled spill: a collaborative proposal.  
DOE Grant DE-FG02-93ER14322, Electro seismic characterization of lithology and fluid type in the shallow subsurface.

## Bibliography of Publications Totally or Partially Sponsored by the Contract

Greaves, R.J., J.M. Lee, D.P. Lesmes, and M.N. Toksöz, Lateral velocity variations and water content estimated from multi-offset ground-penetrating radar, *Geophysics*, 1995, accepted.  
Haartsen, M.W. and R.S. Pride, Modeling of coupled electro seismic wave propagation from point sources in layered media, *SEG Expanded Abstracts*, 1994.  
Haartsen, M.W. and M.N. Toksöz, Electro seismic waves from point sources in layered media, submitted to *J. Geophys. Res.*, 1995.  
Zhao, X., Effects of heterogeneities on fluid flow and borehole permeability, Ph.D. Thesis, Massachusetts Institute of Technology, 1994.  
Zhang, J. and M.N. Toksöz, High-resolution shallow seismic structure imaging using grid-based nonlinear refraction travelt ime tomography, *Proceedings of SAGEEP Annual Meeting*, 1996.  
Zhu, Z., C.H. Cheng, M.N. Toksöz, Polarization and particle motion of the flexural waves in an anisotropic borehole model, *SEG 65th Annual International Meeting Expanded Abstracts, BG3.8*, 89–92, Houston, Texas.

## PREFACE

The objective of this research project was to develop different geophysical techniques for environmental site characterization. The effort was concentrated in four areas: (1) a multi-offset ground penetrating radar (GPR) profiling technique; (2) a nonlinear seismic refraction traveltimes tomography; (3) a 3-D d.c. resistivity tomography; and (4) an electroseismic method. The goals of this project were accomplished successfully. In addition, a large amount of field data were collected and modeled for characterizing actual environmental sites.

In the first section, we demonstrate that performing GPR surveys with multi-offset geometry can improve the signal-to-noise ratio of subsurface radar reflections. Furthermore, we show that using a common midpoint (CMP) processing technique to model multi-offset radar data allows for the determination of dielectric properties, an interpretation of subsurface water content, and the conversion of radar traveltimes profiles to depth profiles.

In the second section, we formulate a nonlinear seismic refraction traveltimes tomography to precisely delineate bedrock topography that fits not only the traveltimes data but also the gradients of traveltimes curves. The use of the Tikhonov regularization method ensures that the inverse problem is well-posed for models with a large number of grids.

The third section describes a 3-D d.c. resistivity tomography technique for characterizing conductivity distribution in the shallow earth that can map surface measurements to the subsurface. We investigate the performance of different inversion algorithms for rapidly mod-

eling a large number of data points on a workstation and on an nCUBE parallel computer. A nonlinear conjugate gradient method performs consistently well.

Finally, the fourth section of the report is on the theoretical and numerical techniques for modeling electroseismic waves from a point source by solving coupled equations of seismic wave propagation, fluid flow, electrical streaming current, and the resulting electromagnetic field.

The usefulness of these techniques for characterizing environmental sites is demonstrated by applications to field data from various sites. The new approaches and algorithms introduced for GPR, seismic refraction tomography, and 3-D resistivity inversion have received wide interest from both the scientific and user communities. The electroseismic method is still a new and potentially powerful technique for subsurface characterization. The theoretical modeling that was done is the first of its kind in this field.



# **VELOCITY VARIATIONS AND WATER CONTENT ESTIMATED FROM MULTI-OFFSET GROUND PENETRATING RADAR**

## **Summary**

The common midpoint (CMP) processing technique has been shown to be effective in improving the results of ground penetrating radar profiling. When radar data are collected with the CMP multi-offset geometry, stacking increases the signal-to-noise ratio of subsurface radar reflections and results in an improved subsurface image. An important aspect of CMP processing is normal moveout velocity analysis. Our objectives are to show the effect of multiple velocity analyses on the stacked radar image and particularly, to demonstrate that this velocity information can also be used to determine subsurface water content.

Most GPR surveys are very limited in spatial extent and assume that within the survey range, radar velocity structure in the shallow subsurface can be adequately approximated by a single velocity function in data processing. In this study we show that variation in radar velocity can be quite significant and that the stacked profile improves as the number of velocity analysis locations is increased.

Interval velocities can be calculated from the normal moveout velocities derived in the CMP velocity analysis. With some reasonable assumptions about subsurface conditions necessary for radar propagation, interval velocity can be converted to an estimate of volumetric

water content. Therefore, by collecting GPR data in the multi-offset CMP geometry, not only is the radar profile improved but it also allows for an interpretation of subsurface variation in water content. We show the application of these techniques to multi-offset GPR data from the Chalk River test area operated by Atomic Energy of Canada Limited.

## 1. Introduction

Ground penetrating radar (GPR) is the recording of high frequency electromagnetic waves that have reflected from subsurface contrasts in dielectric constant. In low-loss media, ground penetrating radar is capable of producing high-resolution images of the shallow subsurface, compared to other surface electric or seismic geophysical techniques. Most commonly, GPR data is collected with a constant source-to-receiver offset. In the early development of GPR, multi-offset common midpoint (CMP) sounding was borrowed from reflection seismology as an effective technique for determining glacial ice velocities (Gudmandsen, 1971). As the use of GPR expanded to rock and soil surveys, multi-offset radar sounding has continued to be used primarily for velocity sounding at one or just a few points along a survey line. The advantages of determining velocity with this method are that it requires no prior knowledge of the subsurface, is not intrusive, uses the radar data acquisition system only and can determine a velocity profile anywhere within the survey. The disadvantage is that acquiring multi-offset data with current GPR systems is slow (compared to constant offset surveys), or impossible, for systems with fixed source-receiver offset.



Recent case studies have shown that when an entire GPR survey is acquired with the CMP geometry, multi-trace reflection seismic processing techniques can be used to improve the subsurface radar images (Fisher *et al.*, 1992; Gerlitz *et al.*, 1993). Fisher *et al.* showed the improvement of the subsurface image resulting from CMP stacking and migration. Our focus is on utilization of the subsurface velocity determined from the CMP pre-stack data. When the data are collected in the CMP configuration, normal moveout velocity analysis is used to derive a 2-D radar stacking velocity field. In our study, using the same data set as Fisher *et al.*, we show how the subsurface image, resulting from the stacking process, improves as the number of normal moveout velocity analyses, defining the stacking velocity field, increases. We then demonstrate a method for interpreting the velocity data in terms of subsurface volumetric water content.

In general, ground penetrating radar velocity decreases rapidly with depth (Davis and Annan, 1989). This is primarily a result of increasing water saturation with depth. Topp *et al.* (1980) derived an empirical relationship between dielectric constant of soil samples and the volumetric water content of the samples, where volumetric water content is the ratio of water volume to total sample volume. Using their relationship, or similar mixing formulas, we can estimate water content from dielectric constants where the dielectric constants are calculated from the interval velocities derived from normal moveout velocities. This interpretation step increases the potential uses of radar profiling in ground water studies and contaminant spill monitoring [see for example the variations in radar interval velocity caused by a controlled

contaminant spill described by Brewster and Annan (1994)]. Radar interval velocity can be used to estimate water content when the subsurface is sufficiently resistive to be treated as a low-loss media. This is a reasonable assumption where radar signals penetrate the subsurface to depths of meters or tens of meters. In partially saturated soils with constant porosity, water content may be interpreted as an indicator of saturation. In fully saturated soils, variations in water content can be interpreted as variations in porosity. The improvement to the radar image as a result of stacking GPR data collected in the CMP geometry, combined with interpretation of the subsurface velocity in terms of water content, should encourage the development of GPR systems capable of acquiring multi-offset data more efficiently.

## **2. Multi-Offset Data**

We obtained a multi-offset GPR survey from Sensors & Software, Inc., that was acquired at the Chalk River research area, operated by Atomic Energy of Canada, Ltd. The data were acquired in cooperation between Sensors & Software, Inc., the Atomic Energy of Canada, Ltd., and the UT-Dallas Geophysical Consortium. The data were collected with multiple source antenna to receiver antenna offsets, such that after rearrangement, 1800 CMP's spaced every 0.25 m were defined. The data were acquired using a pulse EKKO IV digital radar system with 100 MHz antennas. A detailed description of the acquisition geometry and the data recording parameters can be found in Fisher *et al.* (1992). For these data, each CMP gather has, on average, ten traces with offsets ranging from 0.5 m to 20.0 m. The standard

GPR data set would have only a single offset trace at each survey station. A rule-of-thumb estimate of the optimum offset, in a single offset survey, is that the antenna separation should be about 20% of the depth-of-interest (Annan and Cosway, 1992). In Figure 1, the minimum (0.5 m) offset trace profile from the Chalk River data set is displayed. This shows the data as it might have been collected in a single offset GPR survey at this site. The subsurface at the site consists of bedrock covered, primarily, by aeolian and fluvial sand deposits of glacial origin (Fisher *et al.*, 1992). In this profile we see a strong V-shaped reflector that appears to mark the base of the sedimentary section. Also, there is strong loss in reflection continuity between about 100–400 ns from CMP 900 to CMP 1800. Improvements to the radar image in these areas, in particular, are observed in the final CMP processed data profiles.

Figure 2a shows a number of CMP gathers with traces arranged in offset order from 0.5 m to 20.0 m within each CMP. Some of the approximately hyperbolic arrivals from reflections are clearly distinguished, but the signal-to-noise is low in this raw data. Preprocessing steps were applied to the data to prepare it for velocity analysis and stacking. The data were bandpass filtered (20–200 MHz), a top mute (in shot gather mode) was applied to remove the direct arrivals. Amplitude was multiplied by the square of sample travelttime as an approximate correction for geometric spreading loss. An f-k dip filter was applied to common shot gathers to remove some reverse dip events which may have been the result of scattering from off-axis locations. AGC (automatic gain control) scaling is used for display. Figure 2b shows the same CMP gathers after these processes have been applied. These

filtered data are used in the normal moveout velocity analysis.

### 3. Normal Moveout Velocity Estimation

Since the data in this survey were all collected with the CMP geometry, normal moveout (NMO) velocity analysis can be applied at any or all of the CMP's to define the subsurface velocity. The number of velocity analyses that are required depends on how strongly the radar velocity varies laterally. There is no rule or formula for determining an optimum number of velocity analyses for processing a CMP data set, so this parameter must be established by testing the data itself. In this example, we show how increasing the number of velocity analyses affects the final CMP stacked image.

There are a variety of schemes used in NMO velocity analysis (Yilmaz, 1987). We have used a semblance amplitude approach where the data in the CMP's are normal moveout corrected and stacked using a range of trial velocities. The amplitudes versus time over the whole range are then contoured and displayed as a velocity spectrum. The peaks of the amplitude mapping are chosen to define the 1-D velocity function at each CMP being analyzed. After a number of velocity functions have been defined, a 2-D velocity profile is created by interpolation. For a statistical method, like semblance mapping, the more traces there are in any individual CMP, and the larger the offset range (within the small spread approximation), the better the resolution in the velocity spectrum. In practice, the vertical resolution of NMO velocity analysis depends on the vertical spatial frequency of reflectors

strong enough to produce distinct semblance peaks. Usually we pick only the highest amplitude velocity spectra peaks for the traveltime versus velocity function. Therefore, the NMO velocity function will usually have fewer velocity layers defined than there are reflections observed in the data.

When the number of traces per gather is small and somewhat noisy, we expect the velocity spectra to have a relatively poor signal-to-noise ratio. In order to improve the picking resolution in the velocity spectra of the Chalk River data we combined the traces from twenty CMP gathers around each CMP chosen for velocity analysis. A typical velocity spectrum for a single CMP (no combination) is shown in Figure 3a. When the spectrum of the combined 20 CMP's is found, as shown in Figure 3b, the velocity peaks are much better resolved and NMO velocity can be picked with more confidence. One estimate of the error in the velocity pick is the width of the central semblance maximum. For example at 550 ns the peak has a width of 0.012 m/ns which gives an uncertainty in the velocity at this time of about  $\pm 8\%$ . To an extent, resolution in the spectra seems to improve with increasing traveltime. This is due in part to the fact that for near surface reflections, the further offset traces are muted and do not contribute to the analysis, so there are less data in the statistical analysis. Secondly, semblance values of the stack change more slowly as velocity increases. Since radar velocity is, in general, higher in the near surface, we expect less well-resolved peaks in the spectra of near surface reflections.

The NMO velocity analyses were performed at regular intervals along the profile. Figure

4 shows the interpolated NMO velocity fields as the number of velocity analyses is increased. Figure 4a is the simple flat layered profile that results when only one CMP (center) is analyzed. Velocity varies from about .125 m/ns near the surface to about .06 m/ns for deep reflectors. The basement and the overlying sediment interfaces generate strong reflections which are laterally continuous across the image and allow us to make reliable velocity estimates in the sedimentary section. However, the reflections observed below the basement reflector, probably originating from either fractures or foliations (Fisher *et al.*, 1992), are not sufficiently strong or laterally continuous to allow accurate velocity estimates to be made within the crystalline basement. The deepest reflectors for which velocity is estimated is at about 650 ns in the central portion of the data. The normal moveout velocity determined for the last strong reflector is presumed to mark the top of the crystalline basement. This velocity is used to do the NMO correction for all data below the last time pick. Figure 4b shows the 2-D velocity profile when velocity analyses at four CMP's are included. It is immediately clear that there is significant lateral velocity variation. As the number of velocity analyses increase (Figures 4c-4e), the 2-D NMO velocity field becomes even more heterogeneous, although the general background layering is still apparent. Lateral velocity variations of as much as 30% are encountered in a traverse across the more detailed velocity profiles.

## 4. Stacked Radar Profiles

Normal moveout corrections calculated from the NMO velocity field remove the offset dependence of the reflection traveltimes such that the data can be treated as zero offset traces. After the correction is made, the traces within each CMP are stacked to produce a single CMP trace. If the NMO correction is done with the correct velocity function, the stacked traces have an improved signal-to-noise ratio.

The NMO correction is based on the assumption that the subsurface sampled by each CMP can be adequately modeled as a sequence of horizontal layers with uniform interval velocity. Steeply dipping reflectors and strong velocity gradients test the applicability of the normal moveout and stack technique, but in general the method is sufficiently robust to improve data quality under most conditions. If lateral velocity variation is small enough, a single NMO velocity function can be used to calculate the moveout correction at all CMP's. However, where lateral velocity variation is significant, a variable NMO velocity field defined by functions at a number of CMP's must be applied to obtain the best results. In principle, an NMO velocity defined individually by velocity analysis for every CMP should yield the most accurate result. However, a spatial limit to significant (defined by the interpreter) lateral variation in NMO velocity is usually reached at some multiple CMP spacing.

NMO corrections were computed for the Chalk River data using each of the velocity fields in Figure 4. In Figure 5a we show the stacked profile when NMO is defined by the single velocity analysis (Figure 4a). Figure 5b is the stacked profile result when all 35 velocity

analyses (Figure 4e) are used. First, we compare these to the standard (no stack) profile shown in Figure 1. The stacked data profiles show a strong reduction in background noise as compared to single offset. Also, some deeper reflections, below the apparent channel bottom reflection, have been greatly enhanced, in particular, the reflector at about 625 ns from CMP 250 to CMP 1000. Note that when a velocity field is applied, the traveltime to reflectors changes slightly. This is a consequence of the normal moveout correction which is shifting arrival times as a function of the particular velocity field. As the detail in the applied velocity field is increased, the structure in the subsurface image becomes more accurate. For example, the strong reflector at 600 ns between CMP 200 and CMP 800, becomes more realistically upwardly concave in Figure 5b.

Comparing the single velocity stack (Figure 5a) to the multiple velocity analyses stack (Figure 5b), we observe that some deeper reflections occur down to 750 ns but the more clear improvement is in continuity of reflectors throughout the section. Overall, stacking with even just one velocity control point provides the majority of improvement in the deep reflector continuity and depth-of-imaging, compared to no stack. With increasing detail in the velocity field the primary improvement is in reflector continuity and time structure. The fact that the majority of the increase in depth of imaged reflectors occurs with the stack from even a single velocity analysis as compared to no stack, suggests that it is the multi-offset nature of the stack, in particular the far offsets, that provide the signal from the deeper reflectors.



As previously noted, the data between about 200 to 400 ns to the right of CMP 900 shows very few coherent reflectors in the standard GPR survey shown in Figure 1. In fact, the left half of the profile is quite different than the right half of the profile. The description of the survey acquisition by Fisher *et al.* (1992) shows that there is a bend in the survey line at this point. However, only a few CMP's at the turning point are affected by this change in geometry and does not explain the change in reflection character. With the NMO correction and stack, the region on the right changes dramatically, with a dramatic increase in the number of coherent reflectors. When only one velocity is applied (Figure 5a), this area of the data is still poorly resolved. However, when all velocity functions are included in the velocity description, the stack has improved continuity of a number of reflections from the left side of the data into the right side. Also, note that the deepest reflection on the right side, now appears to consist of a series of step-like events carved into the crystalline basement. Although not shown here, only small differences between the stack based on 18 velocity analyses and 35 were observed. This implies that lateral velocity resolution for these data is between 50 and 100 CMP's (12.5 to 25 m). We also note that in some portions of the profiles there are bursts of coherent steeply dipping noise that may be further evidence of scattering from inhomogeneities off the axis of the profile. These could be removed by applying a post-stack dip filter.

## 5. Radar Propagation Approximations

Radar propagation is fundamentally limited by the conductivity of the subsurface medium. Only in low-loss media can radar signals penetrate deep enough to provide a useful subsurface image. The conductivity of common soil and rock materials that can be penetrated to useful survey depths is less than 10 mS/m (Davis and Annan, 1989). Useful approximations for describing the propagation of radar signals can be found by considering the time harmonic solution of the equation

$$\nabla^2 E = \mu\sigma \frac{\partial E}{\partial t} + \mu\varepsilon \frac{\partial^2 E}{\partial t^2} \quad (1)$$

derived from Maxwell's equation for the case of a homogeneous isotropic medium.  $E$  is the electric field amplitude and the constants of proportionality,  $\varepsilon$ ,  $\mu$ , and  $\sigma$  are the electric permittivity, magnetic permeability and conductivity of the medium. The first term on the right side of the wave Eq (1) represents conduction of charge due to the applied electric field. The second term describes the displacement of charge due to the field.

A solution to Eq (1) of the form

$$E = E_0 e^{-kz} e^{i\omega t} \quad (2)$$

yields the dispersion relation

$$k^2 = i\mu\sigma\omega - \mu\varepsilon\omega^2. \quad (3)$$

The wavenumber,  $k$ , is complex and can be written as

$$k = \alpha + i\beta \quad (4)$$

where the attenuation constant

$$\alpha = \frac{\omega}{c} \sqrt{\frac{\kappa_e}{2} \left( \sqrt{1 + \tan^2 \delta} - 1 \right)} \quad (5)$$

and phase constant

$$\beta = \frac{\omega}{c} \sqrt{\frac{\kappa_e}{2} \left( \sqrt{1 + \tan^2 \delta} + 1 \right)} \quad (6)$$

are both real. The parameters,  $c$  and  $\kappa_e$  are the electromagnetic velocity in free space and the real part of the dielectric constant of the medium, respectively. The loss tangent  $\tan \delta$  is, for a plane wave propagating with the angular frequency  $\omega$ , the ratio of conduction current density to displacement current density.

$$\tan \delta = \frac{\sigma}{\omega \epsilon}. \quad (7)$$

Typically, relative susceptibility,  $\frac{\mu}{\mu_o}$ , is taken to be unity except where metallic objects or minerals are present in abundance (Telford *et al.*, 1976). If we take relative susceptibility to be unity, the solution to the equation can then be written as

$$E = E_o e^{-\alpha z} e^{i(\omega t - \beta z)} \quad (8)$$

which is the expression for a damped plane wave propagating with phase velocity

$$v = \frac{\omega}{\beta}. \quad (9)$$

In materials that are good conductors, displacement currents are negligible compared to conduction currents, and Eq (1) reduces to a diffusion equation, i.e., the fields do not

propagate as electromagnetic waves. For materials with low conductivity, and when the frequency of the oscillating electric field is high enough, the displacement current dominates over the conduction current and electromagnetic waves will propagate (Stratton, 1941). Where GPR is most effective, the loss tangent is very small and the diffusion term can usually be neglected. In this case, where  $\tan \delta \ll 1$ , the phase constant reduces to

$$\beta \approx \frac{\omega}{c} \sqrt{\kappa_e} \quad (10)$$

such that

$$v \approx \frac{c}{\sqrt{\kappa_e}} \quad (11)$$

and the medium attenuation,  $\alpha$ , can be approximated by

$$\alpha \approx 0.2 \times \frac{\sigma}{\sqrt{\kappa_e}} \quad (12)$$

where  $\sigma$  is in units of mS/m. At a depth of  $\frac{1}{\alpha}$  meters the field strength is reduced to  $\frac{1}{e}$  of its original amplitude. Care must be taken in interpreting this depth in terms of radar propagation distance. Kong (1990) refers to this as the penetration depth for slightly conducting media. He points out that it is frequency independent, even though we expect penetration to decrease at higher frequencies, and is effectively a volume attenuation due to wave scattering within the medium. It is tempting to refer to this penetration depth as 'skin depth', but it is preferable to reserve this nomenclature for the frequency dependent penetration depth that is found from the attenuation factor in highly conducting media. Practical definitions of

depth of penetration for GPR include not only the medium attenuation but also the acquisition system transmission and receiving characteristics and a frequency dependence (e.g., Davis and Annan, 1989; Daniels, 1989).

This discussion has centered on the time harmonic solution to the wave equation and as such has not considered that the material properties are also frequency dependent and therefore should be treated as complex numbers. In the frequency range of GPR, 10–1000 MHz, the frequency dependence of the dielectric constant and conductivity are small, in low-loss media, and can be taken to be constant for practical purposes (Davis and Annan, 1989). In our interpretation we treat the dielectric constant as real and related to the propagation velocity by the simple expression found in Eq (11). In making this approximation we recognize that frequency dependence as well as many other factors such as scattering loss, source/receiver antenna power and transmission characteristics, and ground coupling are not being accounted for. However, our assumption is that these factors change much more slowly than dielectric constant if reflections are observed in the data.

## **6. Interval Velocity and Water Content**

To interpret the NMO velocity field derived from the multi-offset data, it is necessary to calculate interval velocities and find the relationship of radar propagation velocity to other

geoelectric properties. Interval velocity  $v_{i,n}$  was calculated using the Dix formula (Dix, 1955).

$$v_{i,n} = \sqrt{\frac{v_{NMO,n}^2 t_n - v_{NMO,n-1}^2 t_{n-1}}{t_n - t_{n-1}}}. \quad (13)$$

This calculation was made difficult by the fact that radar velocity decreases with increasing traveltime. The Dix formulation does not preclude the case of velocity decreasing with traveltime, but we found that with decreasing velocity the numerator inside the square root of (13) can be negative if the traveltime interval is small or the NMO velocity change is large. Where this situation was encountered, we used the average interval velocity of laterally adjacent intervals. When the Dix formula is applied to calculated exact NMO traveltimes and moveout velocities for a radar velocity model, this problem is not observed. This implies that the Dix inversion, when applied to radar data, is very sensitive to noise in the velocity analysis. In consideration of this, the interval velocity was subjected to smoothing prior to calculation of dielectric constant and depth values.

The final step in our interpretation scheme is to relate the calculated radar interval velocities to water content. Interval velocity derived from reflection moveout curves is the group velocity. As discussed in the previous section, if we assume that the subsurface properties of the media penetrated by the radar signal do not vary much in the limited frequency range of the radar signal being used, then the group velocity can be taken to be approximately equal to the phase velocity. Then we can use the phase velocity Eq (11) to convert interval velocity to dielectric constant.

The dielectric constant of rocks and soils is very sensitive to the water content of the

sample. This is because the dielectric constant of water ( $\kappa_w \simeq 80$ ) is much larger than the dielectric constant of both mineral grains ( $\kappa_g \simeq 3 - 5$ ) and air ( $\kappa_a = 1$ ). Therefore, as the water content of a rock or soil sample increases, the dielectric constant of the sample increases and its velocity decreases. The net water content ( $\theta$ ) is equal to the product of the sample porosity ( $\phi$ ) and the saturation ( $S_w$ )

$$\theta = \phi S_w. \quad (14)$$

Therefore, the dielectric constant and velocity of a sample is determined by its porosity and saturation, and to a lesser degree, by the microgeometry of the sample.

Several mixing formulas have been both theoretically and empirically developed for the dielectric response of heterogeneous mixtures such as water saturated rocks (see, for example, Jackson and O'Neill, 1986; Dobson *et al.*, 1985). One such mixing formula is the CRIM (complex refractive index method) equation, which is often used in the interpretation of electromagnetic logging data (Schlumberger, 1991). The CRIM equation is a semi-empirical mixing law which relates the dielectric constant of the sample to the water filled porosity,  $\phi$ .

At radar frequencies, where  $\tan \delta \ll 1$ , the CRIM equation can be expressed as

$$\sqrt{\kappa_e} = \phi \sqrt{\kappa_w} + (1 - \phi) \sqrt{\kappa_g} \quad (15)$$

where  $\kappa_e$ ,  $\kappa_w$ , and  $\kappa_g$  are the dielectric constants of the sample, the pore water, and the dry mineral grains, respectively (Wharton *et al.*, 1980). Since  $\kappa_w$  and  $\kappa_g$  can be taken as known constants, the CRIM equation can be used to estimate the porosity of water-filled samples

from the measured dielectric constant of the sample.

In a similar fashion, the Hanai-Bruggeman (H-B) mixing formula can also be used to estimate the porosity of a water saturated rock or soil sample (see, for example, Sen *et al.*, 1981). The H-B formula is obtained by a theoretical effective medium calculation which expresses the complex dielectric response of the sample in terms of the complex dielectric response of the mineral grains and the pore fluids that make up the sample. At high frequencies, where  $\tan \delta \ll 1$ , the H-B equation yields the following implicit expression for the dielectric constant of the sample.

$$\kappa_e = \kappa_w \phi^m \left( \frac{1 - \frac{\kappa_g}{\kappa_w}}{1 - \frac{\kappa_g}{\kappa_e}} \right)^m. \quad (16)$$

This expression can be explicitly solved for the sample porosity of the fully saturated sample.

$$\phi_{HB} = \left( \frac{\kappa_w}{\kappa_e} \right)^{\frac{1}{m}} \left( \frac{\kappa_e - \kappa_g}{\kappa_w - \kappa_g} \right). \quad (17)$$

The cementation index,  $m$ , is a function of the grain shape and is typically found to vary between 1.5, for unconsolidated sands with well-rounded grains, to approximately 2.0 for well-cemented sandstones with oblate grain shapes (Jackson *et al.*, 1978).

Figure 6a shows the dielectric constant of a water saturated sandstone, predicted by the CRIM and H-B mixing formulas, as a function of the sample porosity. In these simulations, we have taken  $\kappa_w = 80$ ,  $\kappa_g = 4.5$  and, for the H-B formula, we have used cementation exponents of  $m = 1.5$  and  $m = 2.0$ . For all three curves, the dielectric constant increases with increasing sample porosity. At a fixed porosity, the H-B equation predicts a lower



dielectric constant for a well-cemented sandstone ( $m = 2.0$ ) than for a poorly cemented sandstone with round grains ( $m = 1.5$ ). The curve corresponding to the CRIM formula, which does not have an explicit dependence upon the sample microgeometry, is bounded by the two H-B curves.

Another way to vary the water content in a rock or soil sample is to vary the level of saturation. In this analysis, we consider a partially saturated rock as a three-phase mixture consisting of mineral grains, pore water, and air. The saturation,  $S_w$ , is the fractional volume of the pore space occupied by water, and therefore, it varies from  $S_w = 0.0$ , for an unsaturated sample, to  $S_w = 1.0$ , for a fully saturated sample. To predict variations in the dielectric constant of partially saturated samples, we need to use a three-phase mixing formula. Both the CRIM and the H-B formulations can be modified to predict the dielectric response of three-phase mixtures.

The CRIM formula is the electrical analog to the Wiley time-average equation, which is frequently used to predict the acoustic velocities of porous media (see, for example, Guéguen and Palciauskas, 1994). In these time-averaged equations the effective slowness (inverse of velocity) of the sample is obtained by adding the sample phases in series with each other. Therefore, a three-phase mixture of grains, water and air, results in the following CRIM type mixing formula.

$$\sqrt{\kappa_e} = \phi S_w \sqrt{\kappa_w} + (1 - \phi) \sqrt{\kappa_g} + \phi(1 - S_w) \sqrt{\kappa_a}. \quad (18)$$

The H-B effective medium theory can also be used to predict the effective dielectric response

of partially saturated rock or soil samples (Endres and Knight, 1992; Samstag, 1992). In this analysis, we follow the procedure of Samstag and Morgan (1991), in which the H-B mixing formula is employed twice; first, to compute the effective dielectric response of the water/air mixture, which fills the pore space, and second to compute the effective dielectric response of the total rock, which is obtained by mixing the mineral grains into the water/air mixture.

The first mixing of air into water gives

$$\kappa_{pore} = \kappa_w S_w^{m_1} \left( \frac{1 - \frac{\kappa_a}{\kappa_w}}{1 - \frac{\kappa_a}{\kappa_{pore}}} \right)^{m_1} \quad (19)$$

for the effective dielectric response of the pore ‘fluid’ mixture, where the exponent,  $m_1$ , is related to the shape of the air bubbles. The second mixing of the mineral grains into the water/air mixture gives

$$\kappa_e = \kappa_{pore} \phi^{m_2} \left( \frac{1 - \frac{\kappa_g}{\kappa_{pore}}}{1 - \frac{\kappa_g}{\kappa_e}} \right)^{m_2} \quad (20)$$

for the effective dielectric response of the partially saturated sample, where  $m_2$  is related to the shape of the mineral grains. In general, the geometric factors,  $m_1$  and  $m_2$ , in the first and second embeddings, may be different. Furthermore,  $m_1$  may also be a function of saturation (Endres and Knight, 1992; Morgan and Samstag, 1991). However, in this analysis we have assumed that  $m_1$  is independent of saturation, and equal to  $m_2$ .

Figure 6b is a plot of the H-B and CRIM simulations of the dielectric constant versus water saturation for a sample with 40% porosity. As in Figure 6a, the H-B simulations with  $m = 1.5$  (spherical inclusions) and  $m = 2.0$  (oblate inclusions), bound the dielectric response obtained from the three-phase CRIM mixing formula.

In practice, it is impossible to derive both the sample porosity and water saturation from just the dielectric constant of the sample. Topp *et al.* (1980), therefore, used a wide range of soil samples with varying degrees of water saturation to obtain the following empirical relationship between the measured dielectric response of the samples and the net water content ( $\theta = \phi S_w$ ).

$$\kappa_e = 3.03 + 9.3 \theta + 146.0 \theta^2 - 76.7 \theta^3. \quad (21)$$

We note that in the Topp *et al.* publication, an expression is also given for finding  $\theta$  in terms of a polynomial in  $\kappa_e$  (22).

$$\theta = -5.3 \times 10^{-2} + 2.92 \times 10^{-2} \kappa_e - 5.5 \times 10^{-4} \kappa_e^2 + 4.3 \times 10^{-6} \kappa_e^3. \quad (22)$$

In comparing crossplots (not shown here) of  $\kappa_e$  and  $\theta$  calculated from the two expressions, we found that for the range of water content,  $\theta = 0.02 - 0.4$ , the expressions are in good agreement, however at  $\theta = 0.0$  they differ by about one dielectric constant unit.

In Figure 6c, the dielectric response of the Topp equation (21), plotted as a function of water content, is compared to the H-B responses for the two-phase and three-phase mixtures plotted in Figures 6a and 6b, respectively. Recall that in the two-phase H-B simulations, the samples are fully saturated and the porosity is varied from 0 – 40% ( $\theta = \phi$ ), whereas, in the three-phase H-B simulations, porosity is held constant at  $\phi = 0.4$  and  $S_w$  is varied from 0.0 to 1.0 ( $\theta = 0.4 S_w$ ).

Note that at high water content, both the two-phase and the three-phase H-B simulations give comparable results, with the  $m = 1.5$  case giving larger dielectric constants than the

$m = 2.0$  case. At low water content, the two-phase H-B simulations converge to  $\kappa_e \simeq 2.5$  which corresponds to the dielectric constant of an unsaturated sandstone.

The Topp equation was obtained by fitting dielectric measurements made for a wide variety of soil types with varying porosities, water saturations, and cementation exponents. Therefore, it is not possible to make a direct comparison between the response of the Topp equation and the responses of the H-B model. However, it is interesting to note that at low water content, the Topp equation is in good agreement with the three-phase H-B model, with  $m = 2.0$ , and at high water content the Topp equation is in good agreement with the two-phase and three-phase H-B models, with  $m = 1.5$ . One possible explanation for this may be that in partially saturated samples, the microgeometry of the water/air mixture, that fills the pore space, may actually vary with the level of water saturation (Endres and Knight, 1992). The Topp curve may actually indicate that the cementation exponent for the water/air mixture in partially saturated samples decreases with increasing saturation.

In the following analysis, we use the Topp equation to transform the dielectric constants, obtained from the interval velocities, into estimates of the subsurface water content. As the curves in Figure 6c imply, the transformation of dielectric constant into water content is a function of the rock porosity, saturation and microgeometry, which are all unknown. Therefore, the transformation will not be exact, but the Topp equation should adequately reflect the relative changes in the subsurface water content. Note that, if the GPR data were collected at multiple frequencies, it might be better to use the Hanai-Bruggeman equation

which, in its complete form, is frequency dependent. It should also be noted that the actual measured property, interval velocity, changes more slowly with water content as velocity decreases. Since radar velocity in general decreases with depth, decreasing sensitivity of the inversion to variations in water content is expected to occur at greater depths.

After calculating the dielectric constants from the smoothed interval velocities using Eq (11), we use the Topp Eq (22) to estimate the subsurface water content shown in Figure 7. We also use the interval velocities to convert the profile from time to depth. Before making this conversion, the velocity estimates were binned into 20 ns intervals and then smoothed with a nine-point averaging window. The resulting water content depth section in Figure 7 clearly shows a zone of high water content in the central portion of the image. The bottom of the depth section reflects the irregular subsurface topography of the crystalline basement. Below the basement reflector, we were not able to estimate velocity and consequently could not estimate water content within the crystalline basement.

The hydrogeology of the Twin Lake Site at the Chalk River Nuclear Laboratories, where these data were acquired, has been extensively characterized with a large network of boreholes and several hydrogeological and geophysical studies (Thomas, 1989; Catto *et al.*, 1989; Kiley and Annan, 1989). Fisher *et al.* (1992) used stratigraphic information obtained from five boreholes, located in the vicinity of the radar survey, to interpret the processed radar data. An adapted version of their interpretation is shown in the lower part of Figure 7. The top stratigraphic layer is composed of unconsolidated aeolian sands predominantly medium-fine

in grain size with lenses of fine sand and silt stringers (indicated by the dotted lines in the figure). The bottom of the aeolian deposits (indicated by the dark solid line in the figure) is marked by a thin (0.5 m to 2.0 m) sand zone which is enriched in garnet and other heavy minerals. The sand layers below the garnetiferous sand are fluvial deposits, consisting of unconsolidated sand of fine to medium grain size, with a silty clay layer located toward the bottom left side of the sedimentary section. The unit below the silty clay layer was labeled as 'unknown' by Fisher *et al.* because, although it was observed in the radar, it was not penetrated by a borehole.

The radar survey was run along a road, which at CMP 805 changed direction and began to climb up a slight gradient. There is approximately 10 m of elevation gain between CMP 805 and CMP 1800. Topographic corrections have not been made to either the water content depth section or the geological cross-section. If topographic corrections were made to the water content section, the zone of high water content between CMP 805 and CMP 1800 would be pulled up by the elevation change. In this case, the high water content would show a downdip trend from right to left in the profile. This direction corresponds to the direction of regional groundwater flow (Killey and Annan, 1989). However, it is also apparent that there will still be some isolation of the high water content zone in the center of the cross-section that may be indicative of water table mounding where the profile, which runs from northwest on the left to southeast on the right, crosses between Twin Lake to the south and a wetland area to the north.

The unknown stratigraphic unit, identified by Fisher *et al.* in the radar profile, seems to have a higher water content than the overlying silty-clay unit. Since it has water content similar to the other fluvial sands in the section, it may also be a fluvial sand. Our water content depth section indicates a maximum depth to basement of approximately 30 m, whereas Fisher *et al.* indicate a maximum depth to basement of about 25 m. Killey and Annan (1989) report basement depths in this area ranging from 0 to 30 meters, making it impossible to be certain which depth calculation is correct. The discrepancy in basement depth between our analysis and that of Fisher *et al.* corresponds to about a 15% difference in average velocity to basement. We suspect that much of the error is in the interval velocities of the shallower portions of the section, where NMO velocity picking was most difficult. In any case, it is advisable to consider the water content values as showing relative changes rather than relying strongly on the absolute values.

## 7. Conclusions

Ground penetrating radar surveys collected with the CMP multi-offset geometry yield improved subsurface images over single offset surveys. We have shown that the CMP profile is improved as the number of velocity analyses is increased. This leads to the conclusion that lateral variation in the radar propagation velocity profile can be significant even over the limited range of a typical GPR survey. The CMP stacking process yields improved depth-of-imaging compared to a single offset survey while detailed velocity analysis yields

improvement to continuity of reflectors throughout the stacked profile.

In this study, we have attempted to connect the practical measurement of radar velocity from the multi-offset data with the theoretical and laboratory relationships between water content and dielectric constant. We have shown a practical approach to estimating water content from these velocities based on the assumption that in low-loss media, radar propagation velocity can be expressed as a function of the real part of the dielectric constant. We applied this method to the Chalk River multi-offset GPR data and calculated a water content cross-section in depth. Comparison of this result to published geologic and hydrogeologic descriptions of the survey area suggests that our water content depth section is indeed reasonable. Based on similarity of water contents, we suggest that the sedimentary unit described by Fisher *et al.* (1992) as 'unknown' is, in fact, a fluvial sand deposit.

Improvement to this approach could be made by increasing the number of source to receiver offsets recorded for each CMP which would improve the NMO velocity analysis. Also, we suggest that a test of this interpretation method should be done by measuring subsurface water content in an area while acquiring a multi-offset radar survey.

## Acknowledgments

The authors would like to thank Dr. Peter Annan of Sensors & Software, Inc. for permission to use these data and for several useful discussions about GPR. We also thank Prof. Dale Morgan for useful discussions about dielectric mixing laws.



This work was supported by Air Force Research Contract F19628-93K-0027, monitored by Phillips Laboratory and, for one of the authors (R.J.G.) by a Chevron Fellowship.

## References

- Annan, A.P. and Cosway, S.W., 1992, Ground penetrating radar survey design, *Proceedings of the Symposium on the Application of Geophysics to Engineering and Environmental Problems (SAGEEP)*.
- Brewster, M.L. and Annan, A.P., 1994, Ground-penetrating radar monitoring of a controlled DNAPL release: 200 MHz radar, *Geophysics*, 59, 1211-1221.
- Catto, N.R., Gorman, W.A., and Patterson, R.J., 1989, Quaternary sedimentology and stratigraphy of the Chalk River region, Ontario and Quebec, in Thomas, M.D. and Dixon, D.F., Eds., *Geophysical and related geoscientific research at Chalk River, Ontario, AECL-9085*, Atomic Energy of Canada, Ltd., 25-37.
- Daniels, J.J., 1989, Fundamentals of ground penetrating radar, *Proceedings of the Symposium on the Application of Geophysics to Engineering and Environmental Problems (SAGEEP)*.
- Davis, J.L., and Annan, A.P., 1989, Ground penetrating radar for high resolution mapping of soil and rock stratigraphy, *Geophys. Prosp.*, 37, 531-551.
- Dix, C.H., 1955, Seismic velocities from surface measurements, *Geophysics*, 20, 68-86.
- Dobson, M.C., Ulaby, R.T., Hallikainen, M.T., and El-Rayes, M.A., 1985, Microwave dielec-

- tric behaviour of wet soil - Part II: Dielectric mixing models, *IEEE Trans. Geosci. and Remote Sensing*, GE-23, 35-46.
- Endres, A.L. and Knight, K., 1992, A theoretical treatment of the effect of microscopic fluid distribution on the dielectric properties of partially saturated rocks, *Geophys. Prosp.*, 40, 307-324.
- Fisher, E., McMechan, G., and Annan, A.P., 1992, Acquisition and processing of wide-aperture ground-penetrating radar data, *Geophysics*, 57, 495-504.
- Gerlitz, K., Knoll, M.D., Cross, G.M., Luzitano, R.D., and Knight, R., 1993, Processing ground penetrating radar data to improve resolution of near-surface targets, *Proceedings of the Symposium on the Application of Geophysics to Engineering and Environmental Problems (SAGEEP)*, 561-574.
- Gudmandsen, P., 1971, Electromagnetic probing of ice, in Wait, J.R., Ed., *Electromagnetic Probing in Geophysics*, The Golem Press, Boulder, CO, 321-348.
- Guéguen, Y. and Palciauskas, V., 1994, *Introduction to the Physics of Rocks*, Princeton University Press.
- Jackson, P.D., Smith, D.T., and Stanford P.N., 1978, Resistivity-porosity-particle shape relationships for marine sands, *Geophysics*, 43, 1250-1268.
- Jackson, T.J. and O'Neill, P.E., 1986, Microwave dielectric model for aggregated soils, *IEEE Trans. Geosci. and Remote Sensing*, GE-24, 920-929.
- Kiley, R.W.D. and Annan, A.P., 1989, Stratigraphic information from impulse radar profiling

- over unconsolidated sand, in Thomas, M.D. and Dixon, D.F., Eds., *Geophysical and related geoscientific research at Chalk River, Ontario, AECL-9085*, Atomic Energy of Canada, Ltd., 295-306.
- Kong, J.A., 1990, *Electromagnetic Wave Theory*, John Wiley & Sons, Inc.
- Samstag, F.J. and Morgan, F.D., 1991, Dielectric and conductivity modeling of clay-bearing sandstones in the frequency and water-saturation domains, Texas A&M University (TAMU) Rock Physics Consortium, Annual Report.
- Samstag, F.J., 1992, An effective-medium model for complex conductivity of shaly sands in the salinity, frequency, and saturation domains, PhD thesis, Texas A&M University.
- Schlumberger, 1991, *Log Interpretation Principles/Applications*, Schlumberger Educational Services, Houston, Tx.
- Sen, P.N., Scala, C., and Cohen, M.H., 1981, A self-similar model for sedimentary rocks with application to the dielectric constant of fused glass beads, *Geophysics*, 46, 781-795.
- Sheriff, R.E., 1991, *Encyclopedic Dictionary of Exploration Geophysics*, 3rd Edition, Soc. Expl. Geophys.
- Stratton, J.A., 1941, *Electromagnetic Theory*, McGraw-Hill, Inc..
- Telford, W.M., Geldart, L.D., Sheriff, R.E., and Keys, D.A., 1976, *Applied Geophysics*, Cambridge University Press.
- Thomas, M.D., 1989, Geology of the region surrounding Chalk River Nuclear Laboratories, Ontario, in Thomas, M.D. and Dixon, D.F., Eds., *Geophysical and related geoscientific*

- research at Chalk River, Ontario, AECL-9085, Atomic Energy of Canada, Ltd., 7-15.*
- Topp, G.C., Davis, J.L., and Annan, A.P., 1980, Electromagnetic determination of soil water content: measurements in coaxial transmission lines, *Water Resources Research*, 16, 574-582.
- Wharton, R.P., Hazen, G.A., Rau, R.N., and Best, D.L., 1980, Advancements in electromagnetic propagation logging, *Soc. Pet. Eng., Paper 9041*.
- Yilmaz, Ö., 1987, *Seismic Data Processing*, Soc. Expl. Geophys.

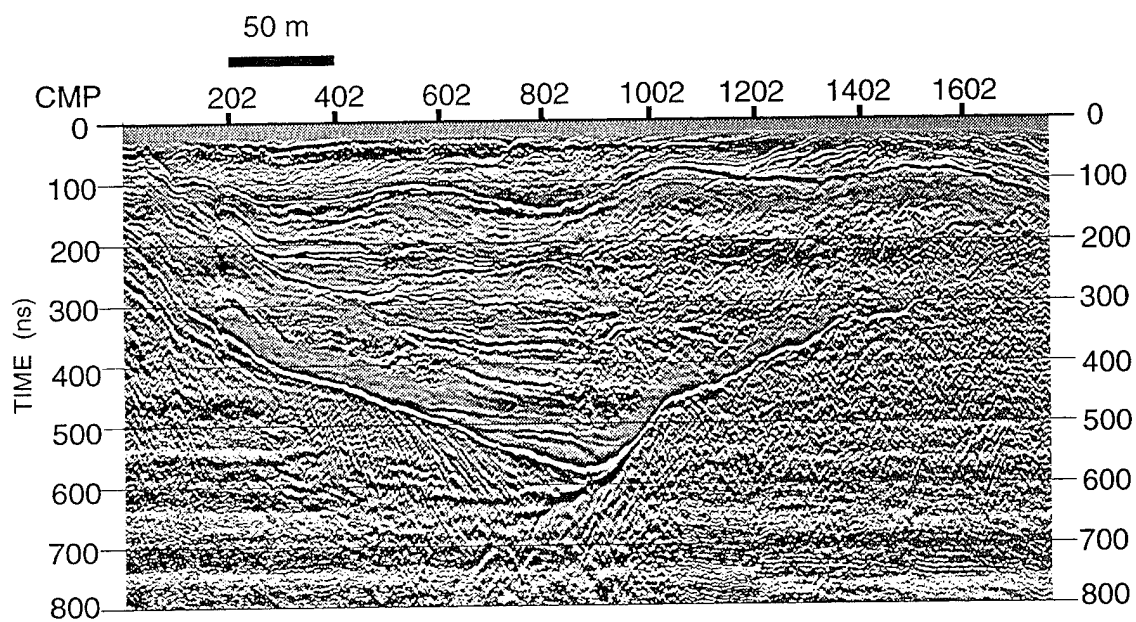


Figure 1: The minimum offset profile extracted from multioffset GPR data at the Chalk River test site. Each trace has a source to receiver offset of 0.5 m.

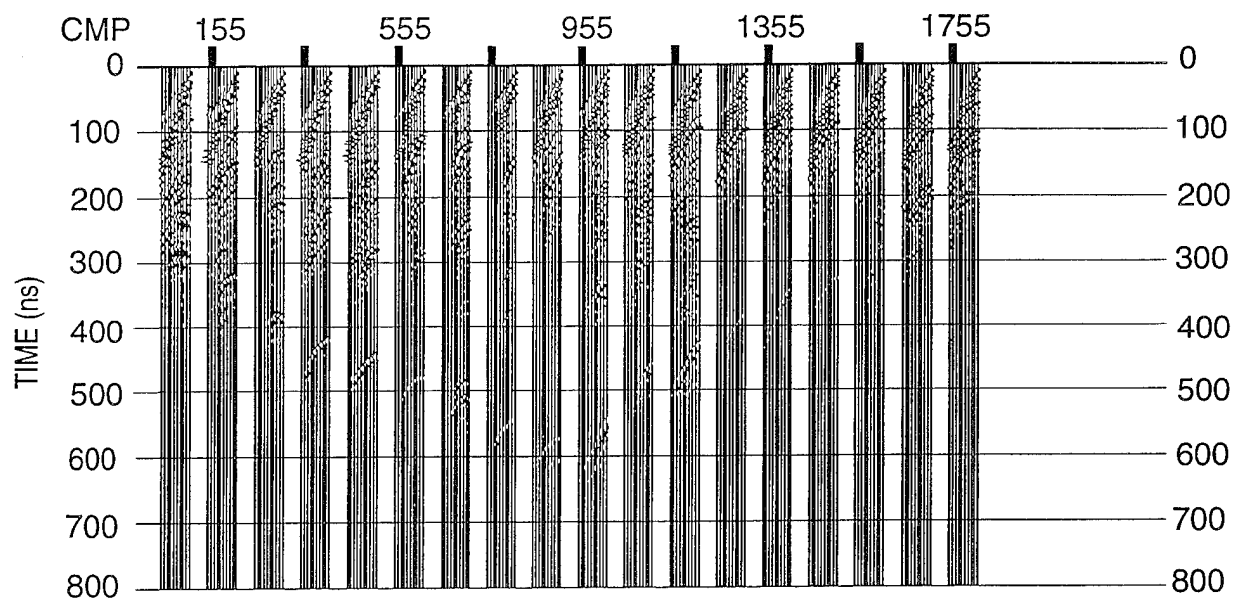


Figure 2a: Radar CMP gathers in offset order before preprocessing. Offsets vary from 0.5 m to 20.0 m within each CMP.

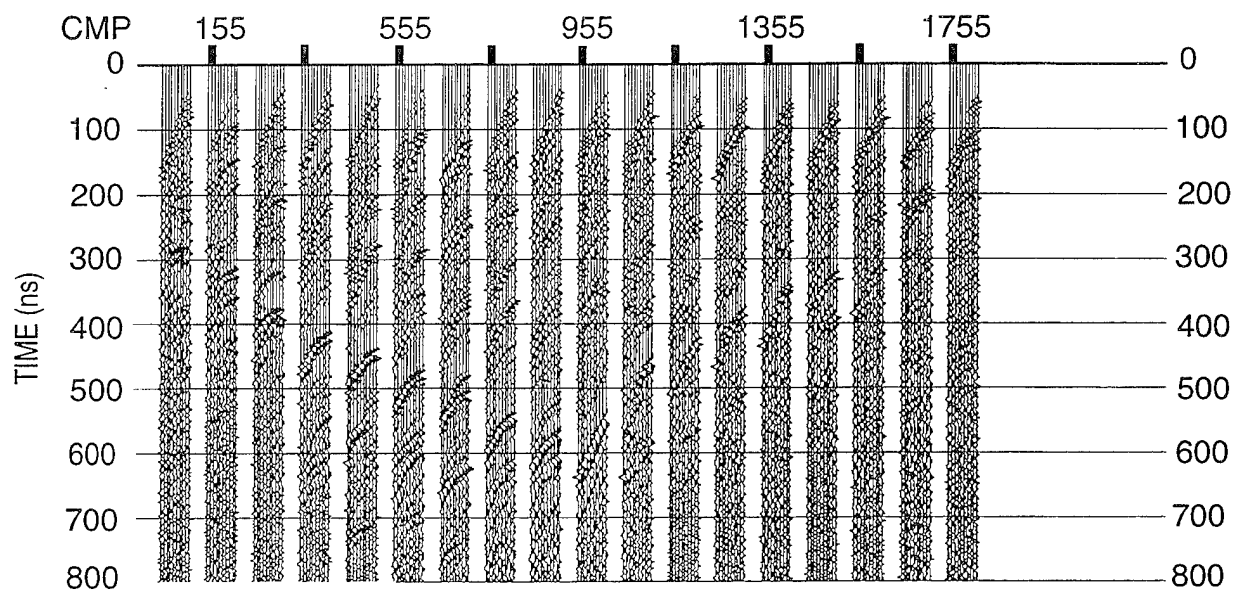


Figure 2b: Radar CMP gathers after preprocessing. Offsets vary from 0.5 m to 20.0 m within each CMP.

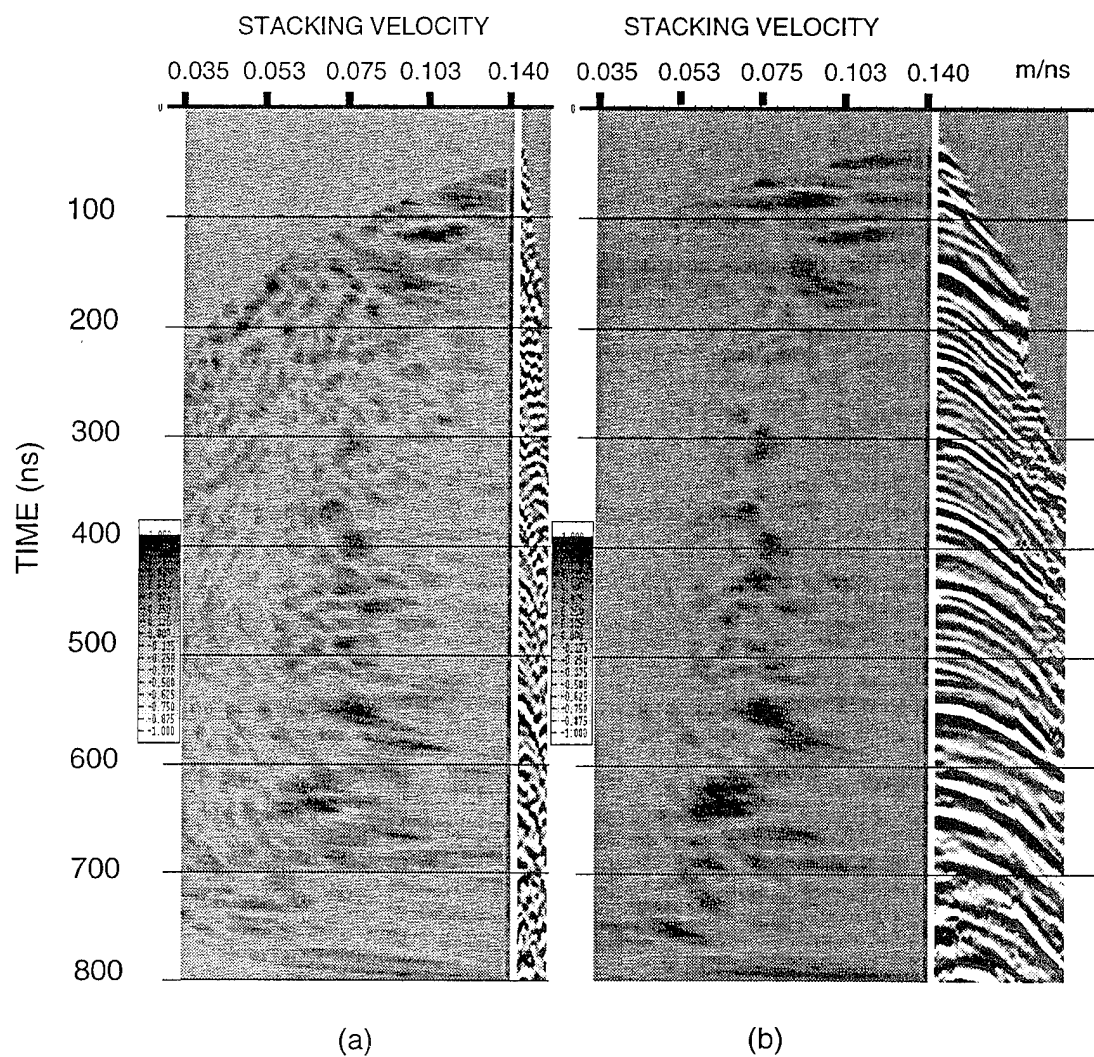


Figure 3: (a) Velocity spectrum of CMP 755. (b) Velocity spectrum of the combination of 20 CMP's centered on CMP 755.





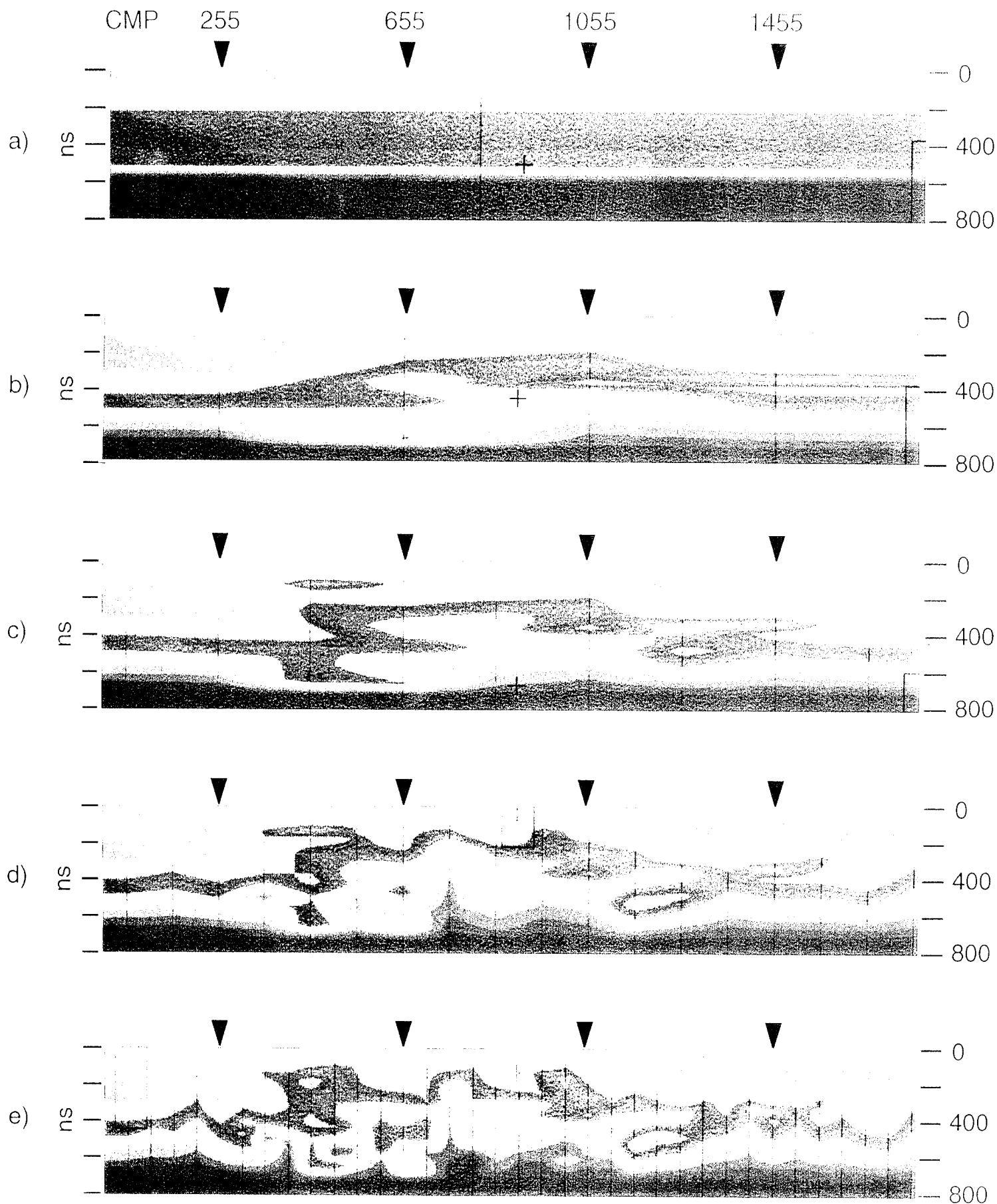


Figure 4: 2-D normal moveout velocity profile in travelt ime after analysis at (a) 1 CMP, (b) 4 CMP's, (c) 9 CMP's, (d) 18 CMP's, and (e) 35 CMP's.

0.12 0.05

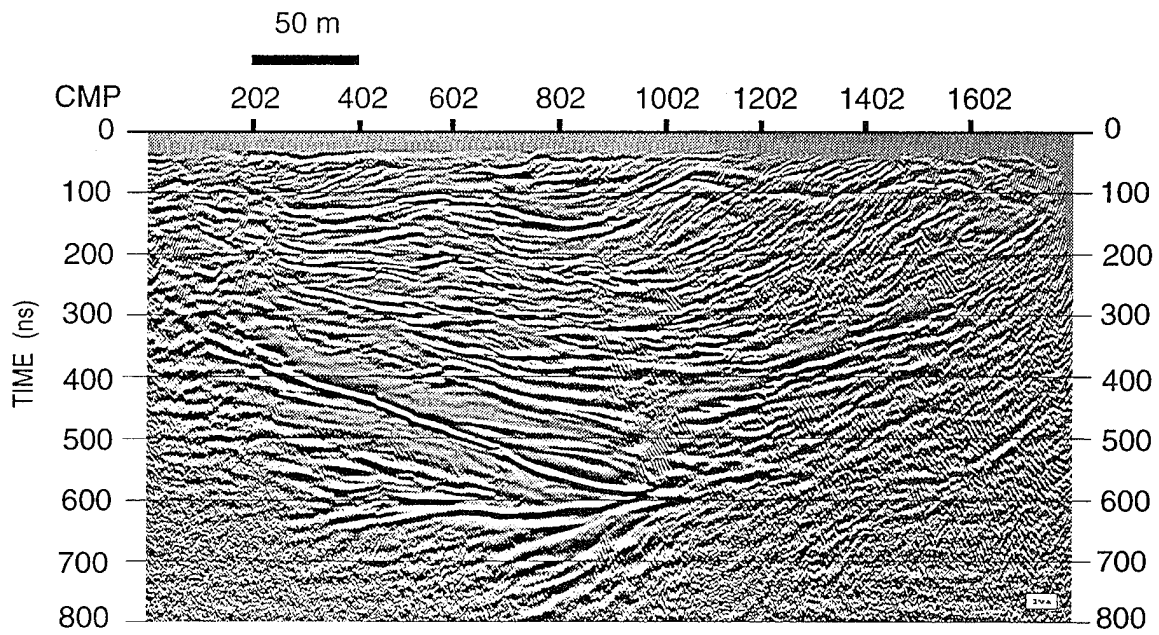


Figure 5a: CMP stacked radar reflection profile using the velocity profile from 1 CMP, corresponding to Figure 4a.

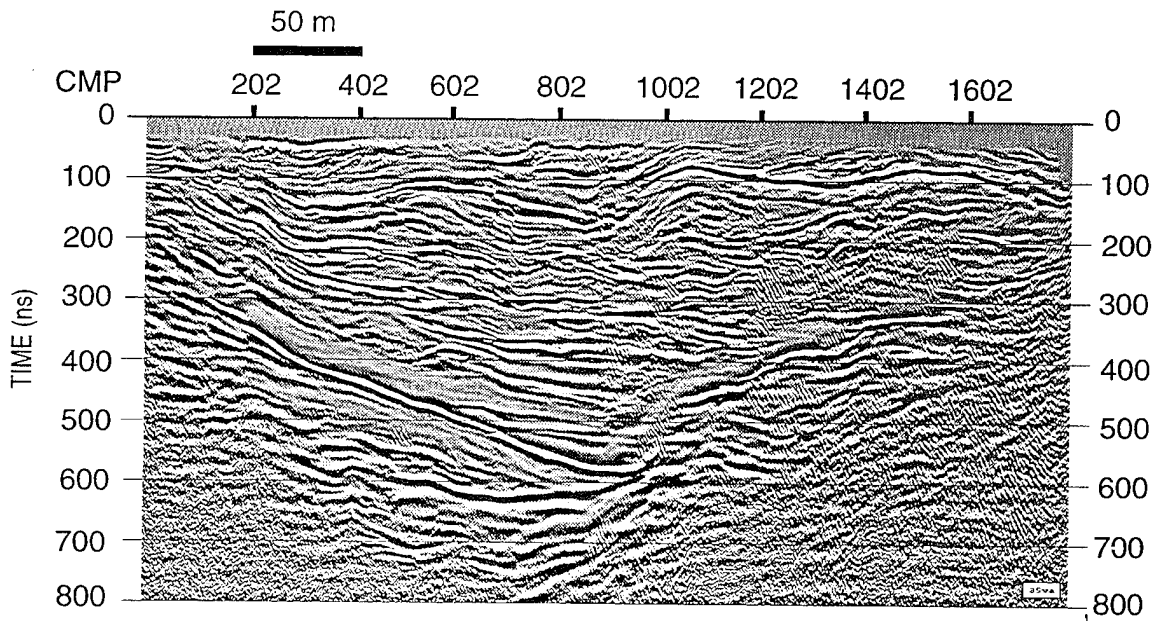


Figure 5b: CMP stacked radar reflection profile using velocity profile from 35 CMP's, corresponding to Figure 4e.

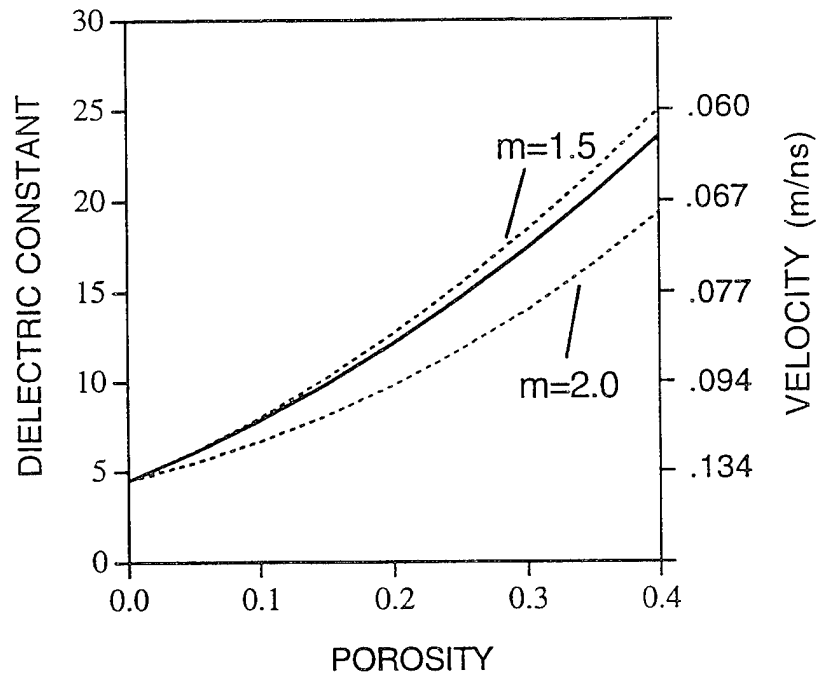


Figure 6a: Dielectric constant as a function of porosity ( $\phi$ ) as predicted by the CRIM (-) and Hanai-Bruggeman (...) two-phase mixing laws. The cementation exponents ( $m$ ) for the H-B simulations are indicated on the figure.

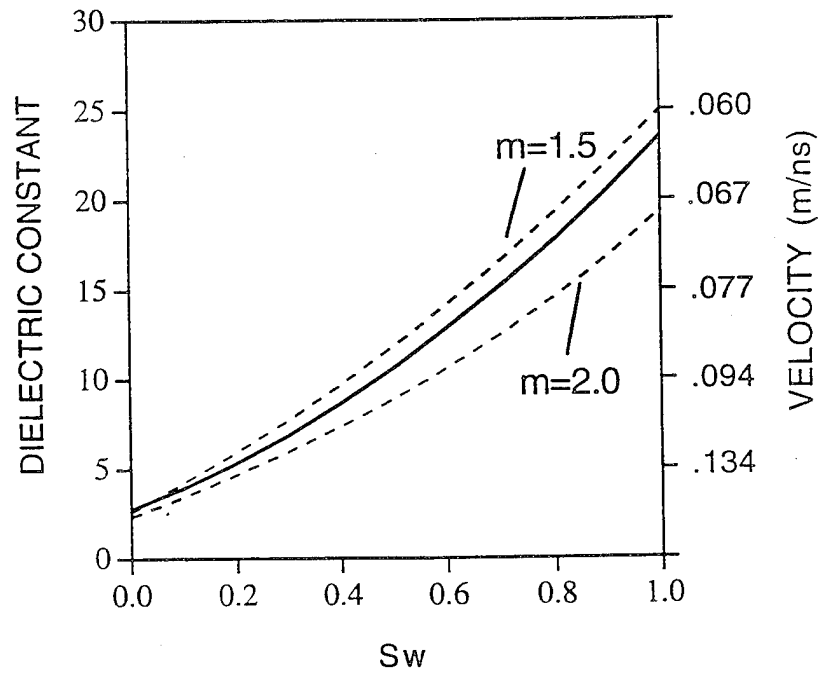


Figure 6b: Dielectric constant as a function of water saturation ( $S_w$ ) as predicted by the CRIM (-) and Hanai-Bruggeman (- -) three-phase mixing laws. The sample porosity is held constant  $\phi = 0.4$  and the cementation exponents ( $m$ ) for the H-B simulations are indicated on the figure.

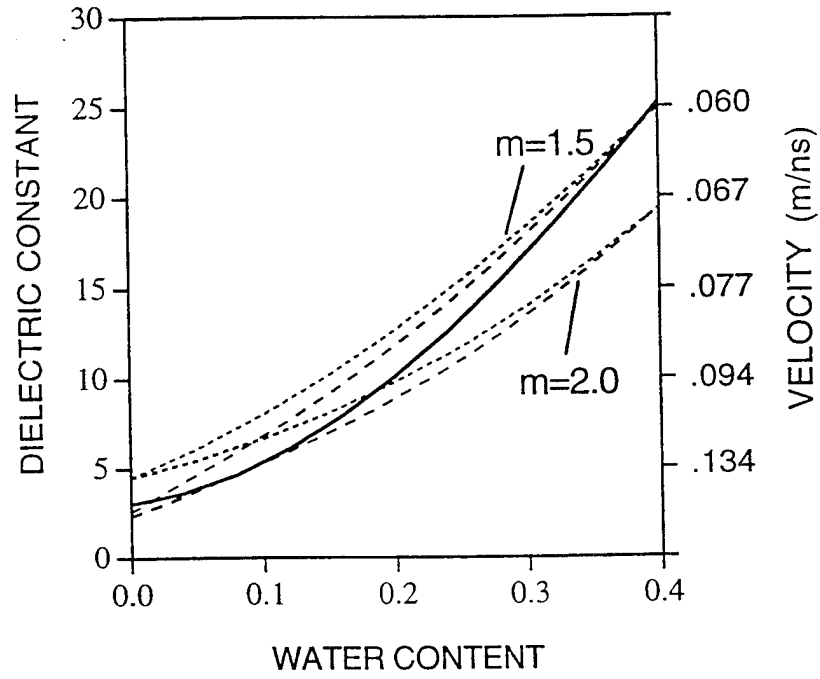


Figure 6c: Dielectric constant as a function of water water ( $\theta = \phi S_w$ ) as predicted by the Hanai-Bruggeman effective medium theory for both two-phase (...) and three-phase (- -) mixtures, and the empirical Topp *et al.* (1980) equation (-). The cementation exponents ( $m$ ) for the H-B simulations are indicated on the figure.

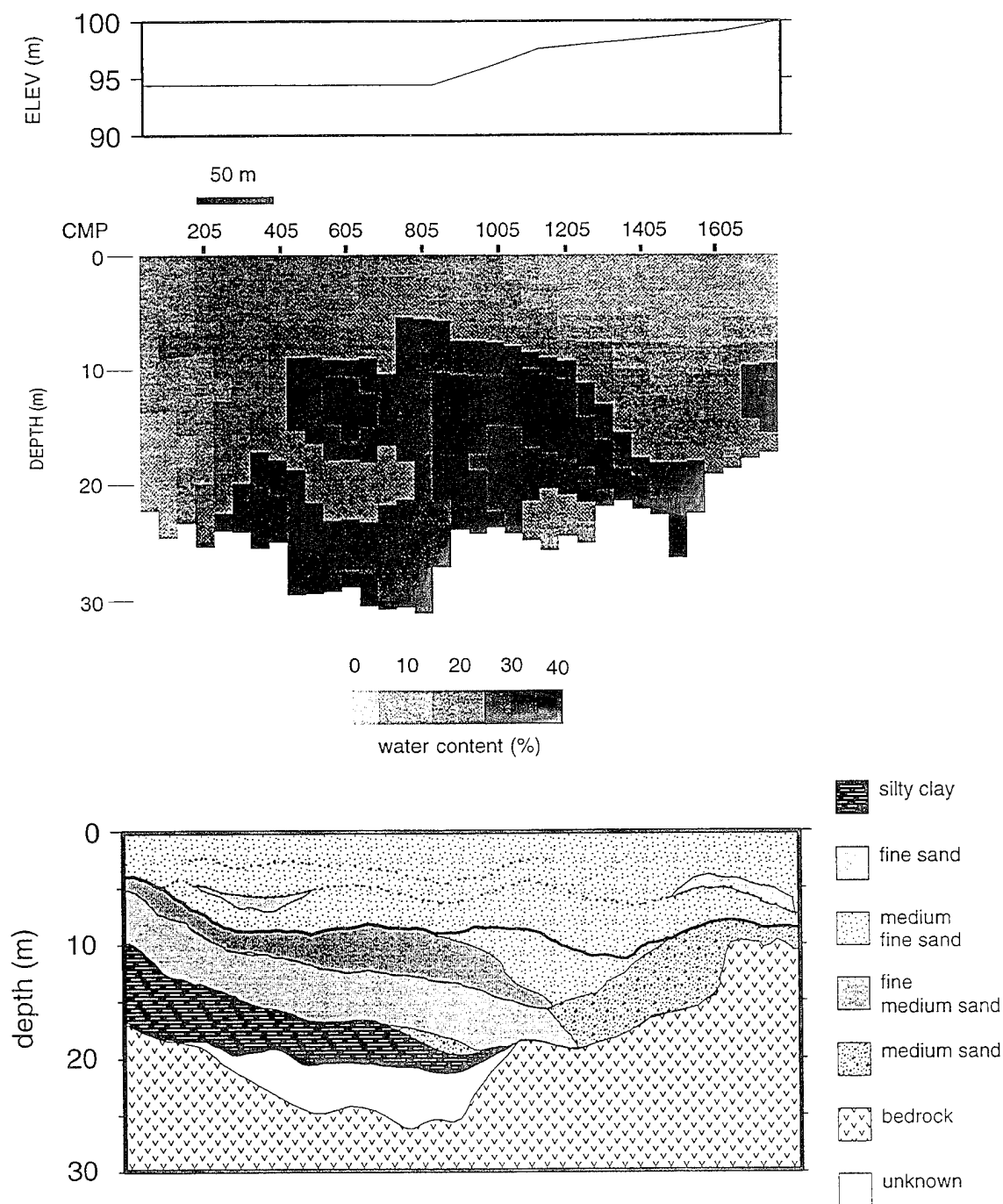


Figure 7: Comparison of the water content depth section (middle), estimated from radar interval velocities, to the geologic interpretation of Fisher *et al.* (1992). An approximate topography profile is shown at the top of the figure. In the geologic cross-section, the dotted lines indicate thin silt layers, and the dark solid line indicates a garnet sand which appears to define the contact between the aeolian sands near the surface and the deeper fluvial deposits.

# HIGH-RESOLUTION SHALLOW SEISMIC STRUCTURE IMAGING USING GRID-BASED NONLINEAR REFRACTION TRAVELTIME TOMOGRAPHY

## Summary

We develop a nonlinear refraction traveltime tomography technique that can rapidly reconstruct seismic velocity distribution in a large 2-D gridded model. For the traveltime and raypath calculations, we improve a graph-theoretical method by placing nodes on each grid boundary with an optimized distribution pattern. This method greatly reduces errors in traveltime and raypath calculations for complex velocity models. We pose a nonlinear objective function for inversion, which includes not only the traveltime misfit and model curvature roughness norm, but also traveltime gradient misfit norm. Our numerical experiments show that fitting the gradients of the traveltime curves in addition to the traveltime itself can better resolve the velocity contrasts across interfaces. We apply Newton's method to minimize the nonlinear objective function iteratively. The use of Tikhonov regularization allows to perform a global inversion and reconstruct the whole model with minimum model curvature roughness.

We apply this refraction traveltime tomography technique to image shallow bedrock topography at a coastal site near Boston, Massachusetts. We will demonstrate that performing nonlinear tomography can effectively reconstruct the subsurface image for complex velocity

structure.

## 1. Introduction

The seismic refraction method is a very useful tool for investigating problems at different scales, from environmental geophysics and oil exploration to crustal structure studies. Conventionally, seismic refraction data are acquired with “forward” and “reverse” geometry, and the interpretation involves reciprocity and some ideas similar to those in reflection migration. These include generalized reciprocal method (Palmer, 1980), wavefront reconstruction method (Aldridge and Oldenburg, 1992), and wavefield extrapolation method (Hill, 1987). However, all these methods can only be applied to areas where seismic velocity structures are relatively simple. Tomography methods, using an approach to calculate traveltimes and raypaths in a gridded model and applying an inversion technique to reconstruct seismic velocities, have been extensively studied and developed for crosshole geometry, but little has been done for refraction problems. Docherty (1992) demonstrates a 2-D refraction travel-time tomography that applies to a two-layer model for imaging shallow weathering layer. Hole (1992) iteratively solves a linearized backprojection problem with somewhat *ad hoc* smoothing constraints for areas in the model that do not contain any raypath. Ammon and Vidale (1993) conduct refraction traveltime tomography using a finite-difference method (Vidale, 1988) for traveltime calculations without rays involved, but have to repeat forward calculations for numerous times in order to obtain sensitivity information. Qin *et al.* (1993)

improved finite-difference method for better accuracy but with a higher cost of computation time. To avoid local minima in inversion, they apply an *ad hoc* horizontal smoothing operator in the model space and also downward extrapolate the gradient of the traveltime misfit function.

In this report, we introduce a different approach for rapidly and accurately conducting nonlinear grid-based refraction traveltime tomography. We account for the nonlinearity of the traveltime inversion problem by updating raypaths for perturbed model. Our forward traveltime and raypath calculations are performed using a graph-theoretical method based on Saito (1989) and Moser (1990) but with significant improvement in accuracy and efficiency. We pose a nonlinear objective function that is particularly meaningful for refraction traveltime problems, i.e., including the misfit norm of the gradients of traveltime curves, which contain independent slowness information in addition to the traveltime. As opposed to applying *ad hoc* model smoothing to keep the inversion stable, we solve the nonlinear traveltime tomography problem using the regularization method of Tikhonov. Tikhonov regularization takes a more explicit approach by damping spatial curvature of the model function and is applied to perform a global inversion in the sense of reconstructing the whole model. The inverse problem is solved by Newton's method (Tarantola, 1987), and conjugate gradient approach (Hestenes and Stiefel, 1952) is applied to rapidly update model changes in each inversion iteration. We demonstrate in real cases that this approach can produce a stable, unique solution of the nonlinear refraction traveltime problem. For a model with



250  $\times$  100 grids, and 12 sources and 24 receivers applied, tomography can be solved in about 7 min on a DEC alpha workstation starting from an arbitrary homogeneous model.

## 2. Traveltime and Raypath Calculations

For traveltime inversion, a forward modeling procedure is needed not only for the traveltime calculation but also for the raypath determination. Raypath tells model sensitivity to the traveltime measurements. One can use the finite-difference method to solve eikonal equation for traveltime calculation (Vidale, 1988; Qin *et al.*, 1993), but additional efforts are needed to find raypaths. We chose a graph-theoretical method that can calculate traveltime and determine raypaths simultaneously (Saito, 1989; Moser, 1990).

In the graph-theoretical method, nodes, where traveltime and raypaths are tracked, are often placed at the corners of the model grids (Saito, 1989; Moser, 1990; Mandal, 1992; Matarese, 1993) or regularly on the grid boundaries (Nakanishi and Yamaguchi, 1986; Moser, 1990). We chose the one which has nodes distributed on the grid boundaries and straight rays do not cross grid interfaces unless the local medium is homogeneous. However, instead of equally placing nodes on the grid boundaries, we optimize node distribution in the graph template so that the angle propagation error is greatly reduced. This is particularly important for refraction traveltime calculations since head waves are generated precisely at critical angles. For a discretized model, there are two independent errors involved in graph method: error due to finite grid size and error due to propagation angle sampling (Moser,

1990; Klimes and Kvasnicka, 1993). Decreasing grid size cannot reduce propagation angle error, and the angle error is associated with the largest angle difference that can be sampled. Therefore, minimizing angle differences for a given number of nodes simply reduces angle error. Figure 1 illustrates a graph template that contains two nodes on each grid boundary. The node distribution is optimized, and all the propagation angles are equal ( $22.5^\circ$ ). If the number of nodes on each grid boundary is more than two, then the optimized propagation angles cannot be exactly equal, but have an overall minimum difference.

In the graph method, the most time consuming job is the determination of shortest traveltimes among some selected nodes. We use an INTERVAL method which is about four to five times faster than the heap sorting algorithm (Klimes and Kvasnicka, 1993).

### 3. Inversion Method

We pose a nonlinear objective function which is physically meaningful for the refraction traveltimes tomography:

$$\Phi(m) = (1 - \omega) \|C_d(d - G(m))\|^2 + \omega \|D_x(d - G(m))\|^2 + \tau \|Lm\|^2 \quad (1)$$

$$= (1 - \omega) \|\bar{m}_d - \bar{m}_G(m)\|^2 + \omega \|\hat{m}_d - \hat{m}_G(m)\|^2 + \tau \|Lm\|^2, \quad (2)$$

$$\bar{m}_d \stackrel{def}{=} \frac{d}{l(m)} : \text{average raypath slowness data}, \quad (3)$$

$$\hat{m}_d \stackrel{def}{=} \frac{\partial d}{\partial x} : \text{surface apparent slowness data}, \quad (4)$$

where  $d$  is the traveltime data;  $G(m)$  is the calculated traveltime data for current model  $m$ .  $C_d$  is an operator that divides a traveltime by the corresponding ray length  $l$  and returns an average slowness  $\bar{m}_d$  along the raypath.  $D_x$  is a differential operator for traveltime with respect to the surface geophone spacing, and  $\hat{m}_d = D_x d$  returns the gradients of the traveltime-distance curves,  $L$  is a Laplacian operator for performing Tikhonov regularization,  $\tau$  is a smoothing trade-off parameter, and  $\omega$  is a weighting factor between data misfit norm and data gradient misfit norm. The inclusion of the second term in the objective function is particularly meaningful for refraction traveltime problem. It gives an  $l_2$  norm of the apparent slowness misfit, which is independent to the information from traveltime itself. In fact, picking reliable first arrivals from seismograms has to be based on not only the first break on the individual trace but also on the systematic moveout of a traveltime curve across all the traces. This is because individual trace may be contaminated by incoherent noise or significant changes in seismic wavelengths may occur due to site effects and attenuation. As one can see, all three terms as defined in the objective function (2) are explicitly related to model slowness in one way or another. The first term gives misfit of the average slowness between sources and receivers along raypaths; the second term represents misfit of apparent slowness along the surface; and the third term calculates the curvature roughness of the model slowness.

We minimize the nonlinear objective function (1) using Newton's method with some

modification:

$$((1-\omega)A_k^T A_k + \omega B_k^T B_k + \tau L^T L + \epsilon_k I) \Delta m_k = (1-\omega)A_k^T (\bar{m}_d - \bar{m}_G(m_k)) + \omega B_k^T (\hat{m}_d - \hat{m}_G(m_k)) - \tau L^T L m_k, \quad (5)$$

$$A \stackrel{def}{=} \frac{\partial \bar{m}_G}{\partial m} = \frac{1}{l(m)} \cdot \frac{\partial G}{\partial m}, \quad (6)$$

$$B \stackrel{def}{=} \frac{\partial \hat{m}_G}{\partial m} = \frac{\partial^2 G}{\partial m \partial x}, \quad (7)$$

$$m_{k+1} = m_k + \Delta m_k, \quad k = 1, 2, 3, \dots, N, \quad (8)$$

where  $A_k$  contains raypath lengths across each model grid,  $B_k$  contains the difference of raypath lengths in each model grid associated with the traveltimes at two adjacent geophones. We found that refraction traveltimes inversion behaves similar to many other nonlinear geophysical inversion problems in the sense that large nonlinearity occurs in the early inversion stage due to a poor starting model, and it approaches linearized when the model is close to the true solution. Therefore, we include a variable damping term  $\epsilon_k I$  in the left-hand side in Eq (5), and define  $\epsilon_k = \alpha \times rhs$ , where  $\alpha$  is an empirical parameter (about 0.01) and  $rhs$  is the rms misfit norm of the right-hand side in Eq (5). If the objective function is not minimized well and quite nonlinear, then  $rhs$  is large, and a large damping  $\epsilon_k$  is applied and small model updates are allowed. With the inversion proceeding further and  $rhs$  decreasing, a smaller  $\epsilon_k$  drives the convergence speed faster in the latter stage.

We apply Tikhonov regularization in our inversion as given by the third term in Eq (1) or (2), and  $L$  is defined as the second-order difference operator. For an allowed data misfit

norm level, there should be one unique trade-off parameter  $\tau$ . Therefore, experiments with different  $\tau$  should be performed in order to find the appropriate one. This selection will be based on the convergence curve of the data misfit norm versus iterations.

## 4. Field Data

At a coastal site near Boston, Massachusetts, a small-scale seismic refraction survey was conducted to map bedrock topography. The goal of this survey was to locate those areas where bedrock is deep so that construction of a new storm-drainage system may proceed without costly blasting. The environment at the working site was quite unusual as the survey area was covered by sea water during high-tide period, and exposed only for about 1 or 2 hours during the low tide each day. Further details of the project are reported by Kutrubes *et al.* (1996).

Figure 2 shows the seismic waveforms recorded from a forward shot and a reverse shot on line 1. Data from both shots show relatively delayed first arrivals between receivers 7 and 14, although the topography along line 1 is flat. Moreover, the amplitudes of these delayed first arrivals are relatively small. The evidence simply suggests that a low-velocity zone with strong seismic attenuation exists beneath receivers 7 to 14. It becomes more obvious when we placed sources (using hammer and air gun) at locations between the receiver 7 and 14, such effects were then observed at all the traces. Figure 3a displays traveltime data from 12 shots along line 1. Corrections for trigger time were made for a few shots based on

reciprocity. These traveltimes curves do not suggest simple velocity structure, rather, indicate complexity in the shallow seismic media. In another case, Figure 4 displays waveform data recorded from survey line 2 and Figure 3b shows traveltimes data from 12 shots. In contrast to line 1, this is a case that demonstrates the influences due to high-velocity anomalies in the shallow structure, *i.e.*, an intermediate velocity zone seats on the bedrock and outcrops the surface in the central area. Using these traveltimes data, we performed tomography studies with models consisting of  $250 \times 100$  grids. Our results are presented in Figure 5. The calculated traveltimes data corresponding to our final solutions are plotted in Figure 2 (grey dots). As one can see from these cases, although recorded data show complexities, the resolved bedrock topography is quite simple. The complexities are mostly due to the shallow velocity structures. These studies simply justify the importance of using nonlinear tomography approach for imaging the shallow earth.

## 5. Conclusions

In this report, we described an accurate and efficient approach for calculating traveltimes and raypaths for any velocity models. We introduced a nonlinear traveltimes tomography method that uses first arrivals and resolves velocities in a gridded model. Using Tikhonov regularization, we obtain a global solution by nonlinear inversion. Finally, the validity of our approach was proven by applications to real data.

## Acknowledgment

This work was supported by Air Force Office Research Contract No. F19628-93-K-0027, monitored by the Phillips Laboratory.

## References

- Aldridge, D.F. and Oldenburg, D.W., 1992, Refractor imaging using an automated wavefront reconstruction method, *Geophysics*, 57, 223–235.
- Ammon, C.J. and Vidale, J.E., 1993, Tomography without rays, *Bull. Seis. Soc. Am.*, 83, 509–528.
- Docherty, P., 1992, Solving for the thickness and velocity of the weathering layer using 2-D refraction tomography, *Geophysics*, 57, 1307–1318.
- Hestenes, M.R., and Stiefel, E., 1952, Methods of conjugate gradients for solving linear system, *J. Res. Natl. Bur. Stand.*, 49, 409–436.
- Hill, N.R., 1987, Downward continuation of refracted arrivals to determine shallow structure, *Geophysics*, 52, 1188–1198.
- Hole, J.A., 1992, Nonlinear high-resolution three-dimensional seismic travel time tomography, *J. Geophys. Res.*, 97, 6553–6562.
- Klimes, L. and Kvasnicka, M., 1993, 3-D network ray tracing, *Geophys. J. Int.*, 116, 726–738.
- Kutrubes, D.L., Zhang, J., and Hager, J., 1996, Comparison of conventional processing techniques and nonlinear refraction travelttime tomography for surveys at Eastern Mas-

sachusetts coastal site, in this proceeding.

Mandal, B., 1992, Forward modeling for tomography: triangular grid-based Huygens' principle method, *J. Seis. Exp.*, 1, 239–250.

Matarese, J.R., 1993, Nonlinear travelttime tomography, Ph.D thesis, Massachusetts Institute of Technology.

Moser, T.J., 1991, Shortest path calculation of seismic rays, *Geophysics*, 56, 59–67.

Palmer, D., 1980, The generalized reciprocal method of seismic refraction interpretation, SEG.

Qin, F., Luo, Y., Olsen, K.B., Cai, W. and Schuster, G.T., 1992, Finite-difference solution of the eikonal equation along expanding wavefronts, *Geophysics*, 57, 478–487.

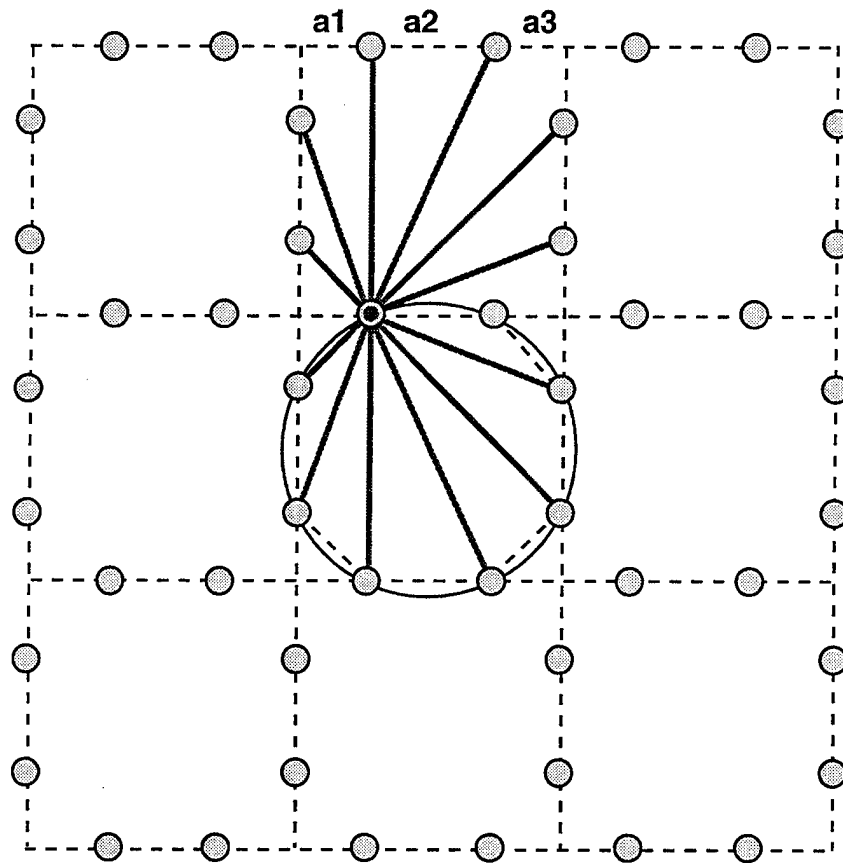
Saito, H., 1989, Traveltimes and ray paths of first arrival seismic waves: Computation method based on Huygens' Principle, Extended abstracts, 59th Ann. Internat. SEG Mtg., 244–247.

Tarantola, A., 1987, *Inverse Problem Theory*, Elsevier.

Vidale, J.E., 1988, Finite-difference travelttime calculation, *Bull. Seis. Soc. Am.*, 78, 2062–2076.



## Optimized Node Distribution



$$a1 = a3 = 0.29289dx$$

$$a2 = 0.41421dx$$

$$\theta = 22.5^\circ$$

Figure 1: An optimized graph template in which the differences of ray angles are minimized.

## Forward Shot

## Reverse Shot

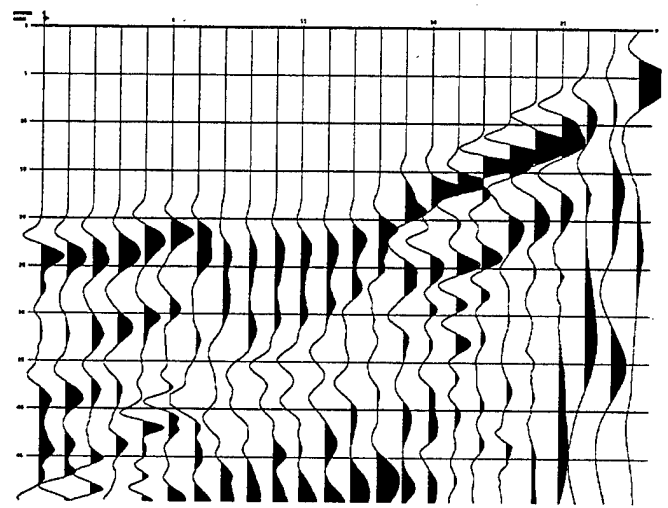
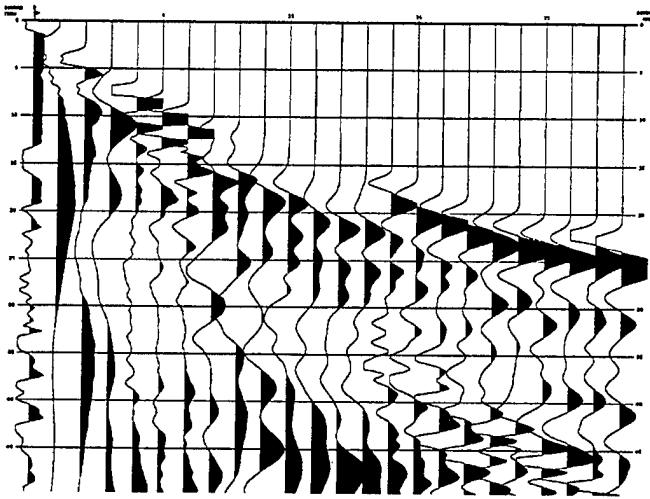


Figure 2: Waveform data from forward and reverse shots on line 1. The influences due to a shallow low velocity zone are shown between trace 7 and 14. Time interval is 5 ms.

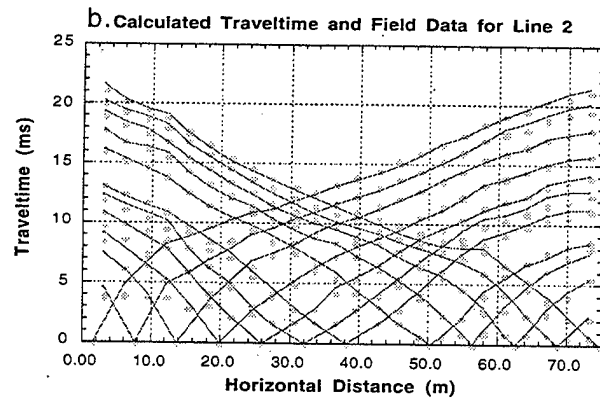
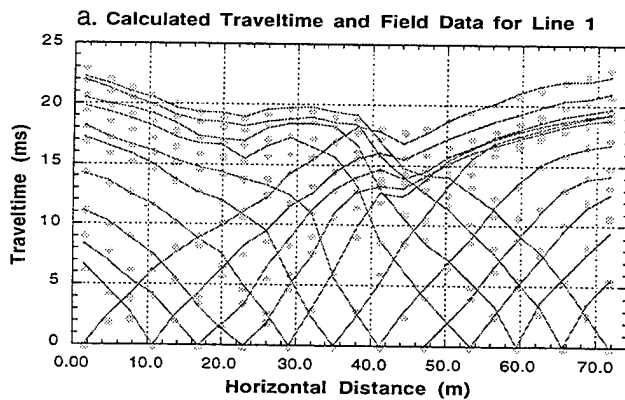
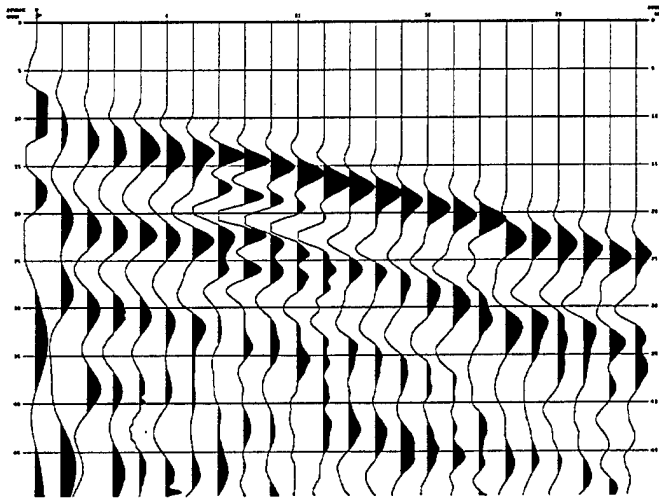


Figure 3: Field traveltime data (curves) from line 1 (a) and line 2 (b) and the calculated traveltimes (grey dots) for the resolved models shown in Figure 5.

### Forward Shot



### Reverse Shot

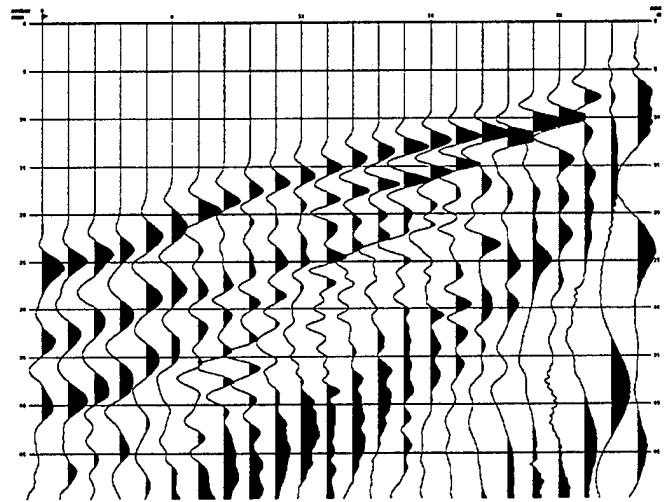
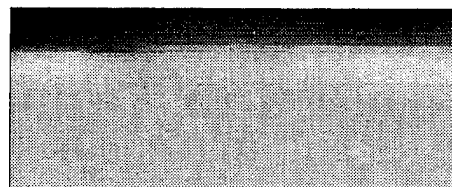


Figure 4: Waveform data from forward and reverse shots on line 2. The influences due to a shallow high velocity zone are shown in the central area. Time interval is 5 ms.

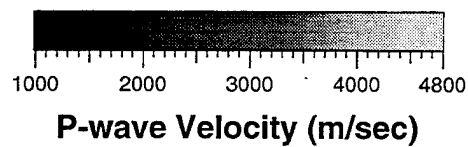
### Seismic Image on Line 1



### Seismic Image on Line 2



10 m



P-wave Velocity (m/sec)

Figure 5: Tomographic imaging results for refraction survey line 1 and line 2.

# 3-D D.C. ELECTRICAL RESISTIVITY INVERSION WITH APPLICATIONS TO IMAGE THE ABERJONA WATERSHED

## Summary

The task of d.c. electrical resistivity inversion is to solve for the subsurface resistivity distribution from the measurements of electrical potential on the surface of the earth or in boreholes. This problem is ill-posed in the sense that an infinite number of solutions to the inverse problem exist due to incomplete and uncertain data. To overcome the ill-posedness solutions must incorporate prior information or a smoothness constraint in order to be physically meaningful and stable against noise in the data. In this paper we investigate inversion algorithms based on Tikhonov's regularization method, which solves a minimization problem to find models that fit the data and also have minimum structure. We investigate different smoothness constraints and find that minimization of second-order spatial derivatives of the resistivity to be most effective, particularly in avoiding unstable features near the source and receiver electrode locations.

To implement the regularized inversion, we developed a numerical algorithm for minimizing the objective functional based on nonlinear conjugate gradient method. We investigate different pre-conditioners in the nonlinear conjugate gradient method and compare their efficiency with the commonly used Gauss-Newton method. By using a pre-conditioner based on the Hessian matrix of the objective function, the nonlinear conjugate gradient method

requires fewer iterations than the Gauss-Newton algorithm, however it may not be as efficient in terms of CPU time. Simpler pre-conditioners require more iterations but less CPU time since the computation of the Hessian is avoided.

We demonstrate our new algorithms on a large dipole-dipole data set collected at a groundwater contamination site in the Aberjona Watershed, Woburn, Massachusetts. The objective is to obtain a 3-D resistivity model of the subsurface to constrain hydrological models of the area. With this data set, the nonlinear conjugate gradient algorithm finds minimum structure models with approximately ten times less computation than the Gauss-Newton method. The results correlate well with other geophysical results at the site, including GPR sections and cone penetrometer logs.

## 1. Introduction

The d.c. electrical resistivity method is a principal geophysical exploration technique which has been used extensively for subsurface characterization. The implementation of the method consists of injecting current into the ground, measuring the electrical potential at intervals on the surface or in boreholes, and from those measurements deducing the subsurface resistivity distribution. Because the instrumentation is simple and the data acquisition is straightforward, the method is extremely cost effective. Important applications include mineral deposits prospecting (Keller, 1966; Burger, 1992), groundwater exploration (McNeill, 1990; Medeiros and Lima, 1990), geothermal studies (Burger, 1992) and engineering construction projects

(Bogoslovsky 1979; Shima, 1992). Recently, this method is being increasingly applied to environmental protection surveys owing to its non-invasive property. The applications include general hydro-geological mapping (Okko,1993), monitoring contaminated fluid migration (Blum, 1989; Van *et al.*, 1992; Spies *et al.*, 1995), mapping the extent of landfill areas (Carpenter *et al.*, 1990) and detection of contaminant plumes (Mazac *et al.*, 1990a; Buselli *et al.*, 1991).

The electrical resistivity of geological materials depends on mineralogy, clay content, pore fluid, permeability, conducting metal content, and other properties of the materials. The resistivity value of different geological materials can vary from  $10^{-4}\Omega.m$  (Pyrrhotite) to  $10^{14}\Omega.m$  (Dry Limestone), a range in values that may be the widest of any common physical property of earth materials. The electrical resistivity method is ideally suited for the task of detection of chemical contamination. The resistivity of some chemical contaminants may be much in contrast with the surrounding natural materials, this contrast makes the resistivity method the most sensitive in discerning contaminants from groundwater. Even when the resistivity image does not reveal the presence of chemical contaminants directly, it can provide valuable information on soil properties that control the transport of chemical contaminants.

The task of the d.c. electrical resistivity inversion is to solve for the subsurface resistivity distribution from the measurements of electrical potential on the surface of the earth or in boreholes. This is a difficult problem on many levels. One major difficulty encountered is

that the d.c. resistivity inverse problem is ill-posed. The ill-posedness comes from the fact that the number of measurements is always finite while the unknown resistivity is a continuous function which contains in principle an infinite number of variables. It is impossible to construct a solution that is stable and unique based on fitting data alone. Therefore solutions must incorporate some *a priori* information or be regularized in order to be physically meaningful and stable against the noise in the data. Since such *a priori* information or regularization is usually difficult to obtain directly from the geological reality, it is subjected to personal bias. Which *a priori* assumption or regularization criteria is thus appropriate for 3-D resistivity inversion remains a problem. The other major difficulty associated with the inversion is a result of the problem's nonlinear and numerically intensive nature. Since, in practice, a moderate 3-D resistivity model always involves a large number of model parameters and data set, the forward modeling entails solving a large matrix system. Further, because the observed electrical potential data are nonlinearly dependent on the resistivity parameters, iterative methods are needed to obtain the inversion solutions. Owing to this computational difficulty, methods for resistivity inversion were mostly restricted to 1-D (Inman, 1975; Parker, 1984) or 2-D (Pelton *et al.*, 1978; Tripp *et al.*, 1984; Smith and Vozoff, 1984; Narayan, 1990) earth models in the past decades, only few 3-D model inversions were found in recent literatures (Petrick *et al.*, 1981; Park *et al.*, 1991; Ellis and Oldenburg 1994; Zhang *et al.*, 1995).

In the past, most methods for d.c. resistivity inversion used coarsely parameterized models

(e.g., large layers or blocks) to make the problem well-posed. These solutions suppress significant structures and can hardly match the geological reality. A more objective approach that allows finely parameterized model was developed by Parker (1984) using bilayer expansion of Green's function on a 1-D uniform grided earth model. He introduced some smoothness constraints to eliminate the rapid unstable oscillation of the resistivity values that are caused by the non-uniqueness of the problem. Since the bilayer expansion was formulated based on a simple layered model, his approach was limited to 1-D earth models. Park and Van (1991) and Zhang *et al.* (1995) developed a 3-D resistivity inversion based on the maximum likelihood method (Tarantola and Valette, 1982; Madden, 1990) using statistical information to constrain the models. The method philosophically requires full statistical knowledge of the model parameters, however, in practice, such information is often unattainable, therefore the statistical inference was replaced by a uniform damping weighted on each model parameters which makes the method effectively the same as the conventionally damped least square method.

The approach presented in this report is based on Tikhonov regularization (Tikhonov, 1962). The method finds solutions by emphasizing the importance of the spatial correlation of the model parameters, it seeks spatially smooth (or "minimum structure" solutions of the inverse problem. The approach has been taken by Pilkington and Todoeschuck (1992) in cross-hole seismic tomography, by Scale *et al.* (1990) in refraction seismic profile, and by Jiracek *et al.* (1987) and deGroot-Hedlin *et al.* (1990) in 2-D magnetotellurics. These studies



indicate that the minimum structure approach is very useful in the case of highly non-unique problems, it suppresses model structures that are not essential in matching the observation and provides a lower bound on model complexity. In the case of the electrical resistivity method, we believe the minimum structure models are reasonable representations of the real earth because the diffusive nature of the electrical energy propagation can not resolve sharp resistivity contrasts.

When minimum structure models are sought, the inversion requires insertion of some smoothness constraints which are used to minimize the model roughness. One objective of this report is to investigate the effect of the smoothness constraints used in the Tikhonov regularization method. We will compare three commonly used smoothness constraints, i.e., the zeroth, the first and the second order spatial derivatives of model parameters, and will show that their effect on the stability of the solution rely on the behavior of the sensitivity function, which is a measure of how the electrical potential outputs change due to a small perturbation in the resistivity model parameters.

The difficulty of implementing such minimum structure regularization on a 3-D resistivity inversion depends, in part, on the numerical algorithm used for minimization. Because of the nonlinearity of the forward problem, iterative minimization schemes are needed to obtain solutions. The nonlinearity may also induce multiple local minima in the objective function used to find minimum structure models that fit the data, it is therefore necessary to repeat the iterative procedure by varying initial models for the minimization algorithm. Further,

due to the non-uniqueness and uncertainty of the problem, it is desirable to find the full set of acceptable solutions, or at least, find as many solutions that fit the data as possible. In doing so, one needs to repeat the iteration algorithm by varying the *a priori* model or the smoothness constraint. Current resistivity inversion algorithms are solved by an iterative linearized procedure that is often called the Gauss-Newton method (Tarantola and Valette, 1982; Park and Van, 1991; Zhang *et al.*, 1995). It starts from an initial model, then estimates a small perturbation of the current model based upon the Taylor expansion, this process is then repeated until the solution converges. This method suffers from slow convergence at the early stage of iterations. It has been shown that it may take tens of hours of CPU time on a high speed workstation to find a single inversion solution on a small (20x20x10) model (Ellis, 1995). A faster and robust algorithm is very desirable for extensively studying the uncertainty and the resolution of the problem and to benefit the 3-D resistivity method in future environmental and engineering application.

The second objective of this report is to investigate a more efficient algorithm based on the conjugate gradient method to solve the nonlinear minimization. We will show that with an appropriate pre-conditioner our algorithm requires less computer resources than the Gauss-Newton method and its superiority will become important when the initial model is far away from the true model.

We finally demonstrate the inversion algorithm by applying it to actual field data gathered using a dipole-dipole electrical resistivity survey at a superfund contamination site in the

Aberjona Watershed, Woburn, Massachusetts. The primary goal of that experiment is to construct a 3-D subsurface resistivity structure which can be used to augment hydrological models of the area in an effort to understand the transport mechanisms that have been involved in the contamination of groundwater. The nonlinear conjugate gradient algorithm, will be used to find minimum structure models, and its efficiency will be compared to the Gauss-Newton method. Our inversion results are correlated with other geophysical results at the site to examine their consistency and accuracy, and are found to be in good agreement.

## 2. Theory

### 2.1. 3-D Electrical Resistivity Forward Modeling

The d.c. electrical resistivity forward problem is the solution for electrical potential in an inhomogeneous medium governed by the equation

$$\nabla \cdot \left[ \frac{1}{\rho(x, y, z)} \nabla v(x, y, z) \right] = -j(x, y, z), \quad (1)$$

where  $\rho(x, y, z)$  is the resistivity [ $\Omega.m$ ] of the medium,  $j(x, y, z)$  is the current source density [ $Am^{-3}$ ], and  $v(x, y, z)$  is the electric potential [ $v$ ] subject to appropriate boundary conditions. On the surface of the earth, it is necessary to use Neumann boundary condition,  $\frac{\partial v}{\partial n} = 0$ , where  $n$  is the direction normal to the boundary. On portions of the boundary inside the earth, an exact boundary condition is not available but various approximate boundary conditions including Dirichlet and mixed boundary conditions (Day and Morrison, 1979; Zhang

*et al.*, 1995) can be used. For numerical simplicity, we assume that the model boundaries are far from the source and receiver so that a Dirichlet boundary condition,  $v = 0$ , can be used.

To solve (1) numerically, we use the transmission network analog developed by Madden (1972) to discretize the 3-D model into a network that consists of network nodes, boundary nodes, and impedance branches (Figure 1). Equation (1) is then approximated by a linear system of equations:

$$\mathbf{K}v = s \quad (2)$$

where  $v$  is a vector of the potentials at the network nodes,  $s$  is the current source vector, and  $\mathbf{K}$  is a real, symmetric, and positive-definite matrix which depends on the resistivities and dimensions of the network cells. Thus, the resistivity function  $\rho(x, y, z)$  is represented by discrete values  $\rho_{i,j,k}$ . To efficiently solve the forward problem (2), a linear conjugate gradient algorithm is used in this paper. Details of this solution can be found in Zhang *et al.* (1995).

## 2.2. Inversion Method

A practical d.c. electrical resistivity inverse problem may be defined as: Given a set of electrical potential measurements  $d = (d_1, d_2, \dots, d_N)$  made at the surface or in boreholes, determine as much information as possible about the subsurface resistivity. This may be written via an equation,

$$d = \mathbf{G}m + e \quad (3)$$

where  $m = m(\vec{x})$  is the unknown resistivity functional,  $\mathbf{G}$  represents the forward modeling operator which maps the model space to the data space, and  $e$  represents the error. Since the potential measurements can be made only at a finite number of locations, whereas the resistivity functional contains in principal an infinite number of variables, this problem is ill-posed. Solutions constrained only by the data alone can never be unique. It is necessary to incorporate *a priori* information in order to define a unique solution.

Classical remedies that advocate *a priori* preference into the model fall under two classes. One class assumes that the model parameters are random variables so that statistical information can be introduced to constrain the model. Important approaches include the following: the Bayesian inference (Duijndam, 1988); the stochastic inversion (Franklin, 1970), and the maximum likelihood method (Tarantola and Valette, 1982; Madden, 1990). The second class assumes some “regularity” properties of the solution such as a constraint on the spatial smoothness of the model parameter. This technique is known as the Tikhonov regularization (Tikhonov, 1962). It is important to note that the methods in the first class philosophically require full statistical knowledge of the model parameters. However, often in practice when such information is unavailable, these methods may impose some smoothness constraints which makes them effectively the same as the Tikhonov regularization.

Tikhonov regularization defines a solution of the inverse problem that fits the data but also that has minimum possible structures. In case of the highly non-unique problems, this technique is very useful because it provides the simplest, or “minimum structure” solutions

(Constable *et al.*, 1987). Solving for the smoothest model can avoid being misled by features that appear in the model but are not essential in matching the observation. Therefore, anomalies that appear in the model can only come from the data.

Using a least-square criterion, Tikhonov regularization defines a solution that is a joint minimization of data misfit and a "stabilizing functional":

$$\Psi = (d - \mathbf{G}m)^T \mathbf{R}_{dd}^{-1} (d - \mathbf{G}m) + \tau (m - m_0)^T \mathbf{L}^T \mathbf{L} (m - m_0) = \min \quad (4)$$

where  $\Psi$  is the objective functional to be minimized,  $\mathbf{R}_{dd}$  is data covariance matrix,  $\mathbf{L}$  is a linear operator,  $\tau$  is a positive number known as the regularization parameter, and  $m_0$  is a *priori* model.

The first term in the objective function measures the data misfit. It is the likelihood function when noise contaminating each observed data,  $e$ , has Gaussian normal distribution with zero mean and variance  $\mathbf{R}_{dd}$ . The second term defines the stabilizing functional as the regularization term which measures the spatial roughness of squared norm of  $\mathbf{L}(m - m_0)$ . In stochastic or the maximum likelihood inversion,  $m_0$  is taken to be a *priori* mean of  $m$  and  $\mathbf{L}$  is chosen such that  $(\mathbf{L}^T \mathbf{L})^{-1} = \mathbf{R}_{mm}$  is a *a priori* covariance of  $m$ . In a minimum structure approach,  $\mathbf{L}$  is a differential operator and  $m_0$  is taken to be a simple *priori* model. In practice it is desirable to vary  $m_0$  so that multiple solutions can be obtained.

Conventionally, the stabilizing functional has three options:

$$1, \quad \mathbf{L} = I, \quad (m - m_0)^T \mathbf{L}^T \mathbf{L} (m - m_0) = \int dx dy dz |m - m_0|^2 \quad (5)$$

$$2, \quad \mathbf{L} = \nabla, \quad (m - m_0)^T \mathbf{L}^T \mathbf{L} (m - m_0) = \int dxdydz |\nabla(m - m_0)|^2 \quad (6)$$

$$3, \quad \mathbf{L} = \nabla^2, \quad (m - m_0)^T \mathbf{L}^T \mathbf{L} (m - m_0) = \int dxdydz |\nabla^2(m - m_0)|^2. \quad (7)$$

It is not certain whether any of those options guarantees a well-posed minimization in 3-D resistivity inversion. In the next section we will discuss this issue.

### 3. Comparison of Stabilizing Functionals

Among proponents of the minimum-structure approach, there is no consensus on the best smoothing operator  $\mathbf{L}$  to use. Constable (1990) defined  $\mathbf{L}$  in terms of the first derivative, as in Eq (6). Scales *et al.* (1990) defined  $\mathbf{L}$  in terms of the second derivative, as in Eq (7). Ellis and Oldenburg (1994) defined  $\mathbf{L}$  as a combination of both the first and the second derivatives. To investigate their influences on the 3-D resistivity problem, we compare them theoretically and numerically.

We know that in Eq (4), when  $\Psi$  is minimized its first order partial derivative with respect to  $m$  is zero yielding,

$$\mathbf{A}^T \mathbf{R}_{dd}^{-1} (d - \mathbf{G}\hat{m}) + \tau \mathbf{L}^T \mathbf{L} (\hat{m} - m_0) = 0 \quad (8)$$

where  $\hat{m}$  is the solution at which  $\Psi(\hat{m})$  is minimized.  $\mathbf{A}$  is the sensitivity operator, or Fréchet derivative. For a discrete model,  $\mathbf{A}$  is the matrix

$$\mathbf{A}_{ij} = \frac{\partial G_i}{\partial m^j} \quad (9)$$

which measures how data changes at the  $i$ th receiver to a change of  $j$ th resistivity. Park *et al.* (1991) derived that the sensitivity matrix is given by the inner product of the current density ( $J_s$ ) from a point source at the transmitter and the current density ( $J_r$ ) from a point source at the receiver integrated over the perturbed volume,

$$\mathbf{A}_{ij} \sim \int_V J_s \cdot J_r d^3 \vec{x}. \quad (10)$$

In the 3-D problem, since the current distribution from a point source approaches infinity at the source, this sensitivity function has singularities at the location of source and receivers. Any small perturbation in the data will result in a large variation in the model space. This aspect of the physics must be accounted for in the regularization method.

Using Eq (8), we obtain the following relationship between the regularized solution model  $\hat{m}$  and the sensitivity matrix  $\mathbf{A}$ ,

$$\mathbf{L}^T \mathbf{L} \hat{m} = \mathbf{L}^T \mathbf{L} m_0 + \tau^{-1} \sum_i \mathbf{A}_0 \mathbf{R}_{dd}^{-1} (d - \mathbf{G} \hat{m}) \quad (11)$$

Therefore, when  $\mathbf{L}$  is an identity, the solution model  $\hat{m}$  equals  $m_0$  plus a linear combination of the sensitivity matrix multiplied by the data residue. When  $\mathbf{L}$  is the first order spatial derivative operator, the Laplacian of  $\hat{m}$  is a linear combination of the sensitivity matrix multiplied by the data residue. When  $\mathbf{L}$  is the second order spatial derivative operator, the Laplacian squares of  $\hat{m}$  is a linear combination of the sensitivity matrix multiplied by the data residue. To test which choice of the stabilizing functional yields a stable solution, we design a simple synthetic test problem.



The model is a conductive block ( $1\Omega.m$ ) buried in a homogeneous half space ( $100\Omega.m$ ). The model is discretized into  $21 \times 21 \times 15$  elements with 10 m spacing. The ( $1\Omega.m$ ) conductive block is discretized into  $7 \times 7 \times 3$  elements. 25 receiver electrodes are placed on the surface, among which nine of them are also used as current electrodes. A total of ( $9 \times 24 = 216$ ) observations are produced by forward modeling and 3% random Gaussian noise is added to the data.

Before investigating the three stabilizing functionals, the amount of smoothing done by each stabilizing functional needs to be justified. Previous studies (Backus and Gilbert, 1970; Parker, 1984) indicate that when noise contaminates the data there is a trade-off between the data misfit and the model roughness. By varying the regularization parameter  $\tau$ , a trade-off curve (Figure 3a) is generated using stabilizing functional (7) as an example. Three points— $\tau_1$ ,  $\tau_2$ , and  $\tau_3$ —are selected from the curve and their associated models are reconstructed and shown in Figure 3b. It is found that when the model is too smooth (when  $\tau = 5.5$ ), it cannot fit the data very well ( $\chi^2 = 275$ ). As  $\tau$  is lowered ( $\tau = 1.1$ ), the model has a smooth structure and provides a better reconstruction ( $\chi^2 = 176$ ). Over-fitting data ( $\chi = 130$  at  $\tau = 0.1$ ) results in a rough model which contains incorrect surface anomalies. In general, if data contains the random Gaussian noise, the expected value of  $\chi^2$  equals to the number of independent data, therefore choosing to fit  $\chi^2$  to the number of independent data is an optimum choice.

In our case, we fit the potential data to  $\chi^2$  misfit of 180 (number of independent source and

receiver pairs). The results for an inversion obtained using the zeroth, the first and the second order regularization are shown in Figure 4. The one with the zeroth order regularization has large resistivity variations in the vicinity of source and receivers indicating that the singularities in the sensitivity functions are not suppressed by this stabilizing functional. The first order regularization yields better results, however the surface artifacts are still seen in the resulting model. The second order regularization successfully suppresses the surface artifacts, giving the smoothest result.

## 4. Comparison of Minimization Algorithm

In the preceding sections we have defined the solution of the resistivity inverse problem by minimizing the objective function  $\Psi$  in equation (4). Since the forward modeling operator  $\mathbf{G}$  depends nonlinearly on  $m$ ,  $\Psi$  is non-quadratic and an iterative minimization is required.

In this section we will investigate two algorithms for minimizing the objective functional, i.e., the Gauss-Newton method, and a nonlinear conjugate gradient method.

### 4.1. Gauss-Newton Method

The Gauss-Newton method is based on expanding  $\mathbf{G}$  in a Taylor series and calculating the model correction at each iteration on the assumption of local linearity. By Taylor expansion, we have

$$\mathbf{G}(m + \delta m) = \mathbf{G}(m) + \mathbf{A}\delta m \quad (12)$$

where we have ignored higher order derivatives. Thus the value of  $\Psi$  predicted by (12) is

$$\begin{aligned}\Psi(m + \delta m) = & (d - \mathbf{G}m - \mathbf{A}\delta m)^T \mathbf{R}_{dd}^{-1} (d - \mathbf{G}m - \mathbf{A}\delta m) + \\ & \tau(m - m_0 + \delta m)^T \mathbf{L}^T \mathbf{L} (m - m_0 + \delta m)\end{aligned}\quad (13)$$

With this approximation,  $\Psi$  depends quadratically on  $\delta m$  and is minimized by setting  $\partial\Psi/\partial\delta m = 0$ , thus  $\delta m$  is found by solving

$$\delta m = (\mathbf{A}^T \mathbf{R}_{dd}^{-1} \mathbf{A} + \tau \mathbf{L}^T \mathbf{L})^{-1} (\mathbf{A}^T \mathbf{R}_{dd}^{-1} (d - \mathbf{G}m) + \tau \mathbf{L}^T \mathbf{L} (m_0 - m)) \quad (14)$$

The Gauss-Newton method thus constructs a sequence of the models by

$$m_{k+1} = m_k + \delta m_k \quad (15)$$

where  $\delta m_k$  solves the linear equation

$$\delta m_k = (\mathbf{A}_k^T \mathbf{R}_{dd}^{-1} \mathbf{A}_k + \tau \mathbf{L}^T \mathbf{L})^{-1} (\mathbf{A}_k^T \mathbf{R}_{dd}^{-1} (d - \mathbf{G}m_k) + \tau \mathbf{L}^T \mathbf{L} (m_0 - m_k)) \quad (16)$$

and a repetition of this process yields successive estimates  $m_1, m_2, \dots, m_k$  until the minimum is found.

Solving this system by computing the inverse of the Hessian,  $(\mathbf{A}^T \mathbf{R}_{dd}^{-1} \mathbf{A} + \tau \mathbf{L}^T \mathbf{L})$ , requires a tremendous amount of computing resources. Zhang *et al.* (1995) suggested that one can solve for  $\delta m$  without direct computation of the Hessian matrix by applying a linear conjugate gradient scheme. This approach significantly reduces the amount of computing resources and makes the 3-D resistivity inversion using the Gauss-Newton method practical.

The Gauss-Newton method has the desirable feature of rapid convergence if the initial guess is close to the solution, especially if, in the neighborhood of the solution the objective function appears to become quadratic, then Gauss-Newton method will find the solution in one step. Unavoidably, an initial guess that is far from the solution may lead to difficulty. The convergence may reveal overshooting and unstable features. Therefore in practice a small damping is often added to the Hessian in order to secure the stability. The penalty is the slow convergence at the early iterations.

#### 4.2. Nonlinear Conjugate Gradient Method

Another potentially more efficient algorithm for minimizing  $\Psi(m)$  is developed in this paper. This algorithm, the Nonlinear Conjugate Gradient (NLCG), was first extended by Fletcher and Reeves (1959) from the linear conjugate gradient. This method yields an alternative minimization of a nonlinear function directly without making any assumptions about its linearity.

The method of NLCG is outlined as follows:

- (a) Choose  $m_1$ , and set  $g_1 = -\nabla\Psi(m_1)$ ,  $h_1 = Cg_1$
- (b) Find  $\alpha = \alpha_k$  which minimizes  $\Psi_k(\alpha) = \Psi(m_k + \alpha h_k)$
- (c)  $m_{k+1} = m_k + \alpha_k h_k$ ,  $g_{k+1} = -\nabla\Psi(m_{k+1})$
- (d)  $h_{k+1} = Cg_{k+1} + \beta_k h_k$ , where  $\beta_k = \frac{(g_k - g_{k-1}) \cdot (Cg_k)}{(g_{k-1}) \cdot (Cg_{k-1})}$

In the algorithm,  $g_k$  is the gradient of the objective functional,  $h_k$  is the direction along which

the parameter  $\alpha_k$  is searched to minimize  $\Psi(m_k + \alpha h_k)$ ,  $C$  is a preconditioning operator which we will discuss later, and the formula for  $h_k$  and  $g_k$  above imply the basic CG-relation

$$g_i \cdot h_j = 0, \quad (i \neq j) \quad (17)$$

There are two important issues of this algorithm that need to be addressed. First, in step (b) there is a line minimization required so as to find a single variable  $\alpha$  which minimizes  $\Psi(m_k + \alpha h_k)$ . At the earlier stage of the iterations, the surface of  $\Psi$  tends to be more distorted due to a relatively large amount of nonlinearity of  $G$ , while at the later stage of the iterations it becomes more quadratic in the vicinity of the minimum. This behavior of  $\Psi$  leads us to design a line minimization routine that is adequate for both the earlier and the later iterations. The strategy is: at every iteration  $k$ , try the first step of the line minimization based on a quadratic assumption,  $\alpha = -\Psi'_\alpha / \Psi''_\alpha$ . After a minimum is bracket then estimate the minimum point and estimate its value by using a cubic interpolation. Such a strategy would not only work at the earlier stage of iteration but also guarantee a rapid quadratic convergence at the later stage of the iterations.

Second, because poor conditioning of  $\Psi$  leads to slow convergence, it is necessary to incorporate a preconditioner into the algorithm. A good preconditioner may help to decrease the objective function more quickly in the early iterations. If the problem were linear (quadratic  $\Psi$ ), a perfect preconditioner would be the inverse of the Hessian matrix

$$C = \nabla^2 \Psi \sim (A^T R_{dd}^{-1} A + \tau L^T L)^{-1} \quad (18)$$

It is probably safe to assume that this preconditioner works well in the nonlinear problem, too. However, applying it requires extensive computing resources. Hence, we explore an improved preconditioner that approximates (18) and is fast to implement. We suggest the use of the following formula as our preconditioner,

$$C = (\tau L^T L + \varepsilon I)^{-1} \quad (19)$$

where

$$\varepsilon = \frac{(\mathbf{A}u)^T \mathbf{R}_{dd}^{-1} \mathbf{A}u}{u^T u} \quad (20)$$

in which

$$u = [\log \rho_0, \log \rho_0, \log \rho_0, \dots, \log \rho_0] \quad (21)$$

is a model with constant resistivity  $\rho_0$ .

The substitution of (19) for (18) scales the d.c. component of the term  $\mathbf{A}^T \mathbf{R}_{dd}^{-1} \mathbf{A}$ . Numerically, the constant  $\varepsilon$  defined by Eq (20) is easy to calculate, because according to Eq (9), we have,

$$(\mathbf{A}u)_i = (Gm)_i \quad (22)$$

which is just the response of the constant model and can be obtained with no computation beyond the forward calculation.

One important issue needs to be addressed. Because of the strong nonlinearity of the resistivity problem, the objective function  $\Psi$  may have not only a global minimum but also some undesired local minimums. Although both the Gauss-Newton and NLCG methods

solve the nonlinear minimization problem and will find a minimum, they can not guarantee if the minimum that is found is the global minimum. Finding the global minimum is, in general, a very difficult problem. A widely used method is to repeat the algorithm starting from different initial models, finding minimums, and then picking the most extreme of them (if they are not all the same) (Press, 1992). A faster algorithm will be benefit for this procedure.

### 4.3. Numerical Comparison

We conducted a number of convergence tests for the Gauss-Newton and the nonlinear conjugate gradient method using the same synthetic model described before (Figure 2). The Gauss-Newton minimization scheme used in this report was developed by Zhang *et al.* (1995).

Choosing a starting model with a homogeneous resistivity value of  $200 \Omega.m$ , the convergence results for each optimization method are shown in Figure 5a. Here 'NLCG' denotes the NLCG method with the improved preconditioner (19), 'NLCG-1' denotes the NLCG method without preconditioning ( $C=identity$ ), and 'NLCG-2' denotes the NLCG with the Hessian (18). From these results it is clear that the convergence rate of the NLCG method depends strongly on the preconditioner: NLCG is the most efficient method in terms of the CPU time, and NLCG-2 is the least efficient method. We also see that NLCG-2 makes larger decreases in  $\Psi$  but takes more CPU time. The Gauss-Newton method interpolates between NLCG and NLCG-2. When all of the methods converge, they find the same solution (Figure

5b).

If the initial model is chosen to be close to the true model:  $m_0 := 50\Omega.m$  (*inside the conductive block*);  $= 100\Omega.m$  (*other region*), the Gauss-Newton method will be as efficient as that of the NLCG method (Figure 6a). This result demonstrates that the Gauss-Newton method has a fast convergence rate in the neighborhood of the solution. Both methods find the same solution (Figure 6b).

When the initial model is far from the solution,  $m_0 = 500\Omega.m$ , the NLCG method has much faster convergence than the Gauss-Newton method (Figure 7a). Both methods finally find the same solution (Figure 7b).

## 5. Application to Field Data: 3-D Resistivity Survey at the Aberjona Watershed, Woburn, Massachusetts

### Background and Objective

The Aberjona Watershed is located in eastern Massachusetts (Figure 8, McBrearty, 1993). The area has a history of industrial contamination dating back to the beginning of the century. Industries, including leather tanners, metal cleaning and automobile salvage yards, dumped their waste into the ground and contaminated the ground water with high concentrations of chemicals shown to be cancer-causing in laboratory animals, including chloroform, perchloroethylene (PCE), trichloroethane, and trichloroethylene (TCE). A suspected result



of the contamination was a high incidence of childhood leukemia in the area during the mid 1980s (Diperna, 1985). The area was designated as a U.S. Environmental Protection Agency superfund site in 1982, and has become the focus of numerous environmental investigations.

The subsurface geology of the Aberjona Watershed is characterized by glacial outwash and till deposits. One of the major valleys—the Aberjona valley formed by the glacial movement, runs beneath the main branch of the Aberjona river. The valley that forms the transmissive regions of the aquifer to a depth of over 100 feet is filled with glacial outwash consisting of fine to medium sands with traces of silt at shallow depth, and medium to coarse sand and gravel as the depth increases. Previous studies also indicated a peat layer overlaying the stratified sand deposits extending over a large area with the thickness range from 2 to 7 feet (USGS Report, 1989). Because of the shallow water table the soils are generally saturated to the surface, the effect of the topography is to cause a damp soft soil with scattered areas of very shallow pooling water. Further, during the winter time, the hydraulic conductivity decreases causing a larger areas of flooding.

Our study site (marked inside a circle in Figure 8) is located near the Well H region of the Aberjona River. Our interest focuses on characterizing the soil around the river in an effort to understand the transport mechanisms that have been involved in the contamination of the drinking water. Before our resistivity survey, other geophysical investigations were employed in the area including ground penetrating radar, and cone penetrometer surveys (Zeeb *et al.*, 1994). The ultimate goal of the resistivity survey was to correlate soil properties with those

investigations to extend the point-source ground truth information into a 3-D map of the stratigraphy of the whole region.

### **5.1. The Resistivity Measurement**

We performed the electrical resistivity survey at the site in March 1995. Figure 9 shows the experiment site and the electrode configuration. There were 80 electrodes placed at 25 ft intervals in an 8x10 array on the surface, covering a 175 x 225 ( $ft^2$ ) area. Electrical current was injected one at a time into 30 of the electrodes (marked in red), with the negative end of the current placed 1000 feet south of the Well H. Potential differences were measured between each of the remaining electrodes and a point adjacent to the current electrode. A total of 30x80 potential differences were thus obtained.

Figure 10 shows a part of data set where the potential differences are displayed in form of contour lines. The current sources are clearly noticeable in the plot where they correspond to the highest potential differences. We estimated that the measured potential differences were accurate to within 5 percent based upon repeated measurements, such that the standard deviation for each datum was assumed to be 5 percent of the potential difference.

### **5.2. The Inversion Results**

We generated a 3-D model with 26x24x20 cells to cover the experimental region. To construct a starting model, surface resistivity information was used. As one can see from Figure 9, a

part of the Aberjona River meanders its way southward, about 100 feet west of the Well H. The river was built into the starting model by assigning an initial resistivity value of  $10 \Omega.m$  to cells traversed the path of the river. In the rest of the area resistivity values of surface soil samples were measured and their mean  $\bar{\rho} = 65(\Omega.m)$  was assigned to the remaining cells of the starting model.

The NLCG method is used to invert the 3-D resistivity structure. Gauss-Newton is also used as a comparison. The convergence rate of both method is shown in Figure 11. The Gauss-Newton method requires approximately 15 hours of computing time on a DEC alpha workstation to find one solution, while the NLCG methods takes 1.5 hours.

Figures 12a and 12b show a 3-D resistivity inversion model as horizontal + vertical cross-sections. The results depict a resistive zone at 20 feet below the surface, dipping from southeast to northwest. Above the resistive zone, the results show a bowl-shape conductive zone. In order to interpret the physical soil types, a vertical cone penetrometer profile obtained at the place that is 75 feet west of the Well H is used to correlate the resistivity results. The results are shown in Figure 13.

The cone penetrometer response indicates somewhat complicated soil types at shallow depth. Except for a region of organic peat layers directly below the surface, there is a section comprised of brown, spongy material that has a high water content (80% water by weight) and contains almost no organic matter. This section is found to be the diatomaceous earth which consists primarily of siliceous skeletons of diatom-microscopic. Because

of high porosity (70–90 % in general) resulting in high water content, the diatomaceous earth section appears to be very conductive. Adjacent to the bowl-shaped lower boundary of the diatomaceous earth is, as expected, a glacial sand layer which is quite resistive. The boundary between the conductive zone (peats + diatomaceous earth) and the resistive zone (sand), as indicated by the 3-D resistivity inversion model, is strongly coherent with the cone penetrometer results. However, due to the diffusive nature of the electrical energy and perhaps, due to the “minimum structure” approach, the 3-D resistivity inversion cannot delineate the heterogeneity within the conductive zone, i.e., different thin peat layers and the diatomaceous earth section.

The resistivity results are in strong agreement with GPR (Ground Penetrating Radar) experiments (Cist *et al.*, 1995). Figures 14a and 14b each compare a vertical GPR section with a correspondent vertical cross-section through the 3-D resistivity inversion model. From these plots, one can see that the shape of the boundary between the diatomaceous earth and the sand layer is in good agreement between the two experiments. Below this interface, the GPR section is dominated by ringing effects of the antennas, whereas the resistivity model detects vertical and lateral variations of the resistivity distribution. This result indicates that the resistivity method has great advantages in resolving structures at depths unattainable to either GPR method or cone penetrometer.

## 6. Conclusions

In this paper, we have presented a method for solving the nonlinear d.c. electrical resistivity inverse problem. To deal with the ill-posedness of the problem, the method uses Tikhonov regularization to obtain a solution which has the least structure necessary to fit the data to specified error bounds. We have investigated three different smoothness constraints and concluded that it is necessary to constrain second order spatial derivatives of the resistivity function to obtain smooth, stable solutions. This result can be understood in terms of the sensitivity functions for 3-D resistivity data and the fact that they are singular at source and receiver positions.

To implement Tikhonov regularization numerically, we have developed a fast and efficient algorithm based on conjugate gradient with preconditioning to solve the nonlinear minimization problem. Using a simple preconditioning operator, the NLCG algorithm results in a tremendous time savings over the conventional Gauss-Newton approach, especially when the initial guess is far from the solution.

We have successfully applied our 3-D resistivity inversion algorithm to a actual resistivity field survey in the Aberjona Watershed, Woburn, Massachusetts. With this field data, the nonlinear conjugate gradient algorithm finds minimum structure models with approximately ten times less computation than the Gauss-Newton method. Our 3-D resistivity image indicates two major layers of the site: the conductive layer which involves the peat and the diatomaceous earth is located beneath the surface; the resistive sand layer is underlined

at an elevation of 20 feet deep, dipping from south-east to north-west. Results have been compared and found to be strongly correlated with other geophysical experiments of the site such as cone penetrometer and GPR measurements.

## Acknowledgment

This work was supported by Air Force Research Contract *F19628-93-K-0027*, monitored by the Phillips Laboratory.

## References

- Backus G., and Gilbert F., Numerical application of a formalism for geophysical inverse problems, *Geophys. J. Roy. Astron. Soc.*, 13, 247-276, 1967.
- Backus G., and Gilbert F., The resolving power of gross Earth data, *Geophys. J. Roy. Astron. Soc.*, 16 169-205, 1968.
- Blum, R., 1989, Geoelectrical Mapping and Groundwater Contamination in Detection of Subsurface Flow Phenomena, G-P Merker (ed.), Springer, Berlin Heidelberg, 253-260.
- Bogoslovsky, V.A. et al., 1979, Geophysical methods for controlling the seepage regime in earth dams, *Bull. Int. Assoc. Geol.*, 20, 249-251.
- Burger, H.R., 1992, *Exploration Geophysics of the Shallow Surface*, Prentice Hall.
- Buselli, G.B., et al., 1991, Detection of groundwater contamination near waste disposal sites with transient electromagnetic and electrical methods, in *Investigations in Geophysics*

- no. 5: *Geotechnical and Environmental Geophysics, II*, SEG, Tulsa, 27–39.
- Carpenter, P.J., et al., 1990, Use of resistivity soundings to determine landfill structure, *Ground Water*, 28, 569–575.
- Cist, B.D., et al., 1995, Correlating GPR and resistivity survey with cone penetrometer and shallow coring studies along the Aberjona River.
- Constable, S.C., Parker, R., and Constable, C.G., 1987, Occam's Inversion: A practical algorithm for generating smooth models from electromagnetic sounding data, *Geophysics*, 52, 289–300.
- Day, A., Morrison, H.F., Resistivity modeling for arbitrary shaped three-dimensional structures, *Geophysics*, 44, 753–780.
- deGroot-Hedlin, C., and Constable, S., 1990, Occam's inversion to generate smooth, two-dimensional models from magnetotelluric data, *Geophysics*, 55, 1613–1624.
- Diperna, P., 1985, *Cluster Mystery*, Mosby.
- Duijndam, A.J.W., 1988, Bayesian estimation in seismic inversion. Part II: Uncertainty Analysis, *Geophys. Prosp.*, 36, 899–918.
- Ellis, R.G., *Joint 3-D EM Inversion*, SEG, 1995, 307–323.
- Ellis, R.G. and Oldenburg, D.W., 1994a, Applied geophysical inversion, *Geophys. J. Int.*, 116, 5–11.
- Ellis, R.G. and Oldenburg, D.W., 1994b, The pole-pole 3-D DC-resistivity inverse problem: a conjugate gradient approach: *Geophys. J. Int.*, 119, 187–194.

- Franklin J., Well-posed stochastic extensions of ill-posed linear problems, *Math. Anal. Appl.*, 31, 682–716, 1970.
- Inman, J.R., 1975, Resistivity inversion with ridge regression, *Geophysics*, 40, 798–817.
- Jiracek, G.R., Rodi, W.L., and Vayan, L.L., 1987, Implications of magnetotelluric modeling for the deep crustal environment in the Rio Grande rift, *Phys. Earth Planet. Interiors*, 45, 179–192.
- Keller, G.V., and Frischknecht, F.C., 1966, *Electrical Methods in Geophysical Prospecting*, Oxford, Pergamon, 517.
- Mackie, R.L. and Madden, T.R., 1993, Three-dimensional magnetotellurics inversion using conjugate gradients, *Geophys. J. Int.*, 115, 215–229.
- Madden, T.R., 1972, Transmission system and network analogies to geophysical forward and inverse problems, *ONR Tech. Rep. 72-3*.
- Marquardt, D.W., 1963, An algorithm for least-squares estimation of non-linear parameters, *J. Soc. Ind. App. Math.*, 11, 431–441.
- Mazac, O., et al., 1990a, Determination of the extent of oil contamination in groundwater by geoelectrical methods, in *Investigations in Geophysics no. 5: Geotechnical and Environmental Geophysics, II*, SEG, Tulsa, 112–119.
- McBrearty, D., 1993, Fracture flow as influenced by geologic fractures in the Aberjona Valley, Massachusetts, *M.S. thesis*, MIT.
- McNeill, J.D., 1990 Use of electromagnetic methods for groundwater studies in ward, stanley



- H., ed., *Geotechnical and Environmental Geophysics, I*, 191–218.
- Medeiros, W.E. and Lima, O.A.L., 1990, Geoelectrical investigation for groundwater in crystalline terrains of center Bahia, Brazil, *Ground Water*, 28, 518–523.
- Narayan, S., 1990, Two-dimensional resistivity inversion, M.S. thesis, Univ. of Calif. Riverside.
- Okko, O.T., 1993, Geophysical investigations in municipal engineering - the enlargement of landfill area in Hanko city, southern Finland, in *Procs. SAGEEP 1993*, 669–676.
- Parker, R., 1984, The inverse problem of resistivity sounding, *Geophysics*, 49, 2143–2158.
- Park, S.K. and Van, G.P., 1991, Inversion of pole-pole data for 3-D resistivity structure beneath arrays of electrodes, *Geophysics*, 56, 951–960.
- Pelton, W.H., Rijo, L., and Ward, S.H., 1978, Inversion of two-dimensional resistivity and induced polarization data, *Geophysics*, 43, 788–803.
- Petrack, W.R., Jr., Sill, W.R., and Ward, S.H., 1981, Three-dimensional resistivity inversion using alpha centers, *Geophysics*, 46, 1148–1163.
- Pilkington, M., and Todoeschuck, J.P., 1992, Natural smoothness constraints in cross-hole seismic tomography, *Geophys. Prosp.*, 40, 227–242.
- Press, F. et al., 1992, *Numerical Recipes*, Cambridge.
- Rodi, W.L. et al., 1995, Algorithms for 3-D d.c. resistivity inversion, draft.
- Scales, J.A., Docherty, P. and Gersztenkorn, A., 1990, Regularization of nonlinear inverse problems: imaging the near-surface weathering layer, *Inverse Problems*, 6, 115–131.

- Shima, H., 1992, 2-D and 3-D resistivity image reconstruction using crosshole data, *Geophysics*, 53, 1565-1576.
- Smith, N.C., and Vozoff, K., 1984, Two-dimensional DC resistivity inversion for dipole-dipole data, *IEEE Trans. Geoscience and Re. Sens.*, GE-22, 21-28.
- Spies, B.R., and Ellis, R.G., 1995, Borehole resistivity tomography of a pilot-scale, in-site, vitrification test, *Geophysics*, 60, 886-898.
- Tarantola, A., and Valette, B., 1982, Inverse Problem = Quest for information, *J. Geophys.*, 50, 159-170.
- Tikhonov, A., Arsenine, V., *Solutions of Ill-posed Problems*, Willy, 1977.
- Tripp, A.C., Hohmann, G.W., and Swift, C.M., Jr., 1984, Two-dimensional resistivity inversion, *Geophysics*, 49, 1708-1717.
- U.S.G.S., 1989, Hydrogeology and simulation of ground-water flow at superfund-site wells G and H, Woburn, Massachusetts, 4.
- Van, G.P., Park, S.K., and Hamilton, P., 1992, Use of electrical resistivity monitoring systems to detect leaks from storage ponds, *SAGEEP '92*, Chicago, 629-647.
- Zeeb, P. et al., 1994, The effects of deposit scale heterogeneities on the trapping and transport of toxic metals in an urban riverine peatland, *AGUMSNA*, 148.
- Zhang, J., Mackie, R.L., and Madden, T.R., 1995, Three-dimensional resistivity for ward modeling and inversion using conjugate gradients, *Geophysics*, 60, 1313-1325.

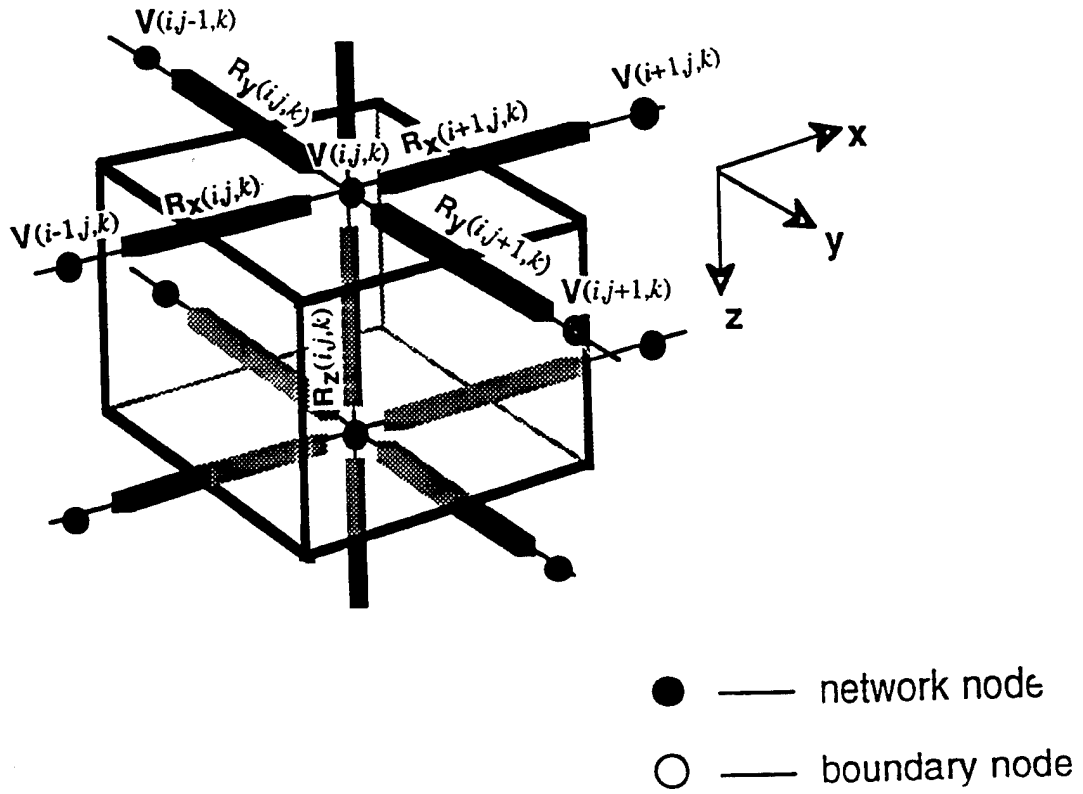


Figure 1: The 3-D resistivity model is discretized into a network which consists of network nodes, boundary nodes, and impedance branches.

## View of the Model

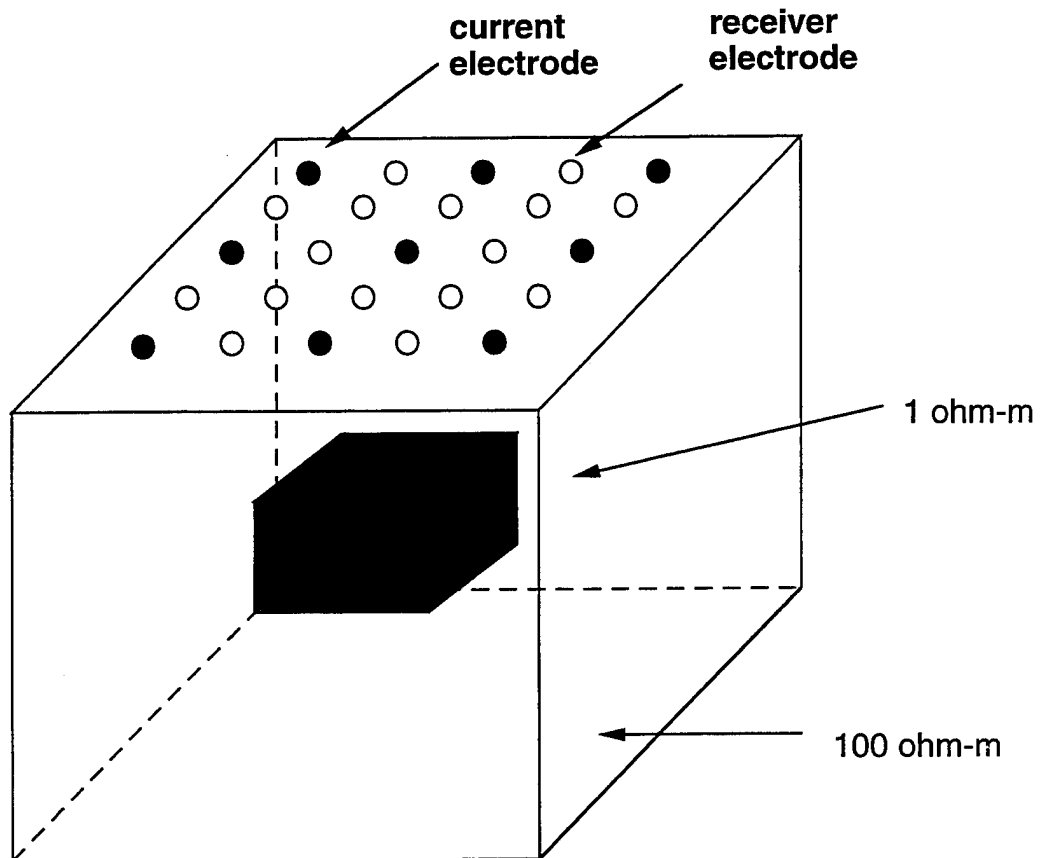


Figure 2: The synthetic model consists of the 7x7x3 prism ( $p=1$  ohm.m) inside a 21x21x15 background ( $p=100$  ohm.m). The data are defined on a 5x5 electrode array and comprise 24 potential field measurements for each of 9 pole current sources.

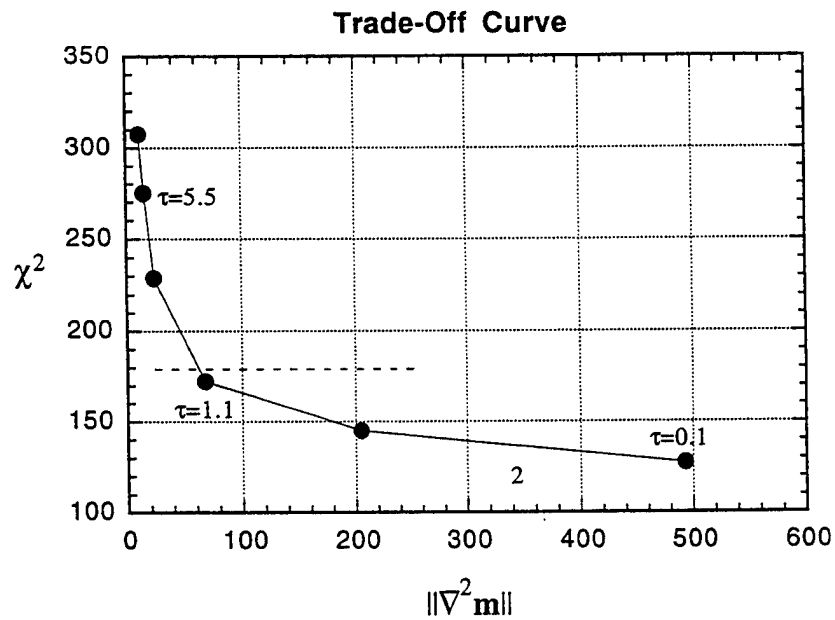


Figure 3a: This trade-off curve shows how the data misfit is balanced by the model roughness. If the model is too smooth, it cannot fit the data well. Over-fitting the data will result in a rough model which contains incorrect surface anomalies. An optimum choice is to fit chi-square to the number of independent data which, in this case, is 180, indicated by the dashed line.

### Min. Laplacian Solutions Controlled by $\tau$

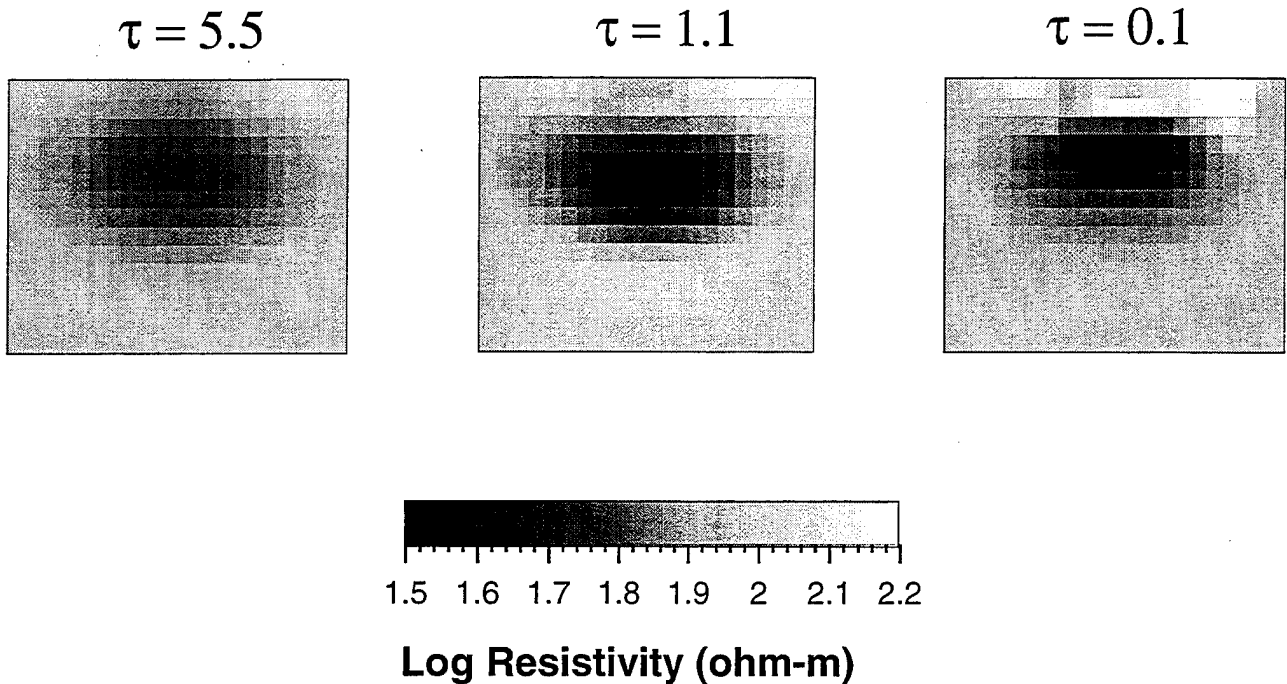


Figure 3b: Resistivity inversion models for three values of the regularization parameter  $\tau$ .

### Solutions by Three Different Stabilizing Functionals

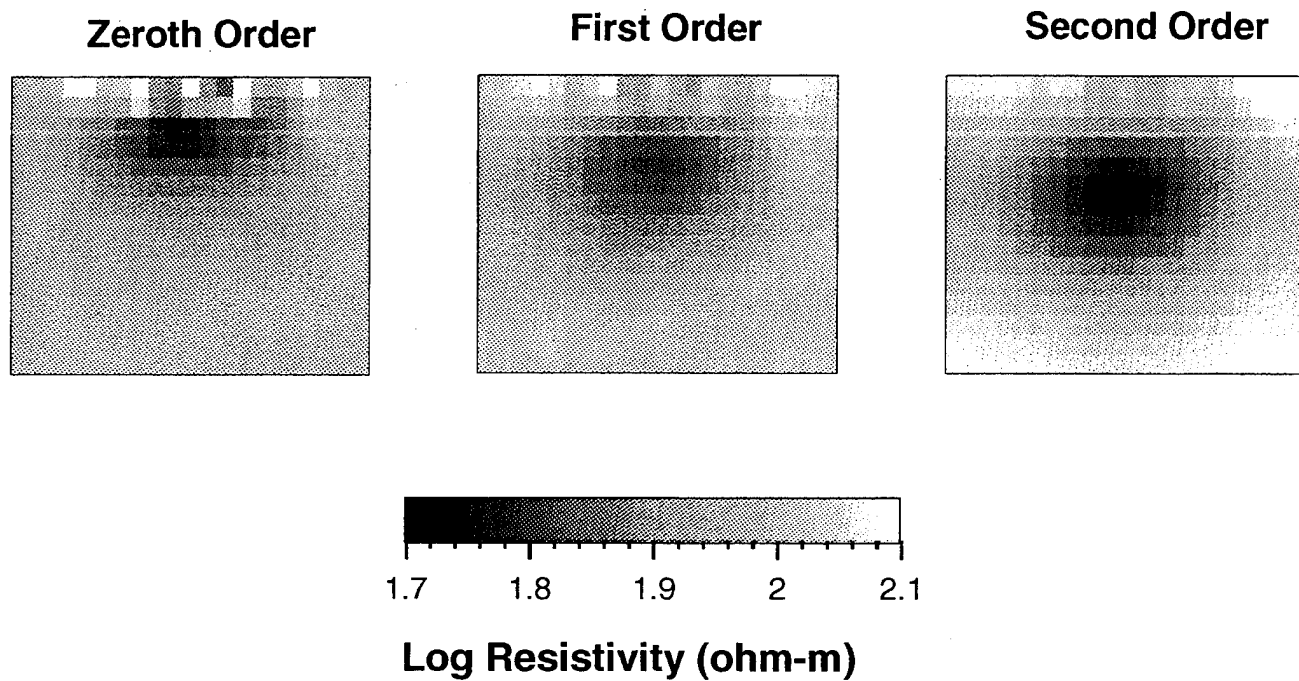


Figure 4: Resistivity inversion models (shown is a vertical cross-section throughout the center of the model).

### Efficiency Test of Different Methods

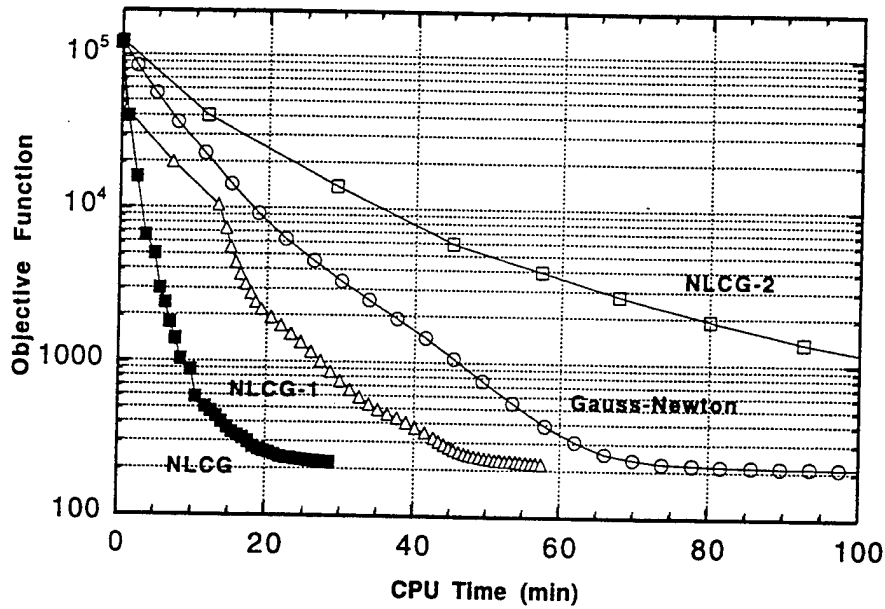


Figure 5a: NLCG is the most efficient method among the others. NLCG-2 is the least efficient method. The Gauss-Newton method interpolates between them. The initial model for this test is 200 (ohm.m).

### Solutions by Different Algorithms (m1=200 ohm.m)

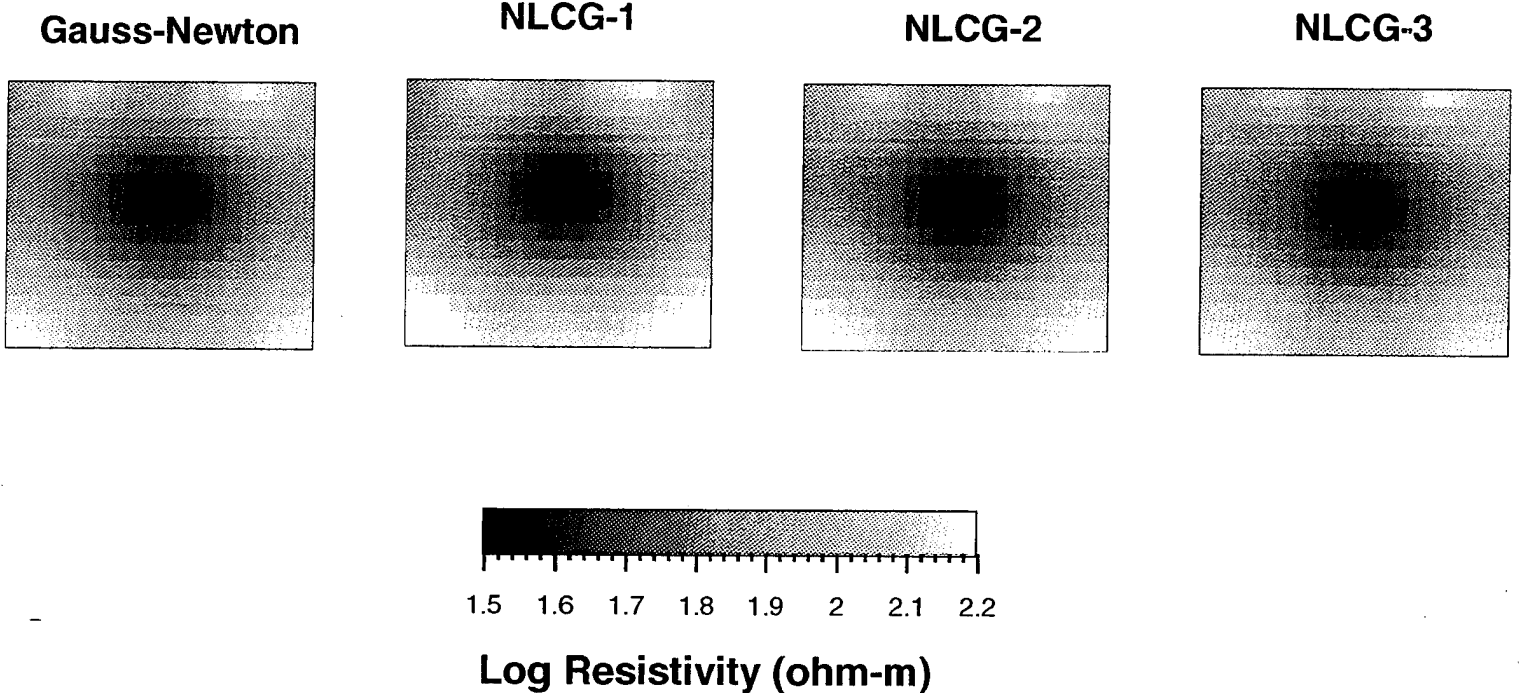


Figure 5b: All of the algorithms find the same solution using an initial model, m1=2-(ohm.m)

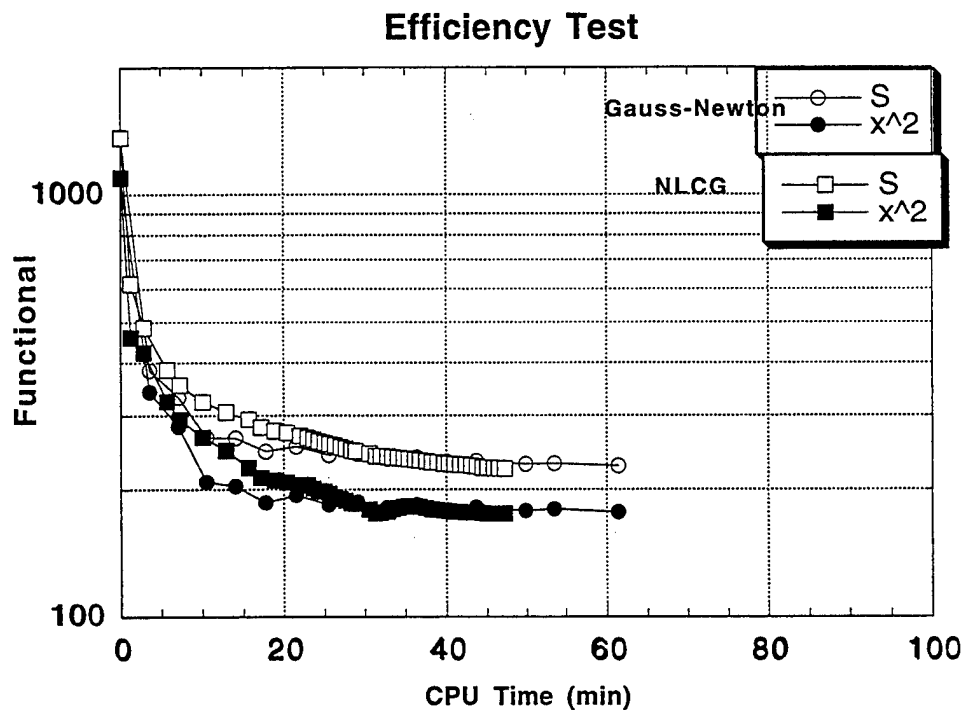


Figure 6a: When the initial guess is close to the true model, the Gauss-Newton method is about as efficient as the NLCG method. Where  $S$  denotes the objective function, and  $\chi^2$  denotes the chi-square. The initial model for this test is  $m_1=1-$  (background),  $=50$  (inside the conductive block).

### Solutions by Different Algorithms ( $m_1=100$ (out), $50$ (in))

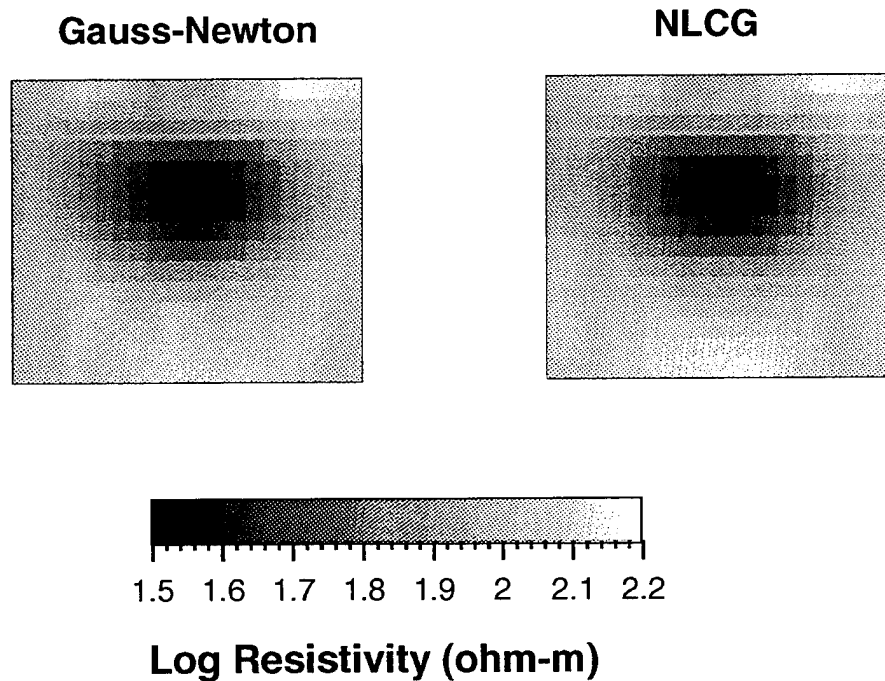


Figure 6b: Gauss-Newton finds the same solution as that of NLCG with a good initial model.



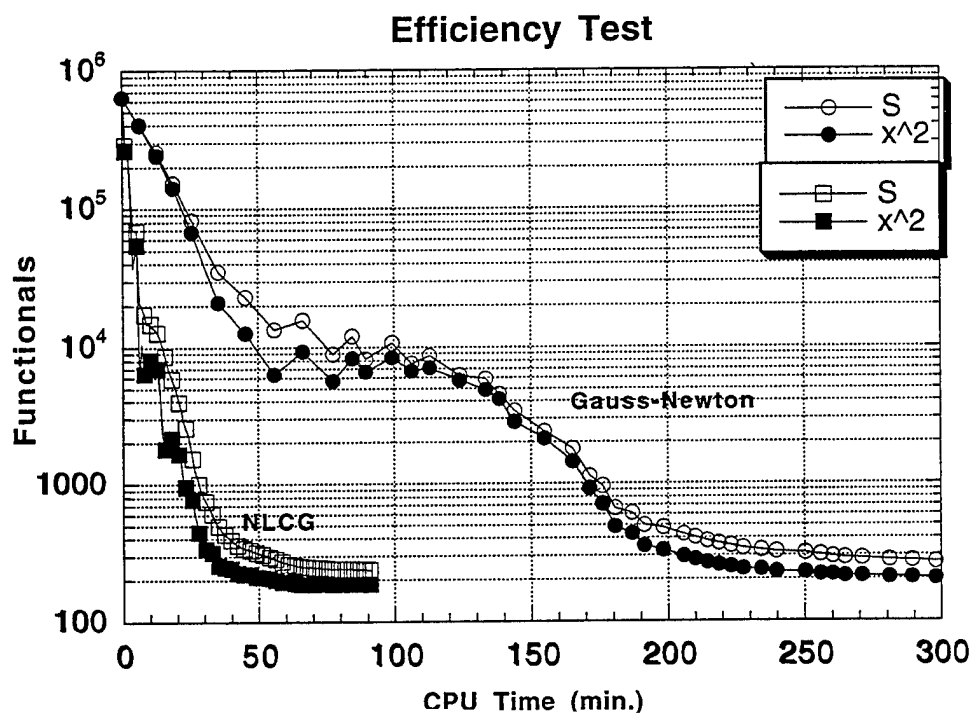


Figure 7a: The NLCG method is much more efficient in terms of the CPU time compared to the Gauss-Newton method. Where S denotes the objective function,  $X^2$  denotes chi-square. The initial model is cosen as  $m_0=500$  ohm-m.

### Solutions by Different Algorithms ( $m_1=500$ )

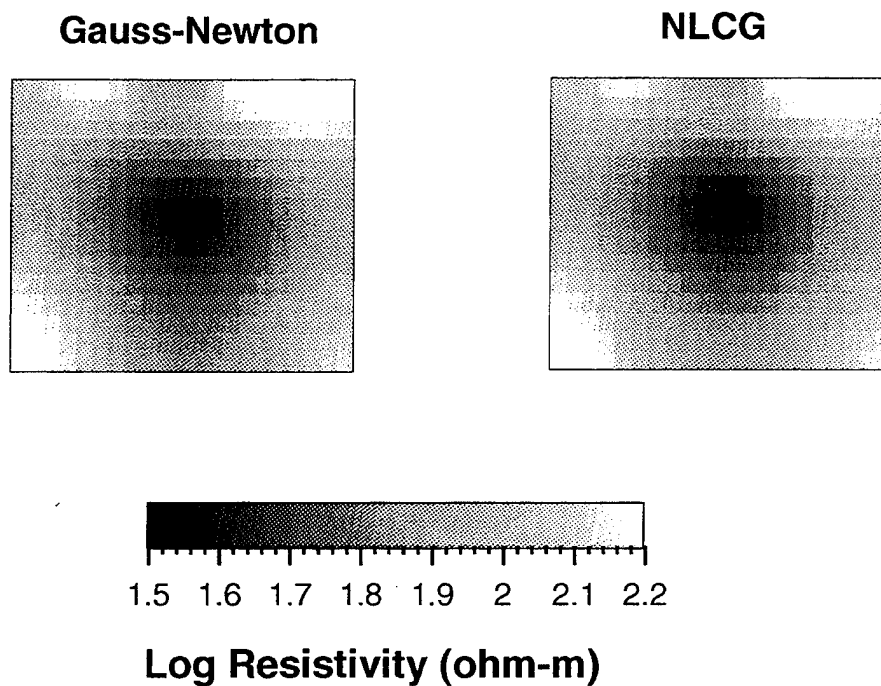


Figure 7b: Gauss-Newton finds the similar solution as that of NLCG with bad initial model.



BASE MAP MODIFIED FROM TOPOGRAPHICAL  
MAPS T-12, 13, 16, 17, 21, 22, CITY OF WOBURN,  
MASSACHUSETTS

#### EXPLANATION

- |                        |                        |
|------------------------|------------------------|
| Wetland                | Industrial supply well |
| Active model boundary. | Observation well       |
| A—A' Geologic section  | Public supply well     |

Figure 8: The Aberjona Watershed is located in eastern Massachusetts. Our experiment site (squared) is located near Well H region of the Aberjona river in the town of Woburn, a suburb 10 miles north of Boston.

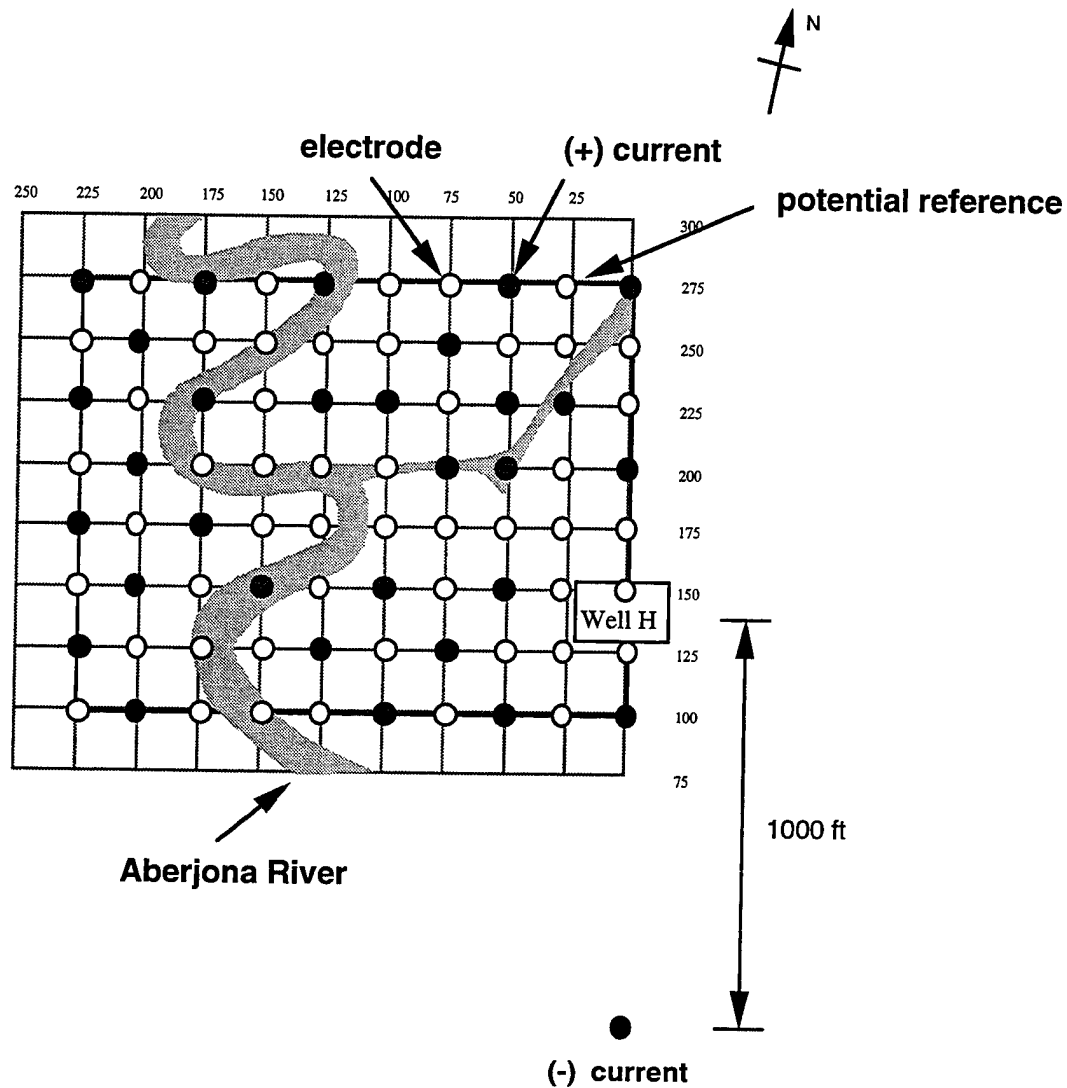


Figure 9: The resistivity experiment deployed 80 electrodes deployed in the Well H area, 30 of them were used as the current electrodes. The negative current electrode is 1000 ft south of Well H. The potential differences were measured with respect to a point which is adjacent to the current electrode.

### Contour of the observed potential differences

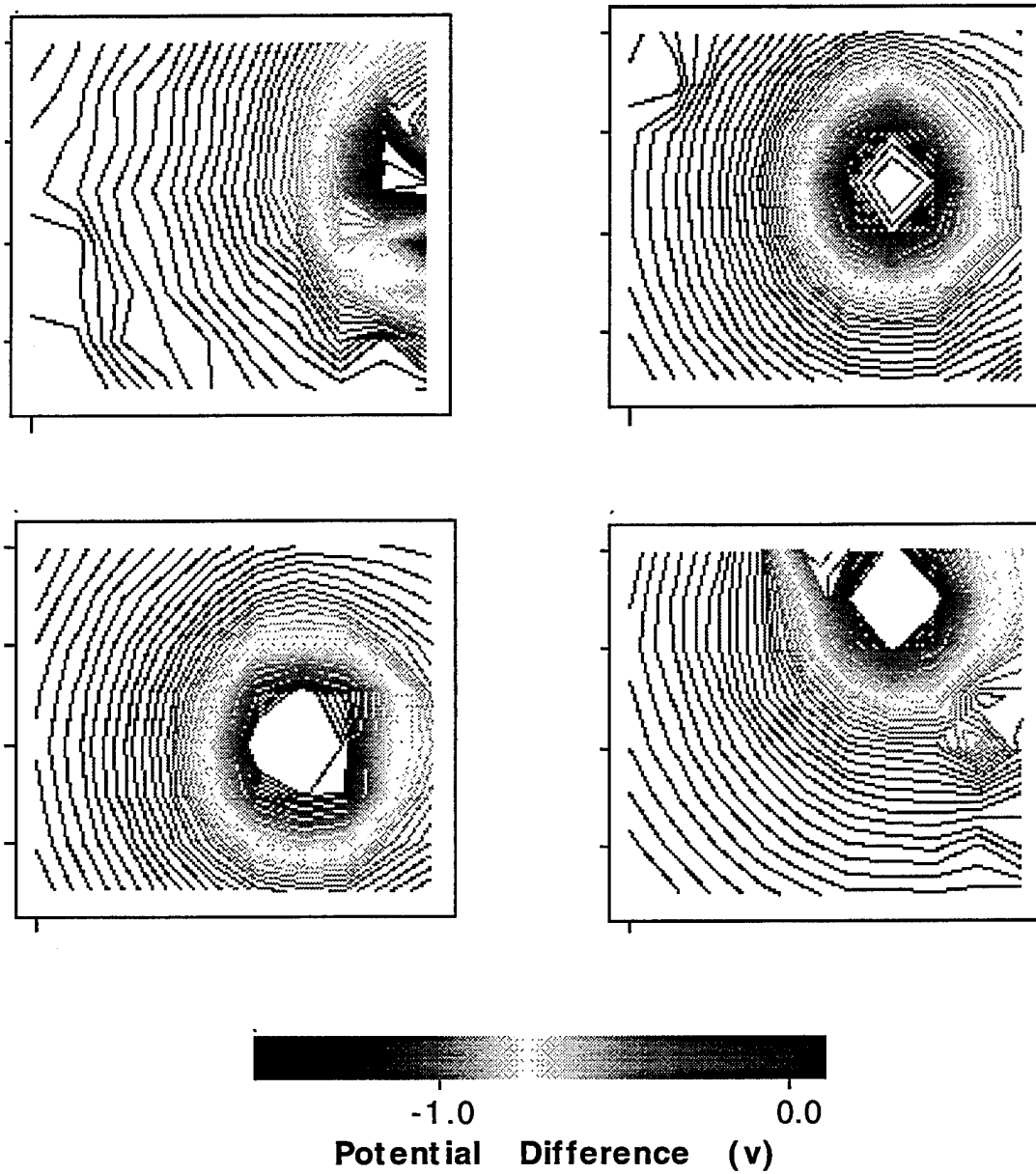


Figure 10: Contour plots of the measured potential differences from four current sources. The current sources are noticeable, which appear to be the singularities.

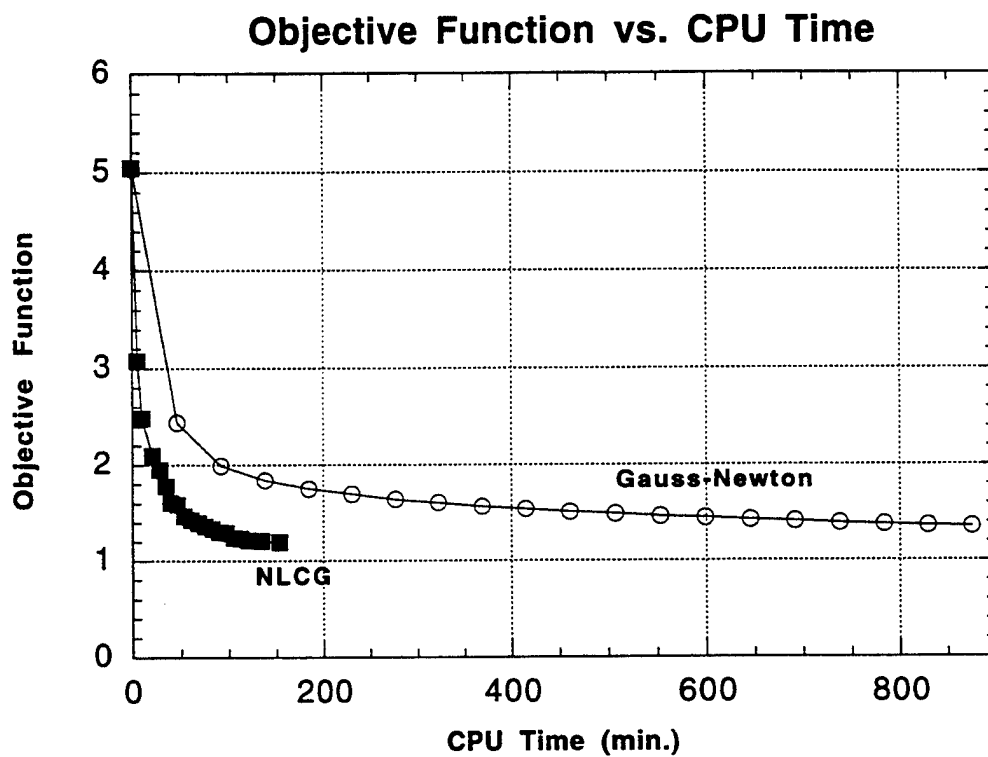


Figure 11: Iteration histories for the NLCG and Gauss-Newton algorithm of the Aberjona data. The NLCG algorithm yields an acceptable inversion model approximately ten times faster than the Gauss-Newton method.

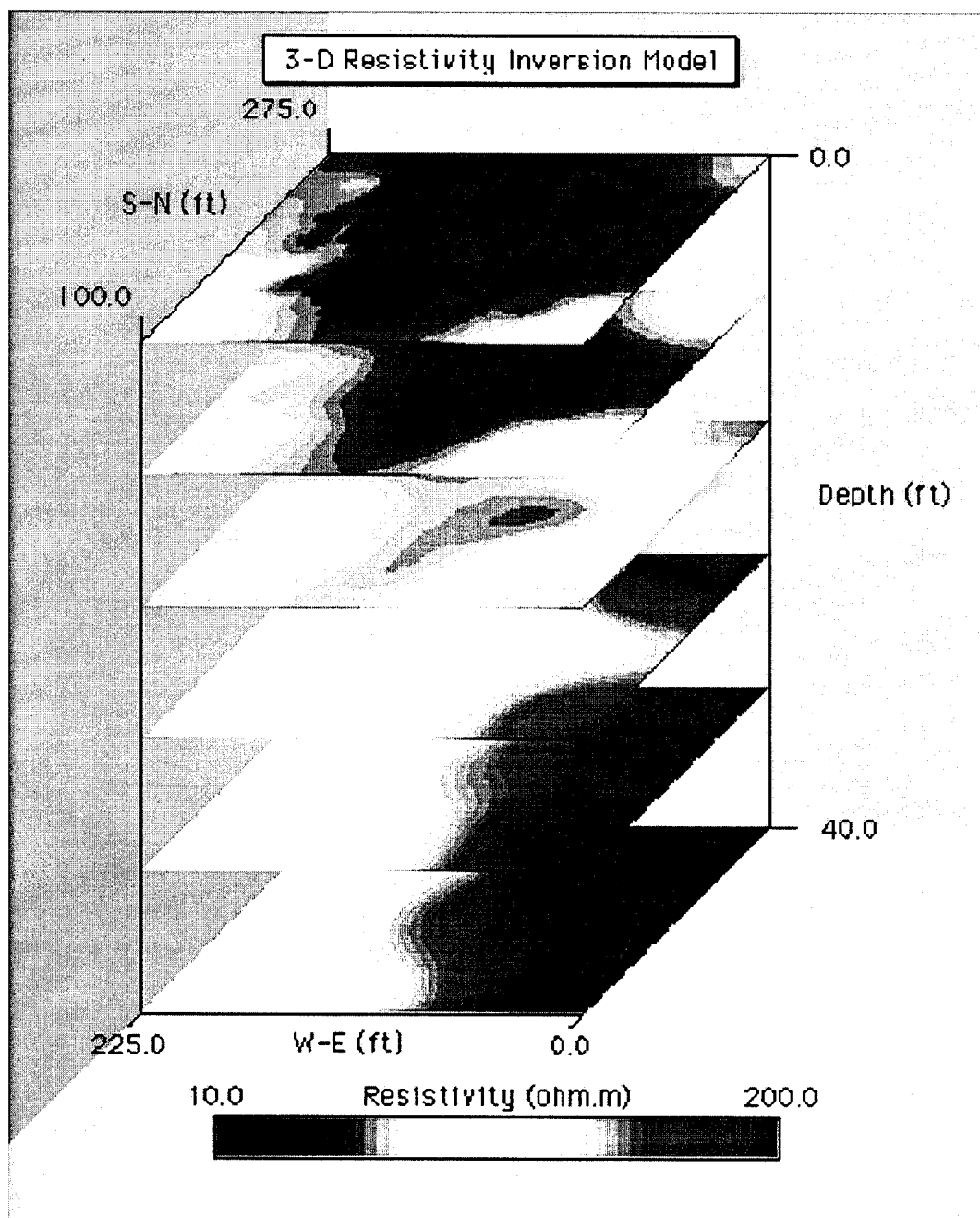


Figure 12-(a) 3D resistivity inversion model (vertical slices) for the Aberjona contamination site. The resistive zone at depth, dipping from east to west, is interpreted to be a sand formation underlying more conductive diatomaceous earth.

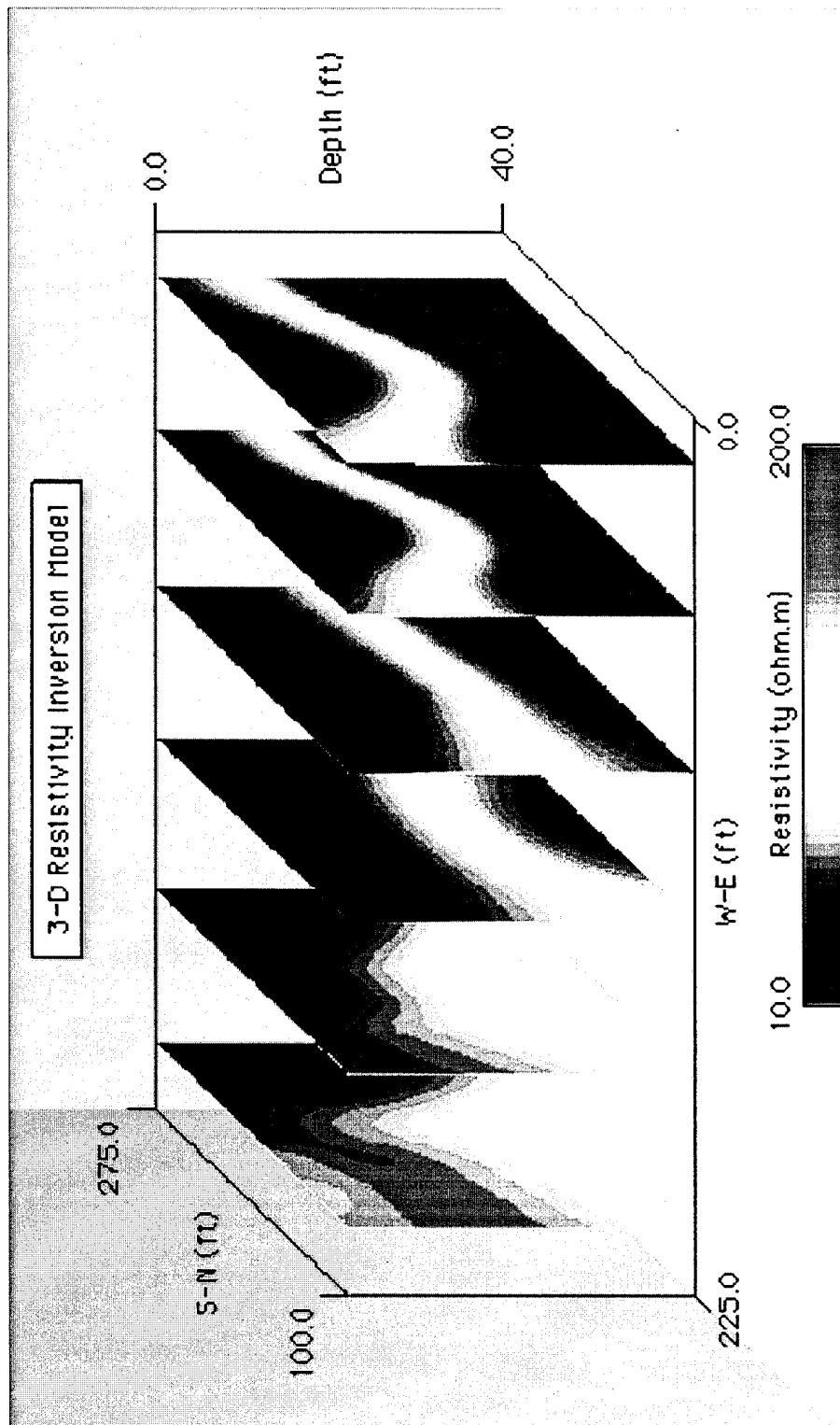


Figure 12-(b) 3D resistivity inversion model (horizontal slices) for the Aberjona contamination site. The resistive zone at depth, dipping from east to west, is interpreted to be a sand formation underlying more conductive diatomaceous earth.

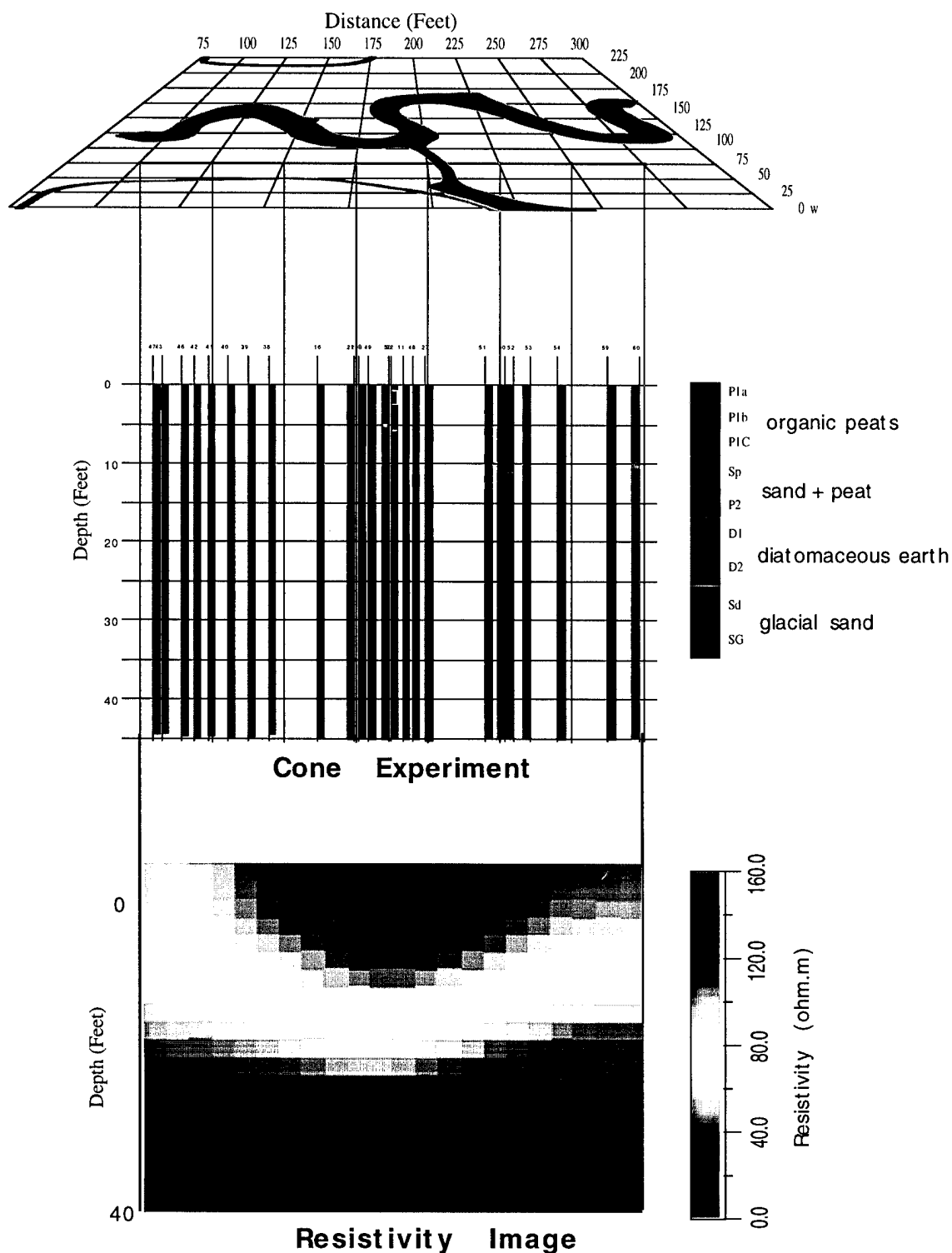


Figure 13, Correlating the 3-D resistivity inversion model with the Cone penetrometer response. The conductive zone is found to be a region of peat layers and a diatomaceous earth section, while the resistive zone corresponds to a glacial sand layer. Note, the bowl-shape lower boundary of the diatomaceous earth is in good agreement between the two methods.



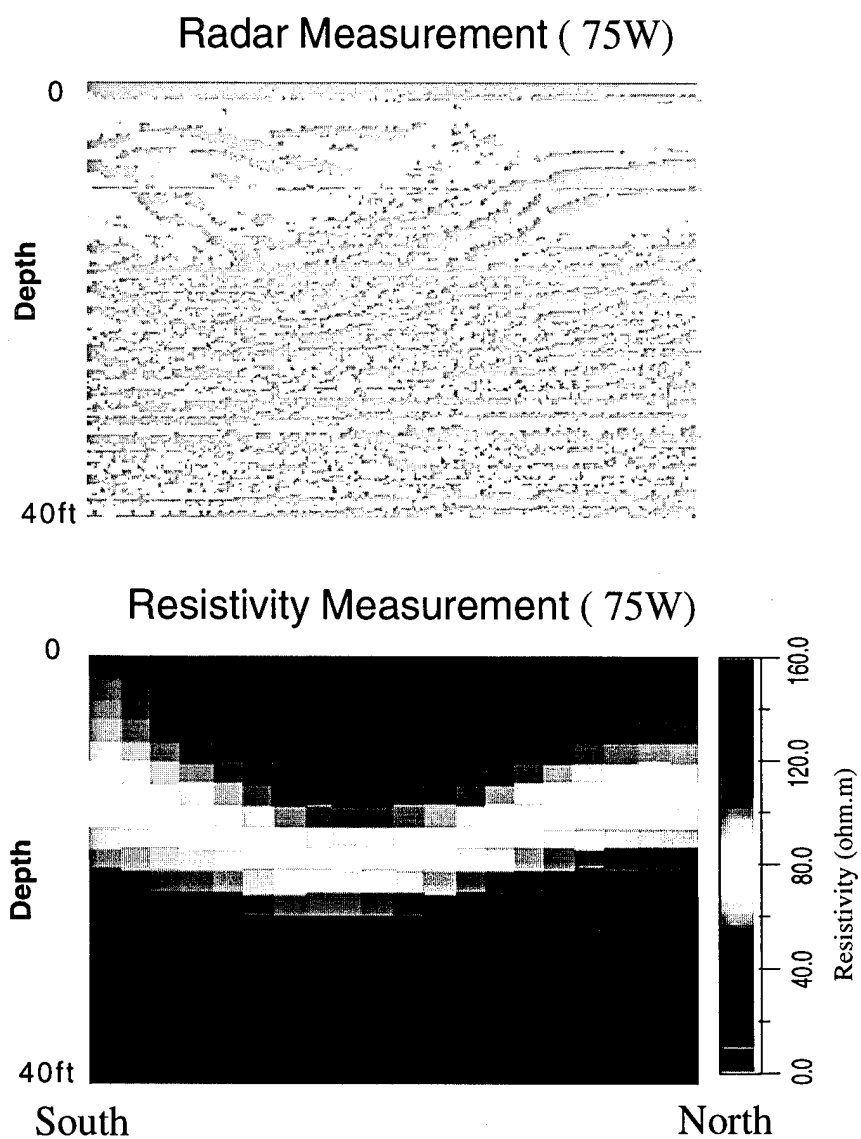


Fig 14 -(a) Comparison of resistivity inversion model with a GPR section located at 75 ft west of the Well H. The shape of the boundary between the diatomaceous earth and the sand layer is in good agreement.

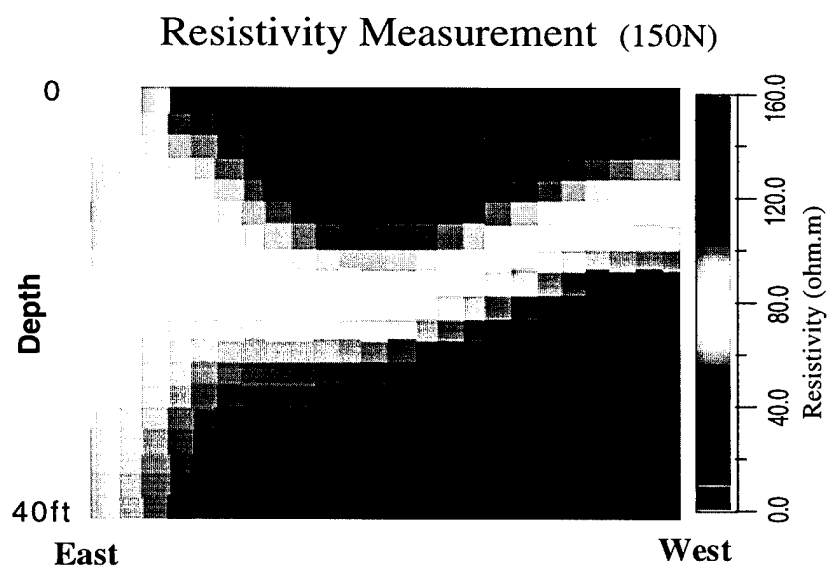
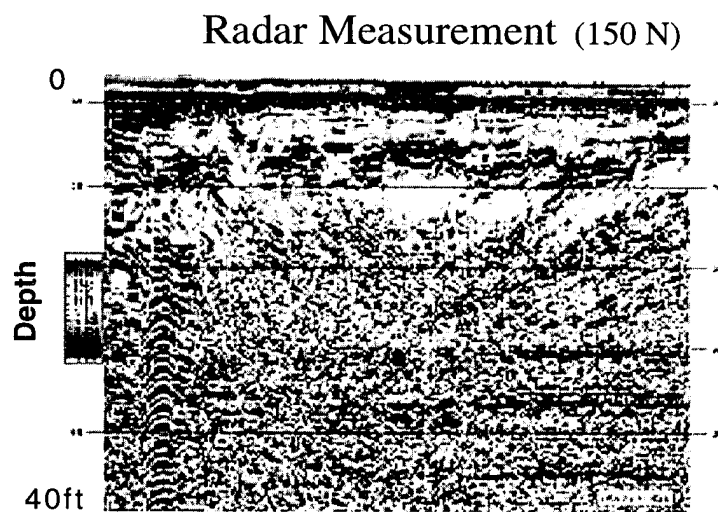


Fig 14 -(b) Comparison of resistivity inversion model with a GPR section located at 150 feet north of the Well H. The shape of the boundary between the diatomaceous earth and the sand layer is in good agreement.

# ELECTROSEISMIC WAVES FROM POINT SOURCES IN LAYERED MEDIA

## Summary

In sedimentary, porous material saturated by a fluid electrolyte, mechanical and electromagnetic disturbances are coupled. The coupling is electrokinetic in nature due to an excess of electrolyte ions that exists in a fluid layer near the grain surfaces within the material. Seismic waves in sedimentary material generate relative fluid-solid motion that induces an electrical streaming current. When a seismic pulse traverses contrasts in electrical and/or mechanical medium properties a dynamic streaming current imbalance is induced across such a contrast, generating electromagnetic disturbances that are measurable at the earth's surface. This paper numerically determines this full-waveform electroseismic pointsource response in a stratified porous medium. It is shown that the macroscopic governing equations controlling the coupled electromagnetics and acoustics of porous media decouple into two sets corresponding to vertical a (*PSVTM*) or horizontal (*SHTE*) polarization of the transverse wavefields. The seismic pulse is shown to induce electric fields that travel with the compressional wavespeed and magnetic fields that travel with the shear waves. The frequency content of the converted electromagnetic field has the same frequency content of the driving incident seismic pulse, as long as the propagation distances are much less than the electromagnetic skin depth.

Snapshots in time and converted electromagnetic amplitudes versus seismic point source-antenna offset are calculated for contrasts in mechanical and/or electrical medium properties. The *TM* component amplitude radiation pattern away from the interface shows similarities with an effective electric dipole radiation pattern centered right beneath the source at the contrast. The *TM* mode amplitudes decay rapidly with traveled distance and suggests the importance of a Vertical ElectroSeismic Profiling geometry to record the converted electromagnetic signal at antennas close to the target (contrast) of interest.

## 1. Introduction

When seismic waves propagate through a fluid saturated sedimentary material a small amount of relative fluid-solid motion is induced (the motion of the pore fluid to the solid matrix defines relative flow). The driving force for the relative flow is a combination of pressure gradients set up by the peaks and troughs of a compressional wave and by grain accelerations. The relative flow caused by grain accelerations can therefore be due to either compressional or shear waves.

A fluid electrolyte in contact with a solid surface chemically adsorbs the anions from the electrolyte to the grain surfaces leaving behind a net excess of ions distributed near the wall. This region is known as an electric double layer (Bockris, 1970). The diffuse distribution of mobile ions, with a higher concentration ions in the region close to the adsorbed layer and more and more diffuse towards the neutral electrolyte are free to move when the fluid moves.

The seismic wave motion which generates the relative flow also induces a 'streaming' electrical current due to flow of double-layer ions. This induced streaming current acts as a current source in Maxwell's equations. The compressional waves in a homogeneous porous media contain a nonradiating electric field that is not detectable outside the wave pulse. The peaks and troughs cause a charge separation setting up electric fields of the Coulombic attraction type, that drives a conduction current that exactly balances the streaming current. Propagating electromagnetic waves are not generated since there is no current imbalance within the seismic pulse.

Divergence-free  $S$  waves cannot cause charge to separate since they do not induce changes in fluid pressure but there is relative fluid-solid motion through equi-voluminal grain accelerations. The induced streaming current sheets induce magnetic fields that generate very small, compared to the electric field associated with the P-wave pulse, electric fields of the induction type. When rotational waves propagate through homogeneous porous medium, it contains a measurable magnetic field within the pulse that is not detectable outside the seismic pulse. In homogeneous media a dipole antenna acts as a geophone measuring the nonradiating electric fields inside the compressional pulse when the pulse passes by. A magnetometer would act as a shear wave selective geophone measuring the non-radiating magnetic fields inside the rotational pulse when the pulse passes by.

Seismic waves that traverse a contrast in electrical and/or mechanical properties however form a complex dynamic current imbalance across the interface generating radiating

electromagnetic waves measurable at the earth's surface. Field data has been recorded that demonstrates that when seismic sources which generate seismic waves that propagate through the near surface sediment layers, convert at depth into electromagnetic disturbances that can be recorded (Thompson and Gist, 1991, 1993; Butler *et al.*, 1994; Mikhailov and Haartsen, 1996).

In this report, the macroscopic equations controlling such behavior will be numerically solved for the case of seismic point sources in a layered medium. Only an explosive pointsource will be numerically modeled, it will be shown however how to allow for other sources as well. A global matrix method (Chin *et al.*, 1984; Mal, 1988) is employed that solves simultaneously for all the macroscopic electromagnetic and poro-elastic wavefield properties. The *EM* field converted from seismic waves traversing boundaries are associated with a change in the following properties: changes in elastic properties (e.g., porosity, bulk and frame moduli, changes in fluid flow permeability, changes in fluid-chemistry that affect the amount of double layer ions free to move in the double layer (e.g., bulk free-ion concentration, pH)).

A thick, relative to the mechanical wavelengths, permeable sand layer example is presented to show the effect of a mechanical contrast on the mechanical and electromagnetic wavefield components. A fresh water/brine contrast model is used to show the effect of an electrical contrast on the mechanical and electromagnetic wavefield components. Both models are also used in the calculation of converted magnetic and electric field amplitudes

versus seismic source-antenna offset at different distances from the interface.

Snapshots in time are calculated to follow the conversion evolution of mechanical waves into electromagnetic waves. The rapid decay in amplitude with traveled distance of the converted electromagnetic signal driven by the seismic source with a seismic center frequency suggests the Vertical ElectroSeismic Profiling geometry, where antennas are positioned close to the target of interest. The last two numerical examples are calculations in this VESP geometry.

## 2. Macroscopic Coupled Electromagnetic and Poro-Elastic Field Equations

Assuming an  $e^{-i\omega t}$  dependence, Pride (1994) derived the following macroscopic fully coupled mechanical, electromagnetic equations and constitutive relations in volume averaged form describing the coupled field behavior in two phase porous medium,

$$\nabla \cdot \underline{\underline{\tau}}_B = -\omega^2 [\rho_B \underline{u}_s + \rho_f \underline{w}] + \underline{F} \quad (1)$$

$$\underline{\underline{\tau}}_B = [K_G \nabla \cdot \underline{u}_s + C \nabla \cdot \underline{w}] \underline{I} + G \left[ \nabla \underline{u}_s + \nabla \underline{u}_s^T - \frac{2}{3} \nabla \cdot \underline{u}_s \underline{I} \right] \quad (2)$$

$$-P = C \nabla \cdot \underline{u}_s + M \nabla \cdot \underline{w} \quad (3)$$

$$-i\omega \underline{w} = L(\omega) \underline{E} + \frac{k(\omega)}{\eta} [-\nabla P + \omega^2 \rho_f \underline{u}_s + \underline{f}] \quad (4)$$

$$\underline{J} = \sigma(\omega) \underline{E} + L(\omega) [-\nabla P + \omega^2 \rho_f \underline{u}_s + \underline{f}] \quad (5)$$

$$\nabla \times \underline{E} = i\omega \underline{B} \quad (6)$$

$$\nabla \times \underline{H} = -i\omega \underline{D} + \underline{J} + \underline{C} \quad (7)$$

$$\underline{D} = \epsilon_0 \left[ \frac{\phi}{\alpha_\infty} (\kappa_f - \kappa_s) + \kappa_s \right] \underline{E} \quad (8)$$

$$\underline{B} = \mu_0 \underline{H} \quad (9)$$

were  $\underline{E}$  is the electric field strength,  $\underline{H}$  is the magnetic field strength,  $\underline{B}$  is the magnetic flux density,  $\underline{D}$  is the electric displacement,  $\epsilon_0$  is the permittivity in free space,  $\mu_0$  is the permeability in free space,  $\kappa_f$  is the relative permittivity in the fluid,  $\kappa_s$  is the relative permittivity in the solid,  $\underline{\tau}_B$  is the bulk stress,  $P$  is the pressure in the pore fluid,  $\underline{u}_s$  is the displacement in the solid,  $\underline{w}$  is the relative fluid-solid motion and  $\underline{I}$  is the identity matrix.  $\underline{C}$  is an external current density source and,  $\underline{F}$  and  $\underline{f}$  are average bodyforces densities acting on the bulk and fluid phase respectively. Equations (1–4) characterize the mechanical wavefield behavior, with Eq (2) and (3) the deformation equations in the fluid and solid phase, respectively. Equations (5–9) characterize the electromagnetic wavefield behavior, with Eq (8) and (9) the electromagnetic constitutive relations. Equations (4) and (5) are the transport equations through which the mechanical wavefields are coupled to the electromagnetic wavefields. The coefficients in the flux equations relating the equations of mass, here fluid flow and current flow when there are potential and pressure gradients are the complex and frequency dependent conductivity of the two phase medium,  $\sigma(\omega)$ ,  $k(\omega)$  is the dynamic permeability,  $L(\omega)$  is the complex electrokinetic coupling coefficient, and  $\eta$  is the fluid viscosity. Isotropic complex and frequency dependent expressions for coefficients  $\sigma(\omega)$ ,  $k(\omega)$  and  $L(\omega)$  are in



Pride (1994). The first term in Eq (4) is the conduction current contribution and the second term is the streaming current contribution to the total current density,  $\underline{J}$ . The fact that the cross terms have the same coupling coefficient  $L(\omega)$  is a statement of Onsager reciprocity.

The coefficients in the deformation equations are,

$$K_G = H - \frac{4}{3}G = \frac{K_{fr} + \phi K_{fr} + (1 - \phi)K_s \Delta}{1 + \Delta} \quad (10)$$

$$C = \frac{K_f + K_s \Delta}{1 + \Delta} \quad (11)$$

$$M = \frac{1}{\phi} \frac{K_f}{1 + \Delta} \quad (12)$$

where the parameter  $\Delta$  is defined as,

$$\Delta = \frac{K_f}{\phi K_s^2} [(1 - \phi)K_s - K_{fr}] \quad (13)$$

The moduli  $K_{fr}$  and  $G$  are the bulk and shear moduli of the framework of the grains, when the fluid is absent. The frame moduli may either be considered experimentally determined or may be obtained from approximate theoretical models for specific pore grain geometries.  $C$  and  $M$  are the incompressibilities used by Biot (1962) and Pride (1992), they are complex and frequency dependent, allowing for losses in addition to those associated with relative flow.

### 3. Electro seismic Wavefield Description in an Isotropic Porous Layered Material

There are assumed to be  $ND$  layers. The fundamental input medium properties used in the numerical modeling that characterize each layer and determine all complex wavefield velocities, the complex and frequency dependent electrical conductivity and electrokinetic coupling coefficients, are: porosity, dc permeability, bulk modulus of the solid and fluid phase, the frame's bulk and shear modulus, the densities of the solid and fluid phase, the viscosity of the fluid phase, the temperature of the bulk material, the tortuosity, the salinity of the fluid and the relative permittivities of the solid and fluid phases.

First, the field equations describing the wave behavior in each layer are determined. A cylindrical coordinate system  $(r, \phi, z)$  with  $z$  being depth has been used since the geometry has azimuthal symmetry. The following definitions involving the horizontal components and horizontal derivatives are used (Hudson, 1969; Kennett, 1983),

$$u_V = \frac{1}{r} \left[ \frac{\partial}{\partial r} (ru_r) + \frac{\partial}{\partial \phi} u_\phi \right] \quad (14)$$

$$u_H = \frac{1}{r} \left[ \frac{\partial}{\partial r} (ru_\phi) - \frac{\partial}{\partial \phi} u_r \right] \quad (15)$$

$$\tau_{Vz} = \frac{1}{r} \left[ \frac{\partial}{\partial r} (r\tau_{rz}) + \frac{\partial}{\partial \phi} \tau_{\phi z} \right] \quad (16)$$

$$\tau_{Hz} = \frac{1}{r} \left[ \frac{\partial}{\partial r} (r\tau_{\phi z}) - \frac{\partial}{\partial \phi} \tau_{zr} \right] \quad (17)$$

$$\langle E, H \rangle_V = \frac{1}{r} \left[ \frac{\partial}{\partial r} (r \langle E, H \rangle_r) + \frac{\partial}{\partial \phi} \langle E, H \rangle_\phi \right] \quad (18)$$

$$\langle E, H \rangle_H = \frac{1}{r} \left[ \frac{\partial}{\partial r} (r \langle E, H \rangle_\phi) - \frac{\partial}{\partial \phi} \langle E, H \rangle_r \right] \quad (19)$$

$$\nabla_1^2 = \frac{1}{r} \frac{\partial}{\partial r} \left( r \frac{\partial}{\partial r} \right) + \frac{1}{r^2} \frac{\partial^2}{\partial \phi^2} \quad (20)$$

to rewrite the governing macroscopic coupled electromagnetic and poro-elastic field equations. To obtain the transform-domain field equations, the governing equations controlling the coupled electromagnetic-seismic, or electroseismic wavefield propagation are first Fourier transformed to the temporal frequency domain. A Finite Fourier Hankel transform is performed over the horizontal coordinates  $r$  and  $\phi$  thus providing a cylindrical wave decomposition.

This transform pair is defined as,

$$HF [\psi(r, \phi)] = \hat{\psi}(k, n) = \frac{1}{2\pi} \int_0^\infty dr \, r J_n(kr) \int_0^{2\pi} d\phi \, e^{-in\phi} \psi(r, \phi) \quad (21)$$

$$HF^{-1} [\hat{\psi}(k, n)] = \psi(r, \phi) = \int_0^\infty dk \, k \sum_{n=-N}^N J_n(kr) e^{in\phi} \hat{\psi}(k, n) \quad (22)$$

Note the property  $HF [\nabla_1^2 \psi] = -k^2 \hat{\psi}$ , (Watson, 1944). The magnitude  $N$  in the summation is determined by azimuthal symmetry of the point source. For spherically symmetric sources there is no azimuthal dependence, then  $N = 0$ . If the source can be described using an arbitrarily directed force vector, then  $N \leq 1$ , while if it can be described using a second order moment tensor, then  $N \leq 2$  (Kennett, 1983).

The final transform-domain field equations are obtained by eliminating those field components that are discontinuous across an interface between two media with different poro-elastic and/or electromagnetic medium properties. The resulting differential equations are written

in the form of a first-order ordinary matrix differential equation. In isotropic media the first-order ordinary differential equations decompose into two sets that describe *PSVTM* and *SHTE* coupled wavefield propagation. The compressional and vertical polarized rotational mechanical waves generate electrical currents in the *PSV* particle motion plane in homogeneous isotropic media. This couples to the electromagnetic wavefield components with *TM* polarization. We call this from now on the *PSVTM* coupled electroseismic wavefield case. The horizontal polarized rotational mechanical waves generate electrical currents in the *SH* particle motion plane in isotropic homogeneous porous media. This couples to the electromagnetic wavefield components with *TE* polarization.

An incoming wave at an interface separating two isotropic porous materials will generate four reflected and transmitted watypes ( $P_{fast}$ ,  $P_{slow}$ ,  $SV$ ,  $TM$ ) in each porous layer in the *PSVTM* case. Thus, eight boundary conditions need to be complied with, requiring the phase matching of eight wavefield components across the interface. In the *SHTE* case, an incoming wave at an interface generates two reflected and transmitted watypes ( $SH$ ,  $TE$ ). Thus, four boundary conditions need to be complied with, requiring the phase matching of four wavefield components across the interface. In Pride and Haartsen (1995) the electroseismic boundary conditions are derived from kinematic constraints and the conservations laws (linear momentum, conservation of mass and conservation of energy). The obtained boundary conditions were shown not to violate uniqueness of solution of an electroseismic boundary value problem. These derived boundary conditions require the following transform-domain

continuity displacement-stress-EM wavefield components in layer  $m$  to be continuous across its interfaces with other layers,

$$B_J^{(m;PSVTM)} = [\hat{u}_1, \hat{u}_z, \hat{w}_z, \hat{\tau}_1, \hat{\tau}_{zz}, \hat{S}, \hat{H}_2, \hat{E}_1]^T \quad (23)$$

$$B_J^{(m;SHTE)} = [\hat{u}_2, \hat{\tau}_2, \hat{H}_1, \hat{E}_2]^T \quad (24)$$

were the horizontal components are defined as follows,

$$\hat{u}_1 = \frac{\hat{u}_V}{ik} \quad \hat{\tau}_1 = \frac{\hat{\tau}_{Vz}}{ik} \quad \hat{H}_2 = \frac{\hat{H}_H}{ik} \quad \hat{E}_1 = \frac{\hat{E}_V}{ik} \quad (25)$$

$$\hat{u}_2 = \frac{\hat{u}_H}{ik} \quad \hat{\tau}_2 = \frac{\hat{\tau}_{Hz}}{ik} \quad \hat{H}_1 = \frac{\hat{H}_V}{ik} \quad \hat{E}_2 = \frac{\hat{E}_H}{ik} \quad (26)$$

The advantage of using these horizontal field components becomes clear if one wants to solve a line source parallel with the stratification instead of a pointsource. Working in the  $(x, y, z)$  cartesian coordinates, assuming the line source to be parallel with the  $y$  axis and taking a Fourier transform of the equations of motion with respect to  $x$ , a plane wave decomposition is now employed, results in exactly the same equations as are obtained when the following identification of the horizontal components in the displacement-stress-EM vectors are made:  $\hat{u}_1 = \hat{u}_x$ ,  $\hat{u}_2 = \hat{u}_y$ ,  $\hat{\tau}_1 = \hat{\tau}_{xz}$ ,  $\hat{\tau}_2 = \hat{\tau}_{yz}$ ,  $\hat{H}_H = \hat{H}_y$ ,  $\hat{H}_V = \hat{H}_x$ ,  $\hat{E}_H = \hat{E}_y$  and  $\hat{E}_V = \hat{E}_x$ . Thus, using this mapping, it follows that the solution of the first-order differential equations applies directly to the line source problem as well. Additionally, the cylindrical wave reflection/transmission coefficients to be obtained are necessarily identical to the plane wave coefficients.

The *PSVTM* continuity vector, Eq (25) is related to the medium at all depths  $z$  through an eight by eight system matrix  $A_{IJ}^{(PSVTM)}$ . The *SHTE* continuity vector, Eq (26) is related to the medium at all depths  $z$  through a four by four system matrix  $A_{IJ}^{(SHTE)}$ . The system matrix components depend on frequency and complex frequency dependent poro-elastic, electric and magnetic medium properties, the horizontal slowness  $p$  (note  $k = \omega p$ ) and the transport and electrokinetic coupling coefficients. After Hankel transforming Eq (6-3) and some algebra the following first-order linear differential matrix equations which describe the *PSVTM* case are obtained,

$$\frac{\partial}{\partial z} B_I^{(PSVTM)} = \begin{bmatrix} \underline{\underline{A}}^{(Biot;PSVTM)} & \underline{\underline{A}}^{(osmosis;PSVTM)} \\ \underline{\underline{A}}^{(electrokinetic;PSVTM)} & \underline{\underline{A}}^{(Maxwell;PSVTM)} \end{bmatrix} B_J^{(PSVTM)} \quad (27)$$

The first order differential matrix equation describing the *SHTE* case in the transform domain is,

$$\frac{\partial}{\partial z} B_I^{(SHTE)} = \begin{bmatrix} 0 & \frac{1}{G} & 0 & 0 \\ -\omega^2 (\beta - p^2 G) & 0 & 0 & 0 \\ \omega^2 L \rho_f & 0 & 0 & -i\omega \epsilon \left(1 - \frac{p^2}{\mu \epsilon}\right) \\ 0 & 0 & -i\omega \mu & 0 \end{bmatrix} B_J^{(SHTE)} \quad (28)$$

where the 6 by 6 *PSVTM* submatrix and the 2 by 2 *SHTE* submatrix

$$A_{IJ}^{(Biot;PSVTM)} = \begin{bmatrix} -i\omega p \underline{\underline{a}}_{11} & \underline{\underline{a}}_{12} \\ -\omega^2 \underline{\underline{a}}_{21} & -i\omega p \underline{\underline{a}}_{11}^T \end{bmatrix}, \quad A_{IJ}^{(Biot;SHTE)} = \begin{bmatrix} 0 & \frac{1}{G} \\ -\omega^2 (\beta - p^2 G) & 0 \end{bmatrix} \quad (29)$$

relate the mechanical stress-displacement wavefields with depth.

Where the 2 by 2 *PSVTM* submatrix and the 2 by 2 *SHTE* submatrix

$$A_{IJ}^{(Maxwell;PSVTM)} = \underline{a}_{33}, \quad A_{IJ}^{(Maxwell;SHTE)} = \begin{bmatrix} 0 & -i\omega \left(1 - \frac{p^2}{\mu\epsilon}\right) \\ -i\omega\mu & 0 \end{bmatrix} \quad (30)$$

relate the electric and magnetic wavefield components with depth.

Where the 6 by 2 *PSVTM* submatrix and the 2 by 2 *SHTE* submatrix

$$A_{IJ}^{(electrokinetic;PSVTM)} = \begin{bmatrix} -\omega^2 \underline{a}_{31} & -i\omega p \underline{a}_{32} \end{bmatrix} \quad (31)$$

$$A_{IJ}^{(electrokinetic;SHTE)} = \begin{bmatrix} \omega^2 L \rho_f & 0 \\ 0 & 0 \end{bmatrix}$$

relate the electric and magnetic wavefield components, converted from the mechanical wavefields, with depth.

And where the 2 by 6 *PSVTM* submatrix and the 2 by 2 *SHTE* submatrix

$$A_{IJ}^{(osmosis;PSVTM)} = \begin{bmatrix} \underline{a}_{13} \\ \underline{a}_{23} \end{bmatrix}, \quad A_{IJ}^{(osmosis;SHTE)} = \underline{0} \quad (32)$$

relate the mechanical wavefield components, converted from electric and magnetic wavefields, with depth.

The following matrices have been used,

$$\underline{a}_{11} = \begin{bmatrix} 0 & 1 & 0 \\ \alpha & 0 & 0 \\ -\beta & 0 & 0 \end{bmatrix}, \quad \underline{a}_{12} = \begin{bmatrix} \frac{1}{G} & 0 & 0 \\ 0 & \frac{M}{\Delta} & -\frac{C}{\Delta} \\ 0 & -\frac{C}{\Delta} & \frac{H}{\Delta} - \frac{p^2}{\rho_E} \end{bmatrix}, \quad \underline{a}_{13} = \underline{0} \quad (33)$$

$$\underline{a}_{21} = \begin{bmatrix} B - 2p^2G(1 + \alpha) & 0 & 0 \\ 0 & \rho_B & \rho_f \\ 0 & \rho_f & \rho_E \frac{\epsilon}{\epsilon - \rho_E L^2} \end{bmatrix}, \quad \underline{a}_{23} = \begin{bmatrix} 0 & 0 \\ 0 & 0 \\ -i\omega p \frac{\rho_E L}{\epsilon - \rho_E L^2} & 0 \end{bmatrix} \quad (34)$$

$$\underline{a}_{31} = \begin{bmatrix} L\rho_f & 0 & 0 \\ 0 & 0 & \frac{pL\rho_E}{\epsilon - \rho_E L^2} \end{bmatrix}, \quad \underline{a}_{32} = \begin{bmatrix} 0 & 0 & L \\ 0 & 0 & 0 \end{bmatrix} \quad (35)$$

$$\underline{a}_{33} = \begin{bmatrix} 0 & i\omega\epsilon \\ i\omega\mu \left(1 - \frac{p^2}{\mu[\epsilon - \rho_E L^2]}\right) & 0 \end{bmatrix}$$

The following coefficients have been used in the matrices above.

$$\alpha = 1 - \frac{2GM}{\Delta} \quad \beta = \frac{\rho_f}{\rho_E} - \frac{2GC}{\Delta} \quad (36)$$

$$\Delta = HM - C^2 \quad B = \rho_B - \frac{\rho_f^2}{\rho_E} \quad (37)$$

$$\epsilon = \epsilon_0 \kappa(\omega) + i \frac{\sigma(\omega)}{\omega} \quad (38)$$

## 4. The Global Matrix Method

To obtain the wavefields in each layer  $m$ , the following continuity conditions at each boundary are used,

$$\lim_{z \downarrow z_m} B_J^{(m+1)} - \lim_{z \uparrow z_m} B_J^{(m)} = 0 \quad m \neq s \quad (39)$$

At the source level  $z = z_s$ , where the source is positioned,  $B_J$  jumps by a finite amount. At the source level,

$$\lim_{z \downarrow z_s} B_J^{(s+1)} - \lim_{z \uparrow z_s} B_J^{(s)} = S_J \quad (40)$$



with  $S_J$  the source vector. First a linear transformation on each of the  $ND$  field vectors  $B_J^{(m)}$  is carried out. Through it, a field-vector-formalism is obtained in which a decomposition of  $B_I^{(m)}$  into up and downgoing fields is manifest. Let  $W_N^{(m;PSVTM)}$  be the eight by one vector and  $W_N^{(m;SHTE)}$  a four by one vector that is related to  $B_J^{(m)}$  by the linear transformation,

$$B_J^{(m)} = D_{J,N}^{(m)} W_N^{(m)} \quad (41)$$

where matrix  $D_{J,N}^{(m)}$  is subject to a convenient choice. From the theory of matrices  $D_{J,N}^{(m)}$  is taken the local eigenvector matrix for the system matrices  $A_{I,J}^{(m)}$  defined in Eq (27) and (28). In the  $PSVTM$  case the eigencolumn matrix, for each layer  $m$ , of the system matrix  $A_{I,J}^{(m;PSVTM)}$  is defined as,

$$D_{J,N}^{(m;PSVTM)} = [\underline{d}^{(m;-P_f,-P_s)}, \underline{d}^{(m;-SV,-TM)}, \underline{d}^{(m;+P_f,+P_s)}, \underline{d}^{(m;+SV,+TM)}] \quad (42)$$

$$= \begin{bmatrix} M_{P,Q}^{(m,PSVTM;-)} & M_{P,Q}^{(m,PSVTM;+)} \\ N_{P,Q}^{(m,PSVTM;-)} & N_{P,Q}^{(m,PSVTM;+)} \end{bmatrix} \quad (43)$$

where  $\underline{d}$  contains the eight by one eigenvectors  $b_J^{(m;\pm r)}$  with  $r \in P_{fast}, P_{slow}, SV, TM$ , the up and downgoing wavefields, shown in Eq (A-4) and (A-7) in Appendix A.  $M_{P,Q}^{(m,PSVTM;\pm)}$  and  $N_{P,Q}^{(m,PSVTM;\pm)}$  are four by four matrices.

In the  $SHTE$  case the eigencolumn matrix, for each layer  $m$  of the system matrix  $A_{I,J}^{(m;SHTE)}$  is defined as,

$$D_{J,N}^{(m;SHTE)} = [\underline{d}^{(m;-SH,-TE)}, \underline{d}^{(m;+SH,+TE)}] = \begin{bmatrix} M_{P,Q}^{(m,SHTE;-)} & M_{P,Q}^{(m,SHTE;+)} \\ N_{P,Q}^{(m,SHTE;-)} & N_{P,Q}^{(m,SHTE;+)} \end{bmatrix} \quad (44)$$

where  $\underline{d}$  contains the four by one eigenvectors  $b_j^{(m;\pm r)}$  with  $r \in SH, TE$ , the up and downgoing wavefields, shown in Eq (A-6) in Appendix A.

Substituting Eq (41) into the first-order differential matrix equation, Eq (27) and (28), and premultiplying the equation with  $D_{M,I}^{(m)-1}$  yields,

$$\frac{\partial}{\partial z} W_M^{(m)} = \left[ D_{M,I}^{(m)-1} A_{I,J}^{(m)} D_{J,N}^{(m)} - D_{M,I}^{(m)-1} \frac{\partial}{\partial z} D_{I,N}^{(m)} \right] W_N^{(m)}. \quad (45)$$

In a uniform medium the eigenvector components in  $D_{J,N}$  are independent of  $z$ , with the result that  $D_{M,I}^{(m)-1} \frac{\partial}{\partial z} D_{I,N}^{(m)}$  vanishes. Since  $D_{J,N}$  is taken the local eigenvector matrix for the system matrices  $A_{I,J}^{(m)}$  we obtain,

$$D_{M,I}^{(m)-1} A_{I,J}^{(m)} D_{J,N}^{(m)} = i\omega \Lambda_{M,N}^{(m)} \quad (46)$$

where  $\Lambda_{M,N}^{(m)}$  is a diagonal matrix of the eigenvalues  $q^{(m;\pm r)}$  of the system matrices  $A_{I,J}^{(m)}$ ,

$$\Lambda_{M,N}^{(m;PSVTM)} = \text{diag} \left[ q^{(m;-P_f)}, q^{(m;-P_s)}, q^{(m;-SV)}, q^{(m;-TM)}, \right. \\ \left. q^{(m;+P_f)}, q^{(m;+P_s)}, q^{(m;+SV)}, q^{(m;+TM)} \right] \quad (47)$$

$$\Lambda_{M,N}^{(m;SHTe)} = \text{diag} \left[ q^{(m;-SH)}, q^{(m;-TE)}, q^{(m;+SH)}, q^{(m;+TE)} \right] \quad (48)$$

The vector  $W_m^{(m)}$  is governed by the following differential equation,

$$\frac{\partial}{\partial z} W_M^{(m)} = i\omega \Lambda_{M,N}^{(m)} W_N^{(m)} \quad (49)$$

with solution,

$$W_M^{(m)} = \exp[i\omega q^{(m;-r)}(z - z_m)] W_N^{(m)}(z_{m-1}) \quad (50)$$

We define the following wave-propagator matrix,

$$\exp[i\omega q^{(m;-r)}(z - z_m)] = \begin{bmatrix} E_{P,Q}^{(m)} & 0 \\ 0 & E_{P,Q}^{(m)-1} \end{bmatrix} \quad (51)$$

with the  $E_{P,Q}^{(m)}$  matrices defined as,

$$E_{P,Q}^{(m;PSVTM)} = \text{diag} \left( \exp[i\omega q^{(m;P_f)} \Delta z], \exp[i\omega q^{(m;P_s)} \Delta z], \right. \\ \left. \exp[i\omega q^{(m;SV)} \Delta z], \exp[i\omega q^{(m;TM)} \Delta z] \right) \quad (52)$$

$$E_{P,Q}^{(m;SHTE)} = \text{diag} \left( \exp[i\omega q^{(m;SH)} \Delta z], \exp[i\omega q^{(m;TE)} \Delta z] \right) \quad (53)$$

with  $q^{(m;P_f,P_s)} = \sqrt{\frac{1}{v_{P_f,P_s}^2} - p^2}$ ,  $q^{(m;SV,SH)} = \sqrt{\frac{1}{v_{SV,SH}^2} - p^2}$  and  $q^{(m;TM,TE)} = \sqrt{\frac{1}{v_{TM,TE}^2} - p^2}$  the vertical slownesses for the compressional fast wave mode, the compressional slow wave mode, the vertical polarized shear wave mode, the horizontally polarized shear wave mode, the transverse magnetic *EM* mode and the transverse electric *EM* mode. The choice of branch cuts is defined according to the computational methods used to perform the inverse Fourier and Hankel transforms;  $\text{Im}(\omega q^{(m;P_f,P_s)}) > 0$ ,  $\text{Im}(\omega q^{(m;SV,SH)}) > 0$  and  $\text{Im}(\omega q^{(m;TM,TE)}) > 0$ .

The field vector  $W_N^{(m)}(z)$  in layer  $m$  is related to field vector  $W_N^{(m+1)}(z)$  in layer  $m + 1$  through the continuity conditions shown in Eq (39) and (40). The interface continuity conditions for  $m \neq s$  after applying the linear transformation are,

$$\begin{bmatrix} M_{P,Q}^{(m;-)} & M_{P,Q}^{(m;+)} \\ N_{P,Q}^{(m;-)} & N_{P,Q}^{(m;+)} \end{bmatrix} \begin{bmatrix} E_{P,Q}^{(m)} & 0 \\ 0 & E_{P,Q}^{(m)-1} \end{bmatrix} \begin{bmatrix} \underline{p}^{(m;-)} \\ \underline{p}^{(m;+)} \end{bmatrix} -$$

$$\begin{bmatrix} M_{P,Q}^{(m+1;-)} & M_{P,Q}^{(m+1;+)} \\ N_{P,Q}^{(m+1;-)} & N_{P,Q}^{(m+1;+)} \end{bmatrix} \begin{bmatrix} \underline{p}^{(m+1;-)} \\ \underline{p}^{(m+1;+)} \end{bmatrix} = \underline{0} \quad (54)$$

$$W_M^{(m;PSVTM)} = \begin{bmatrix} \underline{p}^{(m;PSVTM,-)} \\ \underline{p}^{(m;PSVTM,+)} \end{bmatrix}, \quad W_M^{(m;SHTE)} = \begin{bmatrix} \underline{p}^{(m;SHTE,-)} \\ \underline{p}^{(m;SHTE,+)} \end{bmatrix} \quad (55)$$

The radiation condition for halfspaces requires the conditions of no incoming waves from  $|z| \rightarrow \infty$ , implying  $\underline{p}^{(1;-)} = 0$  and  $\underline{p}^{(ND;+)} = 0$ .

The interface conditions at  $z = z_1$  become,

$$\begin{aligned} M_{P,Q}^{(1;+)} E_{P,Q}^{(1)-1} \underline{p}^{(1;+)} - M_{P,Q}^{(2;-)} \underline{p}^{(2;-)} - M_{P,Q}^{(2;+)} \underline{p}^{(2;+)} &= \underline{0} \\ N_{P,Q}^{(1;+)} E_{P,Q}^{(1)-1} \underline{p}^{(1;+)} - N_{P,Q}^{(2;-)} \underline{p}^{(2;-)} - N_{P,Q}^{(2;+)} \underline{p}^{(2;+)} &= \underline{0} \end{aligned}$$

At  $z = z_N$  the interface conditions are,

$$\begin{aligned} M_{P,Q}^{(ND-1;-)} E_{P,Q}^{(ND-1)} \underline{p}^{(ND-1;-)} + M_{P,Q}^{(ND-1;+)} E_{P,Q}^{(ND-1)-1} \underline{p}^{(ND-1;+)} - M_{P,Q}^{(ND;-)} \underline{p}^{(ND;-)} &= \underline{0} \\ N_{P,Q}^{(ND-1;-)} E_{P,Q}^{(ND-1)} \underline{p}^{(ND-1;-)} + N_{P,Q}^{(ND-1;+)} E_{P,Q}^{(ND-1)-1} \underline{p}^{(ND-1;+)} - N_{P,Q}^{(ND;-)} \underline{p}^{(ND;-)} &= \underline{0} \end{aligned}$$

To include a free surface, the free surface conditions for the mechanical wavefields and the ordinary electromagnetic boundary conditions at the porous medium-air interface need to be complied with. The mechanical normal and tangential stresses and pressure in the two phase medium have to vanish at the free surface, while the tangential electric and magnetic fields obey the porous medium-air boundary conditions. When we neglect the osmosis effect at the free surface, the up and downgoing fast, slow and, shear wave amplitudes can be

related through the vanishing of the stress and fluid traction boundary conditions. The up and downgoing electric and magnetic wavefields at the free surface are related through the ordinary electromagnetic boundary conditions. All downgoing wave type amplitudes can be related to the upgoing wave amplitudes and satisfy all free surface conditions. The reflected wavefield from the free surface are phase delayed to the interface below and included in the phase matching across this boundary.

In this analysis the following matrices are used. The  $3 \times 3$  matrix,  $S_{33}^{(1;\mp)}$  which contains the mechanical eigenvector components that relate the mechanical wavefield amplitudes to the normal and shear bulk stresses and pressure in the pore fluid. The  $2 \times 3$  matrix,  $U_{23}^{(1;\mp)}$  which contains the mechanical eigenvector components that relate the mechanical wavefield amplitudes to the tangential magnetical and electrical wavefields. The  $2 \times 2$  matrix,  $V_{22}^{(1)}$  which contains the electromagnetic eigenvector components that relate the EM wavefield amplitudes to the tangential magnetical and electrical wavefields in the porous medium. The  $2 \times 1$  matrix,  $W_{21}^{(0;-)}$  which contains the electromagnetic eigenvector components that relate the EM wavefield amplitudes to the tangential magnetical and electrical wavefields in the upper halfspace (air). Where the superscript 1 denotes the first layer, 0 the halfspace above the free surface, and  $\mp$  denotes eigenvector components relating to the down or up going wavefields. Using the eigencolumn components listed in Appendix A, the following matrices are constructed, necessary to express the reflected wavefield amplitudes from the

free surface in terms of upgoing wave amplitudes.

$$\begin{aligned}
S_{33}^{(1;\mp)} &= \begin{bmatrix} \pm 2i\omega p q v_{p_f} G & \pm 2i\omega p q v_{p_s} G & i\omega v_{sv} [q^2 - p^2] G \\ \frac{i\omega}{v_{p_f}} \left[ H - 2Gp^2 v_{p_f}^2 - \frac{\left[ \rho_B - \frac{H}{v_{p_f}^2} \right]}{\left[ \rho_f - \frac{C}{v_{p_f}^2} \right]} \right] & \frac{i\omega}{v_{p_s}} \left[ H - 2Gp^2 v_{p_s}^2 - \frac{\left[ \rho_B - \frac{H}{v_{p_s}^2} \right]}{\left[ \rho_f - \frac{C}{v_{p_s}^2} \right]} \right] & i\omega v_{sv} [q^2 - p^2] G \\ \frac{i\omega}{v_{p_f}} \left[ C - \frac{\left[ \rho_B - \frac{H}{v_{p_f}^2} \right]}{\left[ \rho_f - \frac{C}{v_{p_f}^2} \right]} M \right] & \frac{i\omega}{v_{p_s}} \left[ C - \frac{\left[ \rho_B - \frac{H}{v_{p_s}^2} \right]}{\left[ \rho_f - \frac{C}{v_{p_s}^2} \right]} M \right] & 0 \end{bmatrix} \\
U_{23}^{(1;\mp)} &= \begin{bmatrix} 0 & 0 & -\frac{i\omega L G \rho_E}{v_{sv} \rho_f} \frac{\left[ \frac{1}{v_{sv}^2} - \frac{\rho_B}{G} \right]}{\left[ \frac{1}{v_{sv}^2} - \epsilon \mu \right]} \\ -\frac{i\omega \rho_E L p v_{p_f}}{\epsilon} \frac{\left[ \rho_B - \frac{H}{v_{p_f}^2} \right]}{\left[ \rho_f - \frac{C}{v_{p_f}^2} \right]} & -\frac{i\omega \rho_E L p v_{p_s}}{\epsilon} \frac{\left[ \rho_B - \frac{H}{v_{p_s}^2} \right]}{\left[ \rho_f - \frac{C}{v_{p_s}^2} \right]} & \mp i\omega q v_{sv} L G \mu \frac{\rho_E}{\rho_f} \frac{\left[ \frac{1}{v_{sv}^2} - \frac{\rho_B}{G} \right]}{\left[ \frac{1}{v_{sv}^2} - \epsilon \mu \right]} \end{bmatrix} \\
V_{22}^{(1)} &= \begin{bmatrix} -\frac{i\omega L G \rho_E}{v_{tm} \rho_f} \frac{\left[ \frac{1}{v_{tm}^2} - \frac{\rho_B}{G} \right]}{\left[ \frac{1}{v_{tm}^2} - \epsilon \mu \right]} & -\frac{i\omega L G \rho_E}{v_{tm} \rho_f} \frac{\left[ \frac{1}{v_{tm}^2} - \frac{\rho_B}{G} \right]}{\left[ \frac{1}{v_{tm}^2} - \epsilon \mu \right]} \\ -i\omega q v_{tm} L G \mu \frac{\rho_E}{\rho_f} \frac{\left[ \frac{1}{v_{tm}^2} - \frac{\rho_B}{G} \right]}{\left[ \frac{1}{v_{tm}^2} - \epsilon \mu \right]} & i\omega q v_{tm} L G \mu \frac{\rho_E}{\rho_f} \frac{\left[ \frac{1}{v_{tm}^2} - \frac{\rho_B}{G} \right]}{\left[ \frac{1}{v_{tm}^2} - \epsilon \mu \right]} \end{bmatrix} \\
W_{21}^{(0;-)} &= \begin{bmatrix} -q v_{tm} \\ \sqrt{\frac{\epsilon}{\mu}} \end{bmatrix} \tag{56}
\end{aligned}$$

The up and downgoing mechanical wavefield amplitudes in the first layer, are the fast wave amplitudes,  $p_1^{(1,\pm)}$ , the shear wave amplitudes,  $p_2^{(1,\pm)}$  and the slow wave amplitudes,  $p_3^{(1,\pm)}$ , which can be related through the vanishing stress and fluid traction boundary conditions at the free surface.

$$p_{1-3}^{(1;-)} = - \left[ S_{33}^{(1;-)} \right]^{-1} S_{33}^{(1;+)} p_{1-3}^{(1;+)} \tag{57}$$

The electromagnetic boundary conditions are the usual continuity of the magnetic,  $H_\phi$ , and electric,  $E_r$ , components of the electromagnetic  $TM$  mode. The radiation in the space above the free surface requires the condition of no incoming  $EM$  waves from  $z \rightarrow -\infty$ , implying  $p_4^{(0;-)} = 0$ , downgoing  $TM$  wave amplitude is zero. The  $EM$  boundary conditions at the free surface are expressed as follows,

$$U_{23}^{(1;-)} p_{1-3}^{(1;-)} + U_{23}^{(1;+)} p_{1-3}^{(1;+)} + V_{22}^{(1)} \begin{bmatrix} p_4^{(1;-)} \\ p_4^{(1;+)} \end{bmatrix} = W_{21}^{(0;+)} \quad (58)$$

Using Eq (57), the following relation between the up and downgoing  $EM$  wave amplitudes propagating in the first layer can be obtained.

$$\begin{bmatrix} p_4^{(1;-)} \\ p_4^{(1;+)} \end{bmatrix} = \begin{bmatrix} V_{22}^{(1)} \end{bmatrix}^{-1} \left( W_{21}^{(0;-)} p_4^{(0;+)} - \left[ -U_{23}^{(1;-)} \left[ S_{33}^{(1;-)} \right]^{-1} S_{33}^{(1;+)} p_{1-3}^{(1;+)} + U_{23}^{(1;+)} p_{1-3}^{(1;+)} \right] \right) \quad (59)$$

Eliminating the  $p_4^{(0;+)}$  amplitude, the downgoing  $TM$  amplitude in the first layer can be expressed in terms of the upgoing  $TM$  and mechanical wavefield amplitudes.

$$\begin{aligned} p_4^{(1;-)} &= \frac{1}{\det(V_{22}^{(1)})} \left[ \Theta \left( \det(V_{22}^{(1)}) p_4^{(1;+)} + \Xi(2, 1) p_1^{(1;+)} + \Xi(2, 2) p_1^{(1;+)} + \Xi(2, 3) p_3^{(1;+)} \right) \right. \\ &\quad \left. - \Xi(1, 1) p_1^{(1;+)} - \Xi(1, 2) p_2^{(1;+)} - \Xi(1, 3) p_3^{(1;+)} \right] \end{aligned} \quad (60)$$

With,

$$\Theta = \frac{V_{22}^{(1)}(2, 2) W_{21}^{(0;-)}(1) - V_{22}^{(1)}(1, 2) W_{21}^{(0;-)}(2)}{-V_{22}^{(1)}(2, 1) W_{21}^{(0;-)}(1) + V_{22}^{(1)}(1, 1) W_{21}^{(0;-)}(2)} \quad (61)$$

$$\Xi_{23} = -U_{23}^{(1;-)} \left[ S_{33}^{(1;-)} \right]^{-1} S_{33}^{(1;+)} p_{1-3}^{(1;+)} + U_{23}^{(1;+)} p_{1-3}^{(1;+)} \quad (62)$$

Equations (57) and (60) relate the upgoing wave amplitudes to the downgoing wave amplitudes satisfying the free surface conditions. The downgoing wave fields reflected from the free surface are phase delayed to the next interface and included in its boundary condition.

Collecting all interface condition equations in one matrix, a  $(ND-1) \times 8$  by  $(ND-1) \times 8$  dimensional global matrix is obtained in the *PSVTM* case and a  $(ND-1) \times 4$  by  $(ND-1) \times 4$  dimensional global matrix in the *SHTE* case. To obtain the up and downgoing amplitudes in all layers simultaneously in both *PSVTM* and *SHTE* cases, the global matrix needs to be inverted. The obtained global matrix is identical in shape to the matrix obtained for a radiating upper halfspace. Inverting the global matrix yields only the upgoing wave amplitudes in the first layer. The downgoing wave fields are calculated using Eq (57) and (60). The physical wavefields at the receivers are obtained by substituting the inverted up and downgoing amplitudes in each layer into Eq (41) and propagate them to the receiver location in the layer.

The global matrix formulation was developed by Chin *et al.* (1984). The global matrix formulation has several important features: (1) Multiple sources can be treated, the produced wavefields are simply superposed; (2) The up and down going wavefield coefficients are simultaneously solved for in all layers, therefore the wavefield is known to all receivers at all places in the medium; (3) Time stability problems do not occur because decaying exponents are needed only. The Thomson-Haskell propagator matrix approach (Schmidt and Tango, 1986) does not have these advantageous features.



The global matrix system that needs to be solved is,

$$\begin{bmatrix} \underline{\underline{M}}^{(1;+)} \underline{\underline{E}}^{(1)-1} & -\underline{\underline{M}}^{(2;-)} & -\underline{\underline{M}}^{(2;+)} & & \\ \underline{\underline{N}}^{(1;+)} \underline{\underline{E}}^{(1)-1} & -\underline{\underline{N}}^{(2;-)} & -\underline{\underline{N}}^{(2;+)} & & \\ & & & & \\ & \underline{\underline{M}}^{(s;-)} \underline{\underline{E}}^{(s)} & \underline{\underline{M}}^{(s;+)} \underline{\underline{E}}^{(s)-1} & -\underline{\underline{M}}^{(s+1;-)} & -\underline{\underline{M}}^{(s+1;+)} \\ & \underline{\underline{N}}^{(s;-)} \underline{\underline{E}}^{(s)} & \underline{\underline{N}}^{(s;+)} \underline{\underline{E}}^{(s)-1} & -\underline{\underline{N}}^{(s+1;-)} & -\underline{\underline{N}}^{(s+1;+)} \\ & & & & \\ & & \underline{\underline{M}}^{(nd-1;-)} \underline{\underline{E}}^{(nd-1)} & \underline{\underline{M}}^{(nd-1;+)} \underline{\underline{E}}^{(nd-1)-1} & -\underline{\underline{M}}^{(nd;-)} \\ & & \underline{\underline{N}}^{(nd-1;-)} \underline{\underline{E}}^{(nd-1)} & \underline{\underline{N}}^{(nd-1;+)} \underline{\underline{E}}^{(nd-1)-1} & -\underline{\underline{N}}^{(nd;-)} \end{bmatrix} \underline{\underline{W}} = \begin{bmatrix} \underline{\underline{0}} \\ \underline{\underline{0}} \\ \\ \underline{\underline{S}}^- \\ \underline{\underline{S}}^+ \\ \\ \underline{\underline{0}} \\ \underline{\underline{0}} \end{bmatrix}$$

Chin *et al.* (1984) show that the Thomson-Haskell method (Thomson, 1950; Haskell, 1953) can be viewed as treating the coefficient matrix of the linear system in a block diagonal form and applying a forward marching algorithm for its solution. Chin's formulation is a shooting method for a two point boundary value problem. Gaussian elimination with partial pivoting yields stable solutions. To avoid time stability problems (exploding exponentials) the  $\underline{\underline{W}}_M$  vector is multiplied with a diagonal phase matrix  $F_{IJ}$  that cancels the potentially unstable upgoing wave phase factors.

$$F_{IJ} = \text{diag} \left[ E_{P,Q}^{(1)}, I_{P,Q}, E_{P,Q}^{(2)}, \dots, E_{P,Q}^{(ND)}, I_{P,Q} \right] \quad (63)$$

where  $I_{P,Q}$  is the identity matrix. If we define  $W_M = F_{MN} X_N$ ,  $X_N$  can be shown to satisfy,

$$\begin{bmatrix} \underline{\underline{M}}^{(1;+)} & -\underline{\underline{M}}^{(2;-)} & -\underline{\underline{M}}^{(2;+)} \underline{\underline{E}}^{(2)} \\ \underline{\underline{N}}^{(1;+)} & -\underline{\underline{N}}^{(2;-)} & -\underline{\underline{N}}_{P,Q}^{(2;+)} \underline{\underline{E}}^{(2)} \\ & & \\ & \underline{\underline{M}}^{(s;-)} \underline{\underline{E}}^{(s)} & \underline{\underline{M}}^{(s;+)} & -\underline{\underline{M}}^{(s+1;-)} & -\underline{\underline{M}}^{(s+1;+)} \underline{\underline{E}}^{(s+1)} \\ & \underline{\underline{N}}^{(s;-)} \underline{\underline{E}}^{(s)} & \underline{\underline{N}}^{(s;+)} & -\underline{\underline{N}}^{(s+1;-)} & -\underline{\underline{N}}^{(s+1;+)} \underline{\underline{E}}^{(s+1)} \\ & & & & \\ & & \underline{\underline{M}}^{(nd-1;-)} \underline{\underline{E}}^{(nd-1)} & \underline{\underline{M}}^{(nd;+)} & -\underline{\underline{M}}^{(nd;-)} \\ & & \underline{\underline{N}}^{(nd-1;-)} \underline{\underline{E}}^{(nd-1)} & \underline{\underline{N}}^{(nd-1;+)} & -\underline{\underline{N}}^{(nd;-)} \end{bmatrix} \underline{\underline{X}} = \begin{bmatrix} \underline{\underline{0}} \\ \underline{\underline{0}} \\ \\ \underline{\underline{S}}^- \\ \underline{\underline{S}}^+ \\ \\ \underline{\underline{0}} \\ \underline{\underline{0}} \end{bmatrix}$$

All terms that contained  $\exp[-i\omega q^{(m;P_f,P_s)} \Delta z]$ ,  $\exp[-i\omega q^{(m;SV,SH)} \Delta z]$ ,  $\exp[-i\omega q^{(m;TM,TE)} \Delta z]$  are eliminated. These exponentials cause numerical instability when the wavefield goes evanescent (Dunkin, 1965; Kennett, 1983; Schmidt and Tango, 1986).

## 5. Point Forces in a Poro-Elastic Stratified Medium

To model a general source, the moment tensor representing a body force equivalent in a poro-elastic medium has been used. Since the effect of the source is an internal process within a volume  $V$ , its total momentum and total angular momentum must be conserved (Aki and Richards, 1980). Therefore, the total force and momentum about any fixed point must be zero (i.e.,  $\int_V \underline{\underline{h}}(\underline{\underline{r}}) dV(\underline{\underline{r}}) = 0$  and  $\int_V \underline{\underline{h}}(\underline{\underline{r}}) \times (\underline{\underline{r}} - \underline{\underline{r}}_s) dV(\underline{\underline{r}}) = 0$ , with  $\underline{\underline{h}}$  a body force and  $\underline{\underline{r}}_s$  a fixed point in space). The above conditions imply the following body force equivalent,

$$h_j = M_{jk} \frac{\partial}{\partial x_k} \delta(\underline{r} - \underline{r}_s) \wedge M_{jk} = M_{kj}.$$

The following equation has to be evaluated when a cylindrical coordinate system is used,

$$\underline{h} = \underline{\underline{M}} \cdot \nabla \delta(\underline{r} - \underline{r}_s) = \begin{bmatrix} m_{rr} & m_{r\phi} & m_{rz} \\ m_{\phi r} & m_{\phi\phi} & m_{\phi z} \\ m_{zr} & m_{z\phi} & m_{zz} \end{bmatrix} \begin{bmatrix} \frac{\partial}{\partial r} \\ \frac{1}{r} \frac{\partial}{\partial \phi} \\ \frac{\partial}{\partial z} \end{bmatrix} \frac{\delta(r)}{r} \delta(\phi) \delta(z - z_s) \quad (64)$$

### 5.1. Mechanical Point Sources

First an explosion source, vertical line source and vertical dipole source uniformly acting on the solid frame and pore fluid are derived. These sources have due to symmetry no angular dependence. Then a couple source acting in the  $z$  direction with a spacing between the forces in the  $r$  direction, having angular dependence is outlined. Sources uniformly acting on the two phase medium are given by,

$$\underline{H} = \underline{h} = m \nabla \delta(\underline{r} - \underline{r}_s) = m \nabla \left[ \frac{\delta(r)}{r} \delta(\phi) \delta(z - z_s) \right] \quad (65)$$

with  $\underline{H}$  a source acting on the bulk material and  $\underline{h}$  a source acting on the pore fluid phase of the porous medium.

In component form the explosion source is given by,

$$h_r = m \frac{\partial}{\partial r} \left[ \frac{\delta(r)}{r} \right] \delta(\phi) \delta(z - z_s) \quad (66)$$

$$h_\phi = m \frac{\delta(r)}{r^2} \frac{\partial}{\partial \phi} [\delta(\phi)] \delta(z - z_s) \quad (67)$$

$$h_z = m \frac{\delta(r)}{r} \delta(\phi) \frac{\partial}{\partial z} [\delta(z - z_s)] \quad (68)$$

The horizontal component of the explosion source using definition 14 reads,

$$h_V = \frac{1}{r} \left[ \frac{\partial}{\partial r}(r h_r) + \frac{\partial}{\partial \phi} h_\phi \right] = m \delta(z - z_s) \nabla_1^2 \left[ \frac{\delta(r) \delta(\phi)}{r} \right] \quad (69)$$

The horizontal and vertical component of the explosion source after Hankel transformation and mapping on a plane wave description read,

$$\hat{h}_1 = \frac{\hat{h}_V}{i\omega p} = i k m \delta(z - z_s) \quad (70)$$

$$\hat{h}_z = m \frac{\partial}{\partial z} \delta(z - z_s) \quad (71)$$

The vertical line source components are given by 70 and  $\hat{h}_z = 0$  and the vertical dipole force is given by  $\hat{h}_1 = 0$  and 71.

A vertical couple source in the  $z$  direction with a spacing in between the forces in the  $r$  direction is given by,

$$h_r = h_\phi = 0, \quad h_z = m \frac{\partial}{\partial r} \left[ \frac{\delta(r)}{r} \right] \delta\phi \frac{\partial}{\partial z} \delta(z - z_s). \quad (72)$$

The vertical component of the vertical couple source after Hankel transformation (Sneddon, 1951), and mapping on a plane wave description read,

$$\hat{h}_1 = 0, \quad \hat{h}_z = \pm \frac{\partial}{\partial z} \delta(z - z_s) \quad (73)$$

The effect of a general mechanical point source in a stratified porous medium is accommodated by specifying a jump in the displacement stress vector  $B_J$ , across a horizontal plane containing the source (Hudson, 1969; Kennett, 1983).

To obtain this jump vector, the governing poro-elastic constitutive Eq (2) and (3), and the Fourier transformed equations of motion with a point source uniformly acting on the solid frame and pore fluid in a poro-elastic medium,

$$-\omega^2 [\rho_B \underline{u} + \rho_f \underline{w}] = \nabla \cdot \underline{\tau} + \underline{H} \quad (74)$$

$$-\omega^2 [\rho_f \underline{u} + \rho_E \underline{w}] = -\nabla P + \underline{h} \quad (75)$$

are Hankel transformed and manipulated into a set of equations that have all derivatives with respect to  $z$  on the left hand side, and a right hand side identical to the mechanical submatrix of the electroseismic system matrix 29. The first set describes the change in  $z$  of the field quantities  $[\hat{u}_1, \hat{u}_z, \hat{w}_z, \hat{\tau}_1, \hat{\tau}_{zz}, \hat{S}]$ , where the mapping given in Eq (25), (26) is applied to describe the  $P_f - P_s - SV$  case,

$$\frac{\partial}{\partial z} \begin{bmatrix} \hat{u}_1 \\ \hat{u}_z \\ \hat{w}_z \\ \hat{\tau}_1 \\ \hat{\tau}_{zz} \\ \hat{S} \end{bmatrix} = A_{IJ}^{(Biot;PSVTM)} \begin{bmatrix} \hat{u}_1 \\ \hat{u}_z \\ \hat{w}_z \\ \hat{\tau}_1 \\ \hat{\tau}_{zz} \\ \hat{S} \end{bmatrix} + \begin{bmatrix} 0 \\ 0 \\ 0 \\ 0 \\ \hat{H}_z \\ \hat{h}_z \end{bmatrix} + \begin{bmatrix} 0 \\ 0 \\ 0 \\ \hat{H}_1 - \frac{\rho_f}{\rho_E} \hat{h}_1 \\ 0 \\ 0 \end{bmatrix} \quad (76)$$

where  $A_{IJ}^{(Biot;PSVTM)}$  is defined in Eq (29). To include some form of source in the stratification we must solve the following inhomogeneous equation,

$$\underline{B}(z) = \underline{F}(z) \quad (77)$$

First we multiply Eq (77) through with a propagator matrix  $\underline{\underline{P}}^{-1}(z, z_s)$  from the left hand side to obtain an integration factor.

$$\underline{\underline{P}}^{-1}(z, z_s) \left[ \frac{\partial}{\partial z} \underline{B}(z) \right] - \left[ \frac{\partial}{\partial z} \underline{\underline{P}}^{-1}(z, z_s) \right] \underline{B}(z) = \underline{P}(z_s, z) \underline{F}(z) \quad (78)$$

where we have used the relationship  $\underline{\underline{P}}(z_s, z) = \underline{\underline{P}}^{-1}(z, z_s)$ .

Then we integrate with respect to  $z$  and multiply with  $\underline{P}(z, z_s)$ , we obtain,

$$\underline{B}(z) = \underline{P}(z, z_s) \underline{B}(z_s) + \int_{z_s}^z d\zeta \underline{P}(z, \zeta) \underline{F}(\zeta) \quad (79)$$

A point source can be manipulated into some dipolar contribution (Kennett, 1983).

This description is given by,

$$F_I(z_s) = F_I^{(1)} \delta(z - z_s) + F_I^{(2)} \frac{\partial}{\partial z} \delta(z - z_s) \quad (80)$$

with  $F_I^{(1)}$  and  $F_I^{(2)}$  the dipolar contributions. Substituting Eq (80) into Eq (79), we obtain,

$$\begin{aligned} \int_{z_s}^z d\zeta \underline{P}(z, \zeta) \left[ F_I^{(1)} \delta(z - z_s) + F_I^{(2)} \frac{\partial}{\partial z} \delta(z - z_s) \right] = \\ H(z - z_s) \underline{P}(z, z_s) \left[ \underline{P}(z_s, z_s) \underline{F}^{(1)} - \frac{\partial}{\partial \zeta} \underline{P}(z_s, \zeta) \Big|_{\zeta=z_s} \underline{F}^{(2)} \right] \end{aligned} \quad (81)$$

with  $H(z)$  the Heaviside step function.

Using the relationships,  $\underline{P}(z_s, \zeta) = \underline{\underline{P}}^{-1}(z, z_s)$  and  $\frac{\partial}{\partial \zeta} \underline{\underline{P}}^{-1}(z, z_s) = -\underline{\underline{P}}^{-1}(z, z_s) \underline{A}(p, z)$ , we obtain a displacement-stress jump vector condition across a source plane.

$$S_I(z_s) = \hat{\phi}(\omega) [B_I(z_s^+) - B_I(z_s^-)] = \hat{\phi}(\omega) [F_I^{(1)} + A_{I,J}^{(Biot,PSVTM)}(p, z_s) F_J^{(2)}] \quad (82)$$

with  $\hat{\phi}(\omega)$ , the Fourier transform of the source signature  $\phi(t)$ .

The final displacement-stress jump representations of some mechanical point sources in a poro-elastic isotropic medium are,

Explosive point source:

$$S_I^{(P_f P_s SV)}(z_s) = \hat{\phi}(\omega) \left[ 0, \frac{m}{\Delta}(M - C), \frac{m}{\Delta} \left( H - C - \frac{\Delta p^2}{\rho_E} \right), i\omega p m \left( 1 - \frac{\rho_f}{\rho_E} + \beta - \alpha \right), 0, 0 \right]^T \quad (83)$$

Vertical line source:

$$S_I^{(P_f P_s SV)}(z_s) = \hat{\phi}(\omega) \left[ 0, 0, 0, i\omega p m \left( 1 - \frac{\rho_f}{\rho_E} \right), 0, 0 \right]^T \quad (84)$$

Vertical couple source:

$$S_I^{(P_f P_s SV)}(z_s) = \hat{\phi}(\omega) \left[ 0, \pm\omega p m \frac{(M - C)}{\Delta}, \pm\omega p \frac{m}{\Delta} \left( H - C - \frac{\Delta p^2}{\rho_E} \right), \pm i\omega^2 p^2 m (\beta - \alpha), 0, 0 \right]^T \quad (85)$$

Vertical dipole source:

$$S_I^{(P_f P_s SV)}(z_s) = \hat{\phi}(\omega) \left[ 0, \frac{m}{\Delta}(M - C), \frac{m}{\Delta} \left( H - C - \frac{\Delta p^2}{\rho_E} \right), i\omega p m \left( 1 - \frac{\rho_f}{\rho_E} \right), 0, 0 \right]^T \quad (86)$$

## 5.2. Electromagnetic Point Sources

The effect of an electrical point source in a stratified porous medium is accommodated by specifying a jump in the electromagnetic field component vector  $[\hat{H}_2, \hat{E}_1]^T$  across a horizontal

plane containing the source. To obtain this jump vector, Maxwell's equations with an external current source  $\underline{C}$  in Fourier transform domain are Hankel transformed and manipulated into a set of equations that have all derivatives with respect to  $z$  on one side.

$$\frac{\partial}{\partial z} \begin{bmatrix} \hat{H}_2 \\ \hat{E}_1 \end{bmatrix} = \begin{bmatrix} 0 & i\omega\epsilon \\ i\omega\mu \left(1 - \frac{p^2}{\mu\epsilon}\right) & 0 \end{bmatrix} \begin{bmatrix} \hat{H}_2 \\ \hat{E}_1 \end{bmatrix} + \begin{bmatrix} 0 \\ \frac{p\hat{C}_z}{\epsilon} \end{bmatrix} + \begin{bmatrix} -\hat{C}_1 \\ 0 \end{bmatrix} \quad (87)$$

Using  $\hat{C}_1 = 0$  and  $\hat{C}_z = m \frac{\partial}{\partial z} \delta(z - z_s)$  and Eq (82) with  $A_{I,J}^{(Biot;PSVTM)}$  replaced by  $A_{I,J}^{(Maxwell;PSVTM)}$  the jump representation of a vertical electric dipole source is obtained.

$$S_I^{(TM)}(z_s) = \hat{\phi}(\omega) [i\omega pm, 0]^T. \quad (88)$$

A dipole current source produces an electromagnetic field that is expected to generate seismic waves when it traverses an interface at depth. In Pride and Haartsen (1995) it is shown, using a reciprocity argument, that in order to detect a seismic displacement of the order of  $10^{-7} m$  a  $10 Cm$  dipole moment is needed to produce an electric field on the order of  $10^8 V/m$  at a distance  $10 m$  from the source. Electromagnetic waves do generate mechanical wavefields at depth that are possibly measurable at the earth's surface. This very small conversion from electromagnetic waves into mechanical waves can be numerically simulated.

## 6. Transformation Back to the Space Time Domain

In this section the back transformation to the space-time domain of the displacement-stress-EM vector is performed. An inverse Fourier transform is applied to go back to the time



domain. An inverse Hankel transform is applied to obtain the 3D spatial dependence of the displacements, stresses, electric and magnetic fields. The horizontal components of the displacements, stresses, electric and magnetic fields require additional integration over  $r$  and  $\phi$  to obtain,  $u_r, u_\phi, \tau_{\phi z}, \tau_{rz}, H_r, H_\phi$  and  $E_r, E_\phi$  due to the definitions of  $u_V, u_H, \tau_{Vz}, \tau_{Hz}, H_V, H_H$  and  $E_V, E_H$ .

$$u_z(\omega, r, \phi, z) = \int_0^\infty k dk \sum_{n=-N}^N [J_n(kr) \hat{u}_z(\omega, k, n, z)] e^{in\phi} \quad (89)$$

Identical relations exist for  $w_z, \tau_{zz}$  and  $S = -P$ . The horizontal components may be recovered using the following equations (Kennett, 1983),

$$\begin{aligned} u_r(\omega, r, \phi, z) &= \int_0^\infty k dk \sum_{n=-N}^N \left[ \frac{n}{kr} J_n(kr) \hat{u}_2(\omega, k, n, z) \right. \\ &\quad \left. - i J'_n(kr) \hat{u}_1(\omega, k, n, z) \right] e^{in\phi} \end{aligned} \quad (90)$$

$$\begin{aligned} u_\phi(\omega, r, \phi, z) &= \int_0^\infty k dk \sum_{n=-N}^N \left[ \frac{n}{kr} J_n(kr) \hat{u}_1(\omega, k, n, z) \right. \\ &\quad \left. + i J'_n(kr) \hat{u}_2(\omega, k, n, z) \right] e^{in\phi} \end{aligned} \quad (91)$$

Identical relations exist for  $\tau_{rz}, \tau_{\phi z}$  in terms of  $\hat{\tau}_1$  and  $\hat{\tau}_2$ , for  $E_r, E_\phi$  in terms of  $\hat{E}_1$  and  $\hat{E}_2$  and  $H_r, H_\phi$  in terms of  $\hat{H}_1$  and  $\hat{H}_2$ . The above representations may be regarded as a superposition of cylindrical waves whose order dictates the nature of their azimuthal modulation. At each frequency and angular order the radial contribution is obtained by superposing all horizontal wavenumbers  $k$ . This corresponds to including all propagating waves at the level  $z$  within the stratification, from vertically to purely horizontal traveling waves including the

evanescent waves. At any particular distance  $r$  the relative contributions of the wavenumbers are imposed by the radial phase functions  $J_n(kr)$ .

The integrals (89), (90), and (91) are evaluated by the discrete summation over many wavenumbers or the so called Discrete Wavenumber Method (Bouchon and Aki, 1977).

The discretization of the radial wavenumber  $k$  in cylindrical coordinates introduces periodicity into the source distribution. The original single source problem changes after discretization into periodic concentric sources around the original source. The periodicity of these sources or the distance between two adjacent circular sources,  $L$ , is related to the discretization interval of the wavenumber,  $\Delta k$ , by the sampling relation,

$$L = \frac{2\pi}{\Delta k} \quad (92)$$

$L$  and therefore  $\Delta k$  is determined by assuming a receiver located at  $x_r = (r_0, z_0)$  and a source at  $x_s = (0, z_s)$  on the symmetry axes of the medium configuration. Given the time window to record radiated waves from 0 to  $t_{max}$ , 'pseudo' waves radiated from the periodic sources are not allowed to enter this time window. This requirement is,

$$\sqrt{(L - r_0)^2 + (z_0 - z_s)^2} > v_{fastest} t_{max} \quad (93)$$

or

$$L > r_0 + \sqrt{v_{fastest}^2 t_{max}^2 - (z_0 - z_s)^2} \quad (94)$$

The sampling equation becomes now,

$$\Delta k < \frac{2\pi}{r_0 + \sqrt{v_{fastest}^2 t_{max}^2 - (z_0 - z_s)^2}} \quad (95)$$

The above equation is the criterion for choosing the sample rate for the discrete wavenumber summation.

To perform the summation the singularities of the integrands are moved further from the real  $k$  axes. This is done by adding a small imaginary part to the real frequency (analytic continuation into the complex plane), i.e.,  $\omega = \omega_R + i\omega_I$  with  $\omega_I > 0$ . If  $e^{i\omega t}$  was used in the time to frequency transformation there would be a minus sign for the imaginary part of the frequency. The effect of complex frequency moves the singularities into the first and third quadrant of the complex  $k$ -plane. The use of complex frequency has the effect of smoothing the spectrum and enhancing the first motions relative to later arrivals. This effective attenuation is used to minimize the influence of the neighboring fictitious sources introduced by discrete  $k$ . The effect of the imaginary part of the frequency can be removed from the final time domain solution by inverse complex Fourier transform with the complex frequency with the same imaginary part used in the argument of the exponential function in the Fourier transform. The magnitude of the imaginary part is usually chosen to be,

$$\omega_I = \frac{\pi}{t_{max}} \quad (96)$$

Larger  $\omega_I$  increases the attenuation for later arrivals, but also magnifies the numerical noise for late times. If  $\omega_I$  is chosen too small, the attenuation may not be large enough to damp out the arrivals from the fictitious sources.

## 7. Numerical Electroiseismogram Examples

Four different numerical models are calculated in the *PSVTM* wavefield picture. The first example is a 100 *m* thick porous sand layer sandwiched in between two identical halfspaces that are less porous than the layer. The fluid chemistry is the same in all three layers. The source/receiver medium configuration is depicted in Figure 1. This example is meant to study electroseismic conversions as a result of a change in mechanical properties. Mechanical displacement seismograms and electroseismograms (*TM* mode components) are calculated and displayed in Figure 2. The converted magnetic and electric field amplitude behavior as function of antenna position are determined at three different distances from the mechanical contrast as shown in Figure 3. In Figures 4 and 5, four time evolution snapshots are shown of the mechanical wavefront traversing an interface and the conversion of the mechanical wavefield into the electromagnetic *TM* mode components.

The second example studies the effect of a change in fluid salinity, which only affects mainly the medium's electrical properties, on the conversion to electromagnetic waves. The source/receiver medium configuration is depicted in Figure 6. The mechanical displacement seismograms and electroseismograms (*TM* components) are calculated and displayed in Figure 7. The converted magnetic and electric field amplitude behavior as function of antenna position at three different distances from the electrical contrast are shown in Figure 8. The four snapshots, Figures 9 and 10 in time are calculated to trace in time the converted *TM* wavefield pattern generated by a mechanical wavefront traversing the electrical contrast.

The last two examples show the electroseismic effect in a Vertical Electroseismic Profiling (VESP) setting. The seismic source is located in the upper halfspace and the recording geophone/antennas are positioned vertically crossing two mechanical contrasts in the first VESP example (see Figure 11) and an additional electrical contrast in the second VESP example (see Figure 13).

The modeled mechanical source in all examples is a mechanical explosion source. To model true amplitudes, the diagonal elements in the seismic moment matrix, equation 64, need to be replaced by a realistic value. Using the relation  $m = \frac{4\pi a^3}{3} K_G \Delta\Theta$ , with  $a$  the radius of the of the nonlinear deformation zone around the source,  $K_G$  a coefficient from the deformation equation given in equation 10,  $\Delta\Theta$  the fractional change in volume and  $E = \frac{4\pi a^3}{3} K_G (\Delta\Theta)^2 = \epsilon [4.7 \times 10^6 J/Kg] C$ , with  $E$  the total energy,  $C$  the source weight in kilograms and  $\epsilon$  an efficiency factor expressing the fraction energy converted into sound, the following expression for  $m$  is obtained.

$$m = \sqrt{\frac{4\pi a^3}{3} K_G [4.7 \times 10^6 J/Kg] C \epsilon} \quad (97)$$

In the numerical calculation  $m = 4.4 \times 10^6 J$  is used, corresponding to  $C = 1Kg$ ,  $a = 1m$ ,  $K_G = 10^9 Pa$  and  $\epsilon = 10^{-3}$ .

### 7.1. The Electroseismic Conversion at Mechanical Contrasts

An explosion source is positioned 100  $m$  above the first mechanical contrast in the upper halfspace. Fifteen receivers are positioned symmetrically in a straight horizontal line at

both sides of the source 95 *m* above the interface. The receiver spacing is 10 *m*. The medium parameters of the two halfspaces and the 100 *m* thick sand layer are given in Table I. Based on these medium properties the mechanical fast wave, slow wave, shear wave and electromagnetic *TM* wave velocities are calculated. The complex velocities and calculated bulk conductivities are given in Table II. A slow wave and *TM* wave velocity range is given since these two wave phenomena are diffusive.

When an explosion source is set off only *P* waves are generated in an isotropic poro-elastic medium. Numerically the  $8 \times 1$  displacement-stress-EM wavefield component vector is calculated at each geophone/antenna position. In Figure 2 only the mechanical displacement seismograms ( $u_z$  and  $u_r$  components) and the electroseismograms (*TM* mode components) are shown. All plots are seismogram scaled. The amplitudes of the first 40 *msec* in the  $E_r$  and  $H_\phi$  electroseismograms are multiplied by a factor 50 to enhance the electroseismic converted field generated at the first interface.

At the mechanical contrast the *P* wave reflects as a *P* wave, a converted *SV* wave, and a converted *TM* wave. The direct wave is omitted in all seismograms. The mechanical seismograms show the *PP* reflection and *PSV* conversion generated at the top and bottom of the thick sand layer. The converted *TM* wavefield components show up at all antennas at approximately half the two way *P* wave travel time for normal incidence reflection. Since the *TM* wavefield velocity is at least two orders of magnitude faster than the *P* wavefield (see Table II), the traveltimes spent by the *TM* waves in traveling upward to the antennas

is negligible and the total two way travelttime appears to coincide with the oneway travelttime of the incoming  $P$  wave at normal incidence reflection. The hyperbolas arriving at a later time in the  $E_r$  and  $H_\phi$  electroseismograms have the same travel time as the  $PP$  reflection (compare the mechanical seismogram with the  $E_r$  electroseismogram in Figure 2 and the same travelttime as the  $PSV$  conversion (compare mechanical seismogram with the  $H_\phi$  electroseismogram), respectively.

In the first case the compressional waves traveling through homogeneous porous medium cause pressure gradients which cause charge to separate. This induces within the seismic pulse a system of electric fields that travel with the compressional wave speed. As explained before, the seismic pulse doesn't radiate electromagnetic fields away from the pulse. Therefore when the reflected  $P$  wave pulse passes the antennas an electric field is registered inside the  $P$  wave pulse.

In the second case the vertical polarized rotational mechanical waves traveling through homogeneous porous medium cause grain accelerations, setting up current sheets. This induces within the seismic pulse magnetic fields that travel with rotational mechanical wave speed. Therefore when the converted  $SV$  wave pulse passes the antennas a magnetic field is recorded inside the  $SV$  wave pulse. The electric and magnetic field strengths in the seismic pulse are in this case larger than the converted  $TM$  wavefield components strengths. The  $E_r$  hyperbolas arriving after the electroseismic conversion are associated with the electric fields inside the  $P$  wave pulse traveling with fast wave velocity. While the  $H_\phi$  hyperbolas arriving

after the electroseismic conversion are associated with the magnetic fields inside the *SV* wave pulse traveling with *S* wavespeed velocity. The *TM* conversions from the bottom mechanical contrast have amplitudes which are too small to be identified in the electroseismogram with the scaling used.

In Figure 3 the converted electric and magnetic absolute field amplitudes versus antenna offsets are shown at 20, 50 and 95 *m* from the interface. The field amplitude at each antenna position is determined by calculating a root mean square amplitude inside an estimated pulse window in the time domain. The converted *TM* wavefield, driven by the seismic pulse frequency is diffusive, the real and imaginary parts of the *TM* velocity are almost equal, and therefore the largest signals are measured by antennas closest to the interface. The frequency content of the electromagnetic field is the same as the frequency content of the incident seismic wave. Since we are in the,  $\frac{\sigma}{\omega\epsilon} \gg 1$ , conducting medium regime we can find a skindepth  $\delta = \sqrt{\frac{2}{\omega\mu_0\sigma}}$ , with  $\mu_0 = 4\pi \times 10^{-7}$  henry/*m* the permeability of the medium (Kong, 1990). If the propagation distance is much less than the skindepth, the near field of the radiating interface, then the frequency content in the mechanical and electromagnetic fields are the same. The increase in amplitude with increasing source-antenna offset and a later decay in amplitude with offset show similarities with amplitudes that would be recorded if the interface was replaced by a seismically induced electric dipole right under the source (the amplitude drop off results with antenna offset show that the effective source is not a simple dipole but rather a more complicated multipole).



To investigate the  $TM$  wavefield conversions in more detail, snapshots in time are calculated around the first mechanical contrast. In Figures 4 and 5, four successive time snapshots are displayed, showing the mechanical  $u_z$  wavefield component, the top figure, the electromagnetic  $H_\phi$  component, center figure and the electromagnetic  $E_r$  component, bottom figure at 26.6 msec, 28.9 msec, 30.5 msec and 32.0 msec after the shot respectively. The wavefields are determined at 120 by 60 receiver/antenna positions. The receiver/antenna spacings are 1 m in the horizontal direction and 3 m in the vertical direction. At  $t = 26.6$  msec the Ricker wavelet (Hosken, 1988) front has reached the interface at -90 m, see left column in Figure 4. The  $t = 26.6$  msec snapshot displaying the magnetic field component of the  $TM$  mode shows an amplitude radiation pattern of an equivalent magnetic current loop, with a position centered under the seismic source at distance 60 m, with field lines pointing at one side into the paper and at the other side out of the paper. The magnetic field diffuses quickly away from the interface. The  $t = 26.6$  msec snapshot displaying the electric field component of the  $TM$  mode shows an amplitude radiation pattern of an electric dipole, positioned right under the seismic source at a distance 60 m. The largest electric fields are associated with the field inside the  $P$  wave pulse. At later times when a larger part of the seismic pulse has traversed the interface the magnetic current loop diameter increases and the  $TM$  wavespeed differences above and below the interface become visible. The current system imbalances across the interface change in direction in accordance with the pulse polarity, the magnetic and electric field polarities flip accordingly. The last two snapshots show complex patterns of

mechanical field convergences into electromagnetic fields. More than one magnetic current loops appear with alternating field line directions and the inner loop diameter increases. Also more electric dipoles with opposite “dipole type moments” appear there where the wavefront passes. The combined  $E_r$  and  $H_\phi$  amplitude pattern away from the interface has a predominant effective electrical dipole character away from the interface. In both cases the amplitudes decay fast with traveled distance.

## 7.2. The Electro seismic Conversion at Electrical Contrasts

The explosion source is again positioned 100 *m* above an electrical contrast in the upper halfspace. Fifteen receivers are positioned symmetrically in a straight horizontal line at both sides of the source 95 *m* above the interface to record the reflection from the contrast and 95 *m* below the interface to record the transmissions through the contrast. The receiver spacing is 10 *m*. The medium input parameters describing the two halfspaces are given in Table I. The calculated medium velocities and bulk conductivities based on the medium parameters listed in Table I are shown in Table III. In Figure 7 the mechanical displacement seismograms ( $u_z$  and  $u_r$  components) and the electroseismograms ( $TM$  mode components) are shown. All four plots are seismogram scaled. At the electrical contrast the  $P$  wave reflects only as converted  $TM$  waves. Since there is no mechanical contrast, the  $P$  wave doesn't reflect or convert into shear waves. The mechanical  $u_r$  and  $u_z$  seismograms show the transmitted wave fields through the electrical contrast at the geophones 95 *m* below the

interface which are essentially the direct  $P$  wave field from the explosion source in the upper halfspace. The  $TM$  wavefield components are recorded at antennas at approximately the one way  $P$  wave traveltime from source to interface. Since the direct wave in the upper halfspace is omitted, the  $E_r$  wavefield seismogram does not show induced electric fields within the seismic pulse that travel with the compressional wave speed.

In Figure 8 the converted electric and magnetic absolute field amplitudes versus antenna offsets are shown at 20, 50 and 95  $m$  from the interface. An increase in amplitude with increasing source-antenna offset up to a global maximum is observed. When the source-antenna offset is further increased the amplitudes decrease monotonically. The amplitude pattern shows similarities with amplitudes that would be recorded if the interface had been replaced by a seismically induced electric dipole centered right under the seismic source. When Figures 3 and 8 are compared the field amplitude curves have similar shape. The amplitudes however, are a factor 10 bigger for the converted  $TM$  mode generated at the electrical contrast when compared to the converted  $TM$  mode amplitudes converted at the electrical contrast.

In Figures 9 and 10 four successive snapshots in time are displayed, showing the mechanical  $u_z$  wavefield component, top figure, the electromagnetic  $H_\phi$  component, center figure and the electromagnetic  $E_r$  component, bottom figure at 26.6  $msec$ , 28.9  $msec$ , 30.5  $msec$  and 32.0  $msec$  after the shot, respectively. The number of receivers/antennas and their spacings in horizontal and vertical directions are identical to the mechanical contrast case. The top

halfspace has a salinity of  $1.0 \text{ mol/l}$  and the lower halfspace has a salinity of  $0.001 \text{ mol/l}$ . This results in a larger conductivity and lower electromagnetic wavefield velocity in the upper halfspace than in the lower halfspace (see Table III). Therefore the electric fields within the incoming seismic  $P$  wave pulse are small in amplitude when compared to the electric fields within the mechanical  $P$  wave in the lower halfspace. This amplitude behavior can be clearly observed in the electromagnetic  $E_r$  component snapshots. Tracing the transient TM component wavefield pattern fronts in Figures 9 and 10, the  $TM$  wavefield velocity difference in both halfspaces is evident. The complex convergence patterns from mechanical wavefield into electromagnetic  $TM$  fields are similar to the patterns observed around the mechanical contrasts (compare Figures 4 and 5 with 9 and 10). The resultant  $E_r$  and  $H_\phi$  amplitude pattern away from the interface has again a predominant effective electrical dipole character that is centered under the source at the contrast's depth. The amplitudes of the  $TM$  mode transients decay rapidly with traveled distance.

### 7.3. Vertical ElectroSeismic Profiling (VESP)

The converted  $TM$  mode amplitude behavior with distance, discussed when the surface electroseismic calculations were discussed, suggests that the VESP geometry setting is an important one. Since with this technique the antennas are positioned close to the target of interest, larger converted electromagnetic signals can be recorded before they become too attenuated with distance. With the VESP technique the electroseismic method can be

applied to targets, electrical and/or mechanical contrasts, at greater depths.

The first VESP example is a three layer model with the first interface at 300 *m* depth and the second interface at 400 *m* depth. The first receiver/antenna is positioned at a horizontal offset of 50 *m* and a depth of 155 *m*. The receiver/antenna depth spacing is 10 *m*. The medium description with its most important electroseismic medium parameters are shown in Figure 11. In Figure 12 the numerically calculated VESP's are shown. The top plot is the mechanical displacement response, and the center and bottom plots show the  $E_r$  and  $H_\phi$  *TM* mode components, respectively. The top VESP in Figure 12 shows the *P* wave reflections and converted *SV* wave reflection at top and bottom interface of the "sand reservoir." The direct *P* wave in the top halfspace is omitted. The other two vertical electroseismic profiles show the converted *TM* mode components at the two contrasts. The converted *TM* wavefield components show up at all antennas at virtually the same time. The high electrical conductivity in the center layer attenuates the electric field amplitudes completely. The later arrivals in the  $E_r$  VESP are electric fields within the seismic pulse that travel with the compressional wave speed. The  $H_\phi$  component VESP shows the fast decay of the converted electroseismic fields with distance. The converted  $H_\phi$  component of the *TM* mode is much larger in amplitude than the induced magnetic fields inside the *SV* wave pulse. The main reason is the close antenna position to the target of interest.

The last numerical example has a new electrical contrast added to the previous model as is shown in Figure 13. The 100 *m* thick "reservoir sand" is now divided into two sands with

identical mechanical properties saturated with two fluids of different salinity. In Figure 1 the calculated VESP's are shown. The mechanical displacement response is identical to the previous calculation without the electrical contrast. But the *TM* mode component VESP's are modified with an extra electroseismic conversion at the electrical contrast.

## 8. Conclusions

A global matrix method is used which solves the macroscopic equations controlling the coupled electromagnetics and acoustics of porous media numerically in layered poro-elastic media driven by arbitrary seismic point sources. The coupled equations decouple for isotropic porous media into *PSVTM* and a *SHTE* coupled wavefield cases. The induced current motion plane determines to which electromagnetic mode the mechanical waves are coupled. Seismic motion which generates relative flow, induces a 'streaming' electrical current due to flow of double-layer ions. The driving force for the relative flow is a combination of pressure gradients set up by the peaks and troughs of a compressional wave and by grain accelerations. The relative flow and therefore current can be due to either compressional and shear waves, although the two cases are of significant different nature.

Compressional waves traveling through homogeneous porous medium cause pressure gradients which cause charge to separate. This induces within the seismic pulse a system of electric fields that travel with the compressional wavespeed. Rotational waves traveling through a homogeneous porous medium cause grain accelerations and set up current sheets.

This induces within the seismic pulse a detectable magnetic fields that travel with the rotational wavespeed. Therefore when the seismic pulse passes an antenna an electric field is recorded inside the *P* wave pulse and a magnetic field is recorded inside the *S* wave pulse. The seismic pulse doesn't radiate electromagnetic waves away from the pulse.

Radiating electromagnetic wavefields are converted from seismic waves however, when contrasts in mechanical and/or electrical properties are traversed. The principle features of the converted electromagnetic signals are: (1) contacts all antennas at approximately the same time; (2) arrives at the antennas at half of the seismic travel time at normal incidence reflected *P* waves; and (3) changes sign on opposite sides of the shot. The frequency content of the converted electromagnetic field has the same frequency content of the driving incident seismic pulse, as long as the propagation distances are much less than the electromagnetic skin depth. Root mean square converted electromagnetic amplitudes versus seismic point source-antenna offset are calculated for a mechanical porosity contrast and an electrical, salinity contrast at different depths. The amplitude curves are similar in shape, first a strong increase in amplitude to a global maximum is observed with increasing antenna offset and next a monotonic decrease in amplitude with a further increase in antenna offset. The amplitudes decrease rapidly with traveled distance.

Four snapshots in time show the the generation of a converted wavefield there where the seismic wavefront passes the interface creating current imbalances across the interface. Equivalent sources can be identified with the conversion to electromagnetic waves. The

$TM$  component amplitude versus offset curves recorded at some distance from the interface show similarities with the wavefield that would be obtained if the interface was replaced by an equivalent electric dipole positioned right beneath the seismic source at the contrast's depth. The amplitude versus offset results and the electroseismograms confirm such an effective conversion right beneath the source. The VESP modeling shows the rapid decay of the converted electroseismic signals with distance. The antennas close to the target of interest show larger amplitudes in the converted signal than electromagnetic signals inside the seismic pulse. With increasing distance from the contrast seismic pulse, totally dominates in amplitude the converted fields in the electroseismograms with increasing distance from contrast to antenna.

## Acknowledgments

This research was supported by the Department of Energy, Office of Energy Research, grant number DE-FG02 -93ER14322 and by Air Force Research contract no. F19628-93K-0027, monitored by the Phillips Laboratory. We would like to thank Dr. Chengbin Peng for his helpful discussions regarding the Global Matrix Method, Prof. Ted Madden and, Prof. M. Nafi Toksöz, Director and Founder of the Earth Resources Laboratory, where this work was performed.



## References

- Aki, K. and P. Richards, *Quantitative Seismology, Theory and Methods*, vol. 2, W.H. Freeman and Co., New York, 1980.
- Biot, M., Mechanics of deformation and acoustic propagation in porous media, *J. Appl. Phys.*, 33, 1482–1498, 1962.
- Bockris, J. and A.K.N. Reddy, *Modern Electrochemistry*, vol. 2, Plenum Press, 1970.
- Bouchon, M. and K. Aki, Discrete-wavenumber representation of seismic source wavefields, *Bull. Seis. Soc. Am.*, 67, 259–277, 1977.
- Butler, R.D. Russell, A.K. a. M.M. (ed.), *Mapping of a stratigraphic boundary by its seismic response*, Proceedings on the applications of geophysics to engineering and environmental problems (SAGEEP), 1994.
- Chin, R., G. Hedstrom, and L. Thigpen, Matrix methods in synthetic seismograms, *Geophys. J. Roy. Astron. Soc.*, 77, 483–502, 1984.
- Dunkin, J., Computation of modal solutions in layered, elastic media at high frequencies, *Bull. Seis. Soc. Am.*, 55, 335–358, 1965.
- Haskell, N.A., The dispersion of surface waves on multi layered media, *Bull. Seis. Soc. Am.*, 43, 17–34, 1953.
- Hosken, J., Ricker wavelets in their various guises, *First Break*, 6, 25–33, 1988.
- Hudson, J., A quantitative evaluation of seismic signals at teleseismic distances I-radiation from a point source, *Geophys. J. Roy. Astron. Soc.*, 18, 133–249, 1969.

- Kennett, B.L.N. , *Seismic Wave Propagation in Stratified Media*, Cambridge University Press, 1983.
- Kong, J., *Electromagnetic Wave Theory*, Wiley and Sons, Inc., 1990.
- Mal, A., Guided waves in layered solids with interface zones, *Int. J. Eng. Sci.*, 26, 873–881, 1988.
- Mal, A., Wave propagation in layered composite laminates under periodic surface loads, *Wave Motion*, 10, 257–266, 1988.
- Mikhailov, O. and M. Haartsen, Electrostatic investigation of the shallow subsurface: field measurements and numerical modeling (to be submitted), *Geophysics*, 1996.
- Pride, S. and M. Haartsen, Electrostatic wave properties (submitted), *J. Acous. Soc. Am.*, 1995.
- Pride, R.S., A.F. Gangi, and F.D. Morgan, Deriving the equations of motion for porous isotropic media, *J. Acous. Soc. Am.*, 92, 1992.
- Pride, S., Governing equations for the coupled electromagnetics and acoustics of porous media, *Phys. Rev. B*, 50, 15678–15696, 1994.
- Schmidt, H. and G. Tango, Efficient global matrix approach to the computation of synthetic seismograms, *Geophys. J. Roy. Astron. Soc.*, 84, 331–359, 1986.
- Sneddon, I., *Fourier Transforms*, McGraw-Hill, New York, 1951.
- Thompson, A. and G. Gist, Electrostatic prospecting, in *Extended Abstracts of Papers*, pp. 425–427, 61th Annual International Meeting, Society of Exploration Geophysicists,

1991.

Thompson, A. and G. Gist, Geophysical applications of electrokinetic conversion, *The Leading Edge*, 12, 1169–1173, 1993.

Thomson, W.T., Transmission of elastic waves through stratified medium, *J. Appl. Phys.*, 21, 89–93, 1950.

Watson, G.N., *A Treatise on the Theory of Bessel Functions (2nd edition)*, Cambridge University Press, 1966.

## APPENDIX A. ElectroSeismic Field-Vector Formalism with Powerflow Normalized Eigenvectors

In this appendix the electroseismic field-vector-formalism results are given, which are used to calculate the electroseismograms in this paper. The reader is referred to Pride and Haartsen (1995) for the derivation of these results.

A linear transformation of the vector  $\underline{B}^{(PSVTM)}$  is performed, through it, a field-vector-formalism is obtained in which a decomposition of  $\underline{B}^{(PSVTM)}$  into up and downgoing fields is manifest. Let  $\underline{W}^{(PSVTM)}$  be the 8 by 1 vector that is related to  $\underline{B}^{(PSVTM)}$  by the linear transformation,

$$\underline{B}^{(PSVTM)} = \underline{\underline{D}}^{(PSVTM)} \underline{W}^{(PSVTM)}. \quad (\text{A-1})$$

The  $\underline{\underline{D}}^{(PSVTM)}$  is the eigencolumn matrix of system matrix  $\underline{\underline{A}}^{(PSVTM)}$  ( $\frac{\partial}{\partial z} \underline{B} = \underline{\underline{A}} \underline{B}$ ) and

defined as,

$$\underline{\underline{D}}^{(PSVTM)} = \begin{bmatrix} b_J^{(m;-P_f)}, b_J^{(m;-P_s)}, b_J^{(m;-SV)}, b_J^{(m;-TM)}, \\ b_J^{(m;+P_f)}, b_J^{(m;+P_s)}, b_J^{(m;+SV)}, b_J^{(m;+TM)} \end{bmatrix}. \quad (\text{A-2})$$

The  $-$  superscript denotes downgoing eigenvectors and the  $+$  superscript denotes upgoing wavefield eigenvectors. The wavefield eigenvector  $\underline{B}^{(PSVTM)}$  is derived to be,

$$\underline{B}^{(PSVTM)} = [u_x, u_z, w_z, \tau_{xz}, \tau_{zz}, S, H_y, E_x]^T. \quad (\text{A-3})$$

The up and downgoing compressional eigenvectors, bulk displacement normalized, are given in the following matrix:

$$\begin{bmatrix} b_J^{(m;\mp P_f)} \\ b_J^{(m;\mp P_s)} \end{bmatrix}^T = \begin{bmatrix} pv_{p_f} & pv_{p_s} \\ \pm qv_{p_f} & \pm qv_{p_s} \\ \mp \begin{bmatrix} \rho_B - \frac{H}{v_{p_f}^2} \\ \rho_f - \frac{C}{v_{p_f}^2} \end{bmatrix} qv_{p_f} & \mp \begin{bmatrix} \rho_B - \frac{H}{v_{p_s}^2} \\ \rho_f - \frac{C}{v_{p_s}^2} \end{bmatrix} qv_{p_s} \\ \pm 2i\omega pqv_{p_f} G & \pm 2i\omega pqv_{p_s} G \\ \frac{i\omega}{v_{p_f}} \left[ H - 2Gp^2v_{p_f}^2 - \begin{bmatrix} \rho_B - \frac{H}{v_{p_f}^2} \\ \rho_f - \frac{C}{v_{p_f}^2} \end{bmatrix} \right] & \frac{i\omega}{v_{p_s}} \left[ H - 2Gp^2v_{p_s}^2 - \begin{bmatrix} \rho_B - \frac{H}{v_{p_s}^2} \\ \rho_f - \frac{C}{v_{p_s}^2} \end{bmatrix} \right] \\ \frac{i\omega}{v_{p_f}} \left[ C - \begin{bmatrix} \rho_B - \frac{H}{v_{p_f}^2} \\ \rho_f - \frac{C}{v_{p_f}^2} \end{bmatrix} M \right] & \frac{i\omega}{v_{p_s}} \left[ C - \begin{bmatrix} \rho_B - \frac{H}{v_{p_s}^2} \\ \rho_f - \frac{C}{v_{p_s}^2} \end{bmatrix} M \right] \\ 0 & 0 \\ -\frac{i\omega\rho_E Lpv_{p_f}}{\epsilon} \begin{bmatrix} \rho_B - \frac{H}{v_{p_f}^2} \\ \rho_f - \frac{C}{v_{p_f}^2} \end{bmatrix} & -\frac{i\omega\rho_E Lpv_{p_s}}{\epsilon} \begin{bmatrix} \rho_B - \frac{H}{v_{p_s}^2} \\ \rho_f - \frac{C}{v_{p_s}^2} \end{bmatrix} \end{bmatrix} \quad (\text{A-4})$$

with the compressional velocities determined by,

$$\begin{aligned}
\frac{2[HM - C^2]}{v^2} &= \rho_B M + \rho_E \left[ 1 + \frac{L^2 \rho_E}{\epsilon} \right] H - 2\rho_f C \\
&\pm \left[ \left( \rho_B M + \rho_E \left[ 1 + \frac{L^2 \rho_E}{\epsilon} \right] H - 2\rho_f C \right)^2 \right. \\
&\quad \left. - 4(HM - C^2) \left( \rho_E \rho_B \left[ 1 + \frac{L^2 \rho_E}{\epsilon} \right] - \rho_f^2 \right) \right]^{1/2}
\end{aligned} \tag{A-5}$$

The + sign denotes the fast compressional ( $P_f$ ) wavefield velocity,  $v_{pf}$ , and the – sign denotes the slow compressional ( $P_s$ ) wavefield velocity,  $v_{ps}$ .

$$\begin{bmatrix} b_J^{(m;\mp SH)} \\ b_J^{(m;\mp TE)} \end{bmatrix}^T = \begin{bmatrix} 1 & 1 \\ \pm i\omega q G & \pm i\omega q G \\ \mp \frac{i\omega LG q \rho_E}{\rho_f} \frac{\left[ \frac{1}{v_{sh}^2} - \frac{\rho_B}{G} \right]}{\left[ \frac{1}{v_{sh}^2} - \epsilon \mu \right]} & \mp \frac{i\omega LG q \rho_E}{\rho_f} \frac{\left[ \frac{1}{v_{te}^2} - \frac{\rho_B}{G} \right]}{\left[ \frac{1}{v_{te}^2} - \epsilon \mu \right]} \\ -i\omega LG \mu \frac{\rho_E}{\rho_f} \frac{\left[ \frac{1}{v_{sh}^2} - \frac{\rho_B}{G} \right]}{\left[ \frac{1}{v_{sh}^2} - \epsilon \mu \right]} & -i\omega LG \mu \frac{\rho_E}{\rho_f} \frac{\left[ \frac{1}{v_{te}^2} - \frac{\rho_B}{G} \right]}{\left[ \frac{1}{v_{te}^2} - \epsilon \mu \right]} \end{bmatrix} \tag{A-6}$$

The up and downgoing shear and  $TM$  wavefield eigenvectors, bulk displacement normalized,

are given in the following matrix:

$$\begin{bmatrix} b_J^{(m;\mp SV)} \\ b_J^{(m;\mp TM)} \end{bmatrix}^T = \begin{bmatrix} \pm q v_{sv} & \pm q v_{tm} \\ -p v_{sv} & -p v_{tm} \\ -\frac{p v_{sv} G}{\rho_f} \left[ \frac{1}{v_{sv}^2} - \frac{\rho_B}{G} \right] & -\frac{p v_{tm} G}{\rho_f} \left[ \frac{1}{v_{tm}^2} - \frac{\rho_B}{G} \right] \\ i\omega v_{sv} [q^2 - p^2] G & i\omega v_{tm} [q^2 - p^2] G \\ \mp 2i\omega q p v_{sv} G & \mp 2i\omega q p v_{tm} G \\ 0 & 0 \\ -\frac{i\omega L G \rho_E}{v_{sv} \rho_f} \left[ \frac{\frac{1}{v_{sv}^2} - \frac{\rho_B}{G}}{\frac{1}{v_{sv}^2} - \epsilon\mu} \right] & -\frac{i\omega L G \rho_E}{v_{tm} \rho_f} \left[ \frac{\frac{1}{v_{tm}^2} - \frac{\rho_B}{G}}{\frac{1}{v_{tm}^2} - \epsilon\mu} \right] \\ \mp i\omega q v_{sv} L G \mu \frac{\rho_E}{\rho_f} \left[ \frac{\frac{1}{v_{sv}^2} - \frac{\rho_B}{G}}{\frac{1}{v_{sv}^2} - \epsilon\mu} \right] & \mp i\omega q v_{tm} L G \mu \frac{\rho_E}{\rho_f} \left[ \frac{\frac{1}{v_{tm}^2} - \frac{\rho_B}{G}}{\frac{1}{v_{tm}^2} - \epsilon\mu} \right] \end{bmatrix} \quad (\text{A-7})$$

with the shear and  $TM$  wavefield velocities determined by,

$$\begin{aligned} \frac{2}{v^2} &= \frac{\rho_B - \rho_f^2 / \rho_E}{G} + \epsilon\mu_0 + L^2 \rho_E \mu_0 \\ &\pm \left[ \left[ \frac{\rho_B - \rho_f^2 / \rho_E}{G} - (\epsilon\mu_0 + L^2 \rho_E \mu_0) \right]^2 - 4 \frac{\rho_f^2 L^2 \mu_0}{G} \right]^{1/2} \end{aligned} \quad (\text{A-8})$$

The + sign denotes the shear ( $SV$ ,  $SH$ ) wavefield velocity and the - sign denotes the  $EM$  wavefield velocity. If a normalization by vertical power flow is preferred the following normalization factors for each wave type need to be used.

#### The SV and TM vertical power flux

$$\langle S_z \rangle = \frac{\omega^2}{4} G \left[ \left( \frac{qv}{v^*} + \frac{q^* v^*}{v} \right) \left( \frac{G\mu}{\rho_f^2} \rho_E \rho_E^* L L^* \gamma_T \gamma_T^* + 1 \right) \right] \quad (\text{A-9})$$

### The $P_f$ and $P_s$ vertical power flux

$$\langle S_z \rangle = \frac{\omega^2}{4} \left[ \left( \frac{qv}{v^*} + \frac{q^*v^*}{v} \right) (H + (\gamma_L + \gamma_L^*)C + \gamma_L\gamma_L^*M) \right] \quad (\text{A-10})$$

### The SH TE vertical power flux

$$\langle S_z \rangle = \frac{\omega^2}{4} \left[ (q^* + q) \left( \frac{\rho_E \rho_E^*}{\rho_f^2} LL^* \mu \gamma_T \gamma_T^* G + 1 \right) \right] \quad (\text{A-11})$$

where  $\gamma_T$  and  $\gamma_L$  are defined as,

$$\gamma_T = - \frac{\left[ \frac{1}{v^2} - \frac{\rho_B}{G} \right]}{\left[ \frac{1}{v^2} - \epsilon \mu \right]} \quad (\text{A-12})$$

$$\gamma_L = - \frac{\left[ \rho_B - \frac{H}{v^2} \right]}{\left[ \rho_f - \frac{C}{v^2} \right]} \quad (\text{A-13})$$

To obtain the normalization with respect to time-averaged Poynting power perpendicular to the plane wave front, we dot Eq (A-9) or (A-10) into the real part of the wave direction vector, which is  $Re[pv, 0, qv]$ . The velocity  $v$  determines which eigenvector wave type is meant,  $*$  denotes the complex conjugate and  $q$  is the vertical slowness and  $p$  is the horizontal slowness of a wave type. With  $\epsilon$  the electric permittivity and  $\mu$  the magnetic permeability. The electrokinetic coupling coefficient  $L(\omega)$  used in Eq (A-4), (A-5), (A-7), and (A-8) is defined in Pride (1994).

TABLE I. The mechanical contrast and the electrical contrast medium properties.

Property	Top and bottom halfspaces	Sand layer	Fresh water halfspace	Brine halfspace
porosities ( $\phi[\%]$ )	15	30	15	15
dc permeability ( $k[m^2]$ )	$10^{-12}$	$10^{-12}$	$10^{-12}$	$10^{-12}$
bulk modulus solid ( $k_s[Pa]$ )	$3.6 \times 10^{10}$	$3.6 \times 10^{10}$	$3.6 \times 10^{10}$	$3.6 \times 10^{10}$
bulk modulus fluid ( $k_f[Pa]$ )	$2.2 \times 10^9$	$2.2 \times 10^9$	$2.2 \times 10^9$	$2.2 \times 10^9$
frame bulk modulus ( $k_{fr}[Pa]$ )	$9.9 \times 10^9$	$9.9 \times 10^9$	$9.9 \times 10^9$	$9.9 \times 10^9$
frame shear modulus ( $g_{fr}[Pa]$ )	$9.0 \times 10^9$	$9.0 \times 10^9$	$9.0 \times 10^9$	$9.0 \times 10^9$
fluid viscosity ( $\eta[Pa \cdot s]$ )	$1.0 \times 10^{-3}$	$1.0 \times 10^{-3}$	$1.0 \times 10^{-3}$	$1.0 \times 10^{-3}$
density solid ( $\rho_s[Kg/m^3]$ )	$2.7 \times 10^3$	$2.7 \times 10^3$	$2.7 \times 10^3$	$2.7 \times 10^3$
density fluid ( $\rho_f[Kg/m^3]$ )	$1.0 \times 10^3$	$1.0 \times 10^3$	$1.0 \times 10^3$	$1.0 \times 10^3$
salinity ( $C[mol/l]$ )	$1.0 \times 10^{-3}$	1.0	$1.0 \times 10^{-3}$	1.0
temperature ( $T[K]$ )	298	298	298	298
permittivity ( $\kappa_f$ )	80	80	80	80
permittivity ( $\kappa_s$ )	4	4	4	4
tortuosity ( $\alpha_\infty$ )	3	3	3	3



TABLE II. Calculated complex wavefield velocities and bulk conductivities used in the mechanical contrast model. The diffusive slow wave and *EM* wavefield velocities are listed at zero and source center frequency (200 *Hz*). The real and imaginary parts of the fast and shear waves are listed.

Properties	Upper and lower halfspace	Sand reservoir layer
fast wave velocity[m/s]	(3282.62, -0.1037)	(3158.56, -0.7419)
slow wave velocity[m/s]	(21.2/146.2, -13.3/-119.1)	(16.7/111.6, -10.5/-100.3)
shear wave[m/s]	(1769.14, -1.39)	(1669.25, -1.53)
<i>TM</i> wave velocity[m/s]	(318890/2.04 10 <sup>6</sup> , -201223/-2.02 10 <sup>6</sup> )	(7159/45665, -4517/ -45326)
conductivity ( $\sigma$ [S/m])	0.000388	0.77

TABLE III. Calculated complex wavefield velocities and bulk conductivities used in the electrical contrast model. The diffusive slow wave and *EM* wavefield velocities are listed at zero and source center frequency (200 *Hz*). The real and imaginary parts of the fast and shear waves are listed.

Properties	Top fresh water saturated halfspace	Bottom brine saturated halfspace
fast wave velocity[m/s]	(3282.62, -0.1037)	(3282.62, -0.1037)
slow wave velocity[m/s]	(21.2/146.2, -13.3/-119.1)	(21.2/146.1, -13.3/-119.1)
shear wave[m/s]	(1769.14, -1.39)	(1769.14, -1.39)
<i>TM</i> wave velocity[m/s]	(318890/2.04 10 <sup>6</sup> , -201223/-2.02 10 <sup>6</sup> )	(10124/64580, -6389/-64100)
conductivity ( $\sigma$ [S/m])	0.000388	0.385

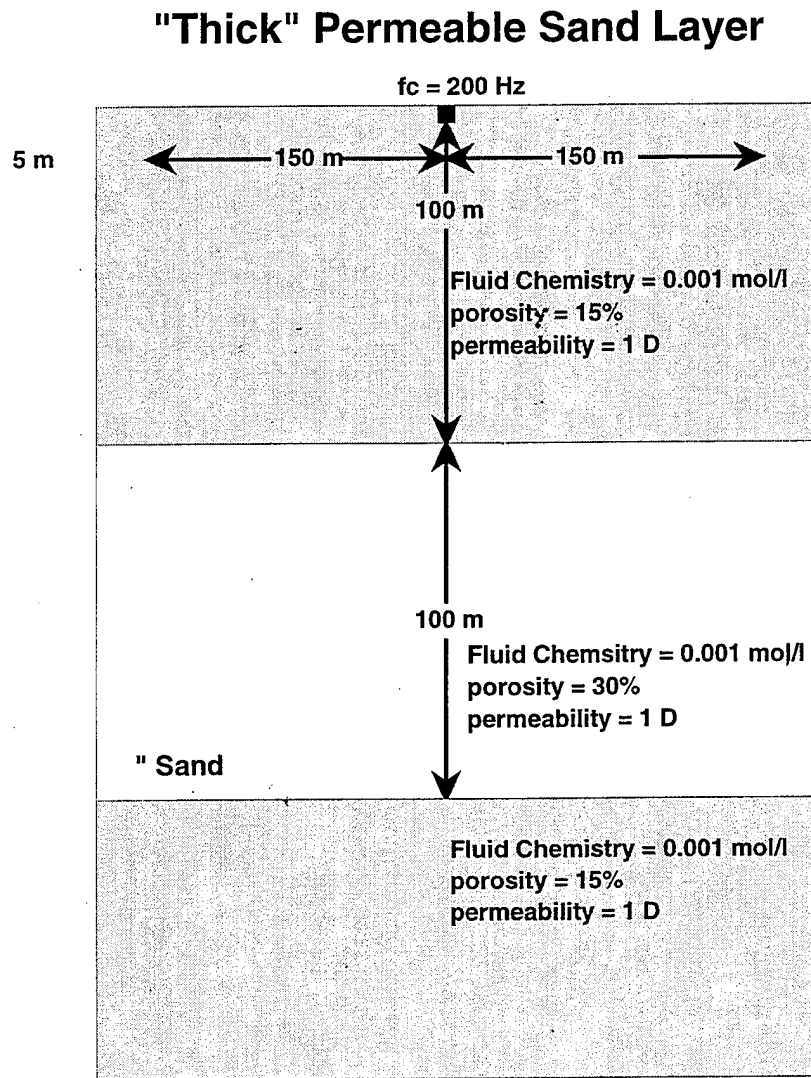


Figure 1: The thick, relative to the mechanical wavelength, permeable sand medium configuration.

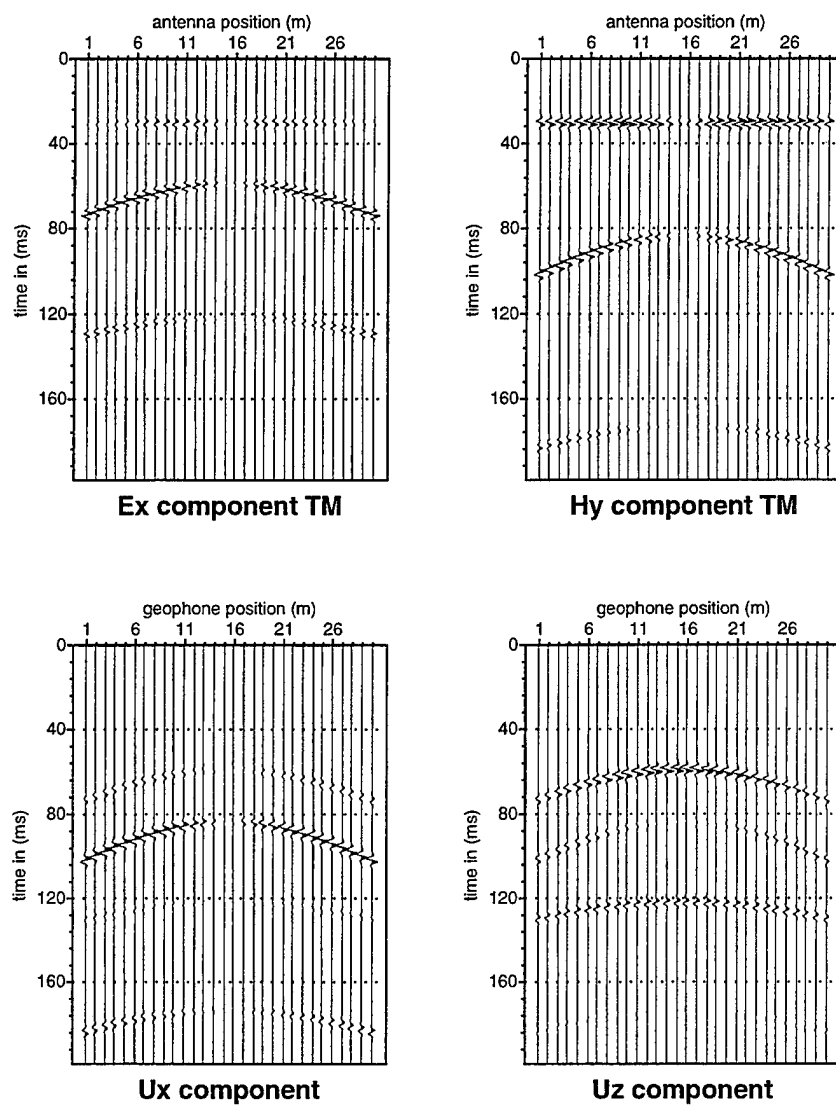


Figure 2: The mechanical displacement component seismograms and the  $TM$  mode component electroseismograms calculated for the thick permeable sand medium configuration.

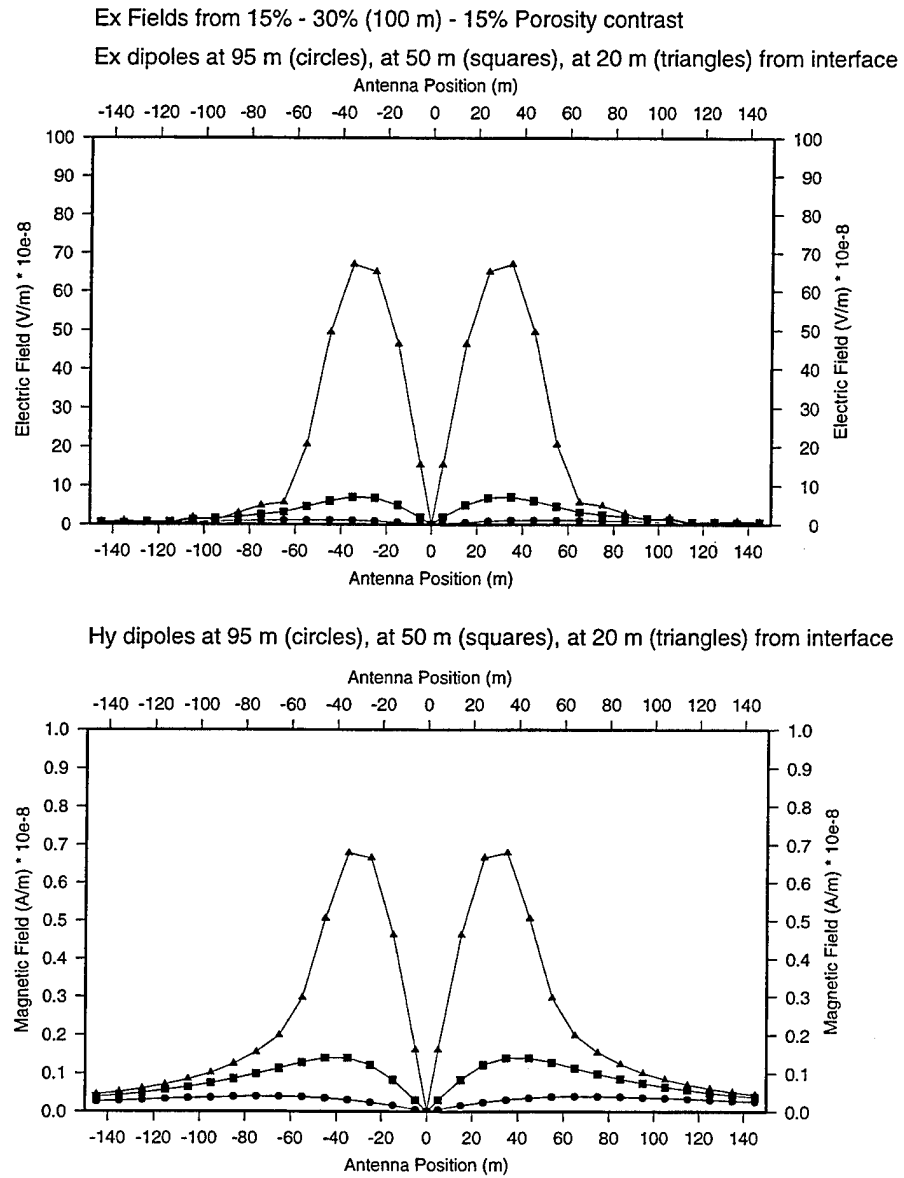
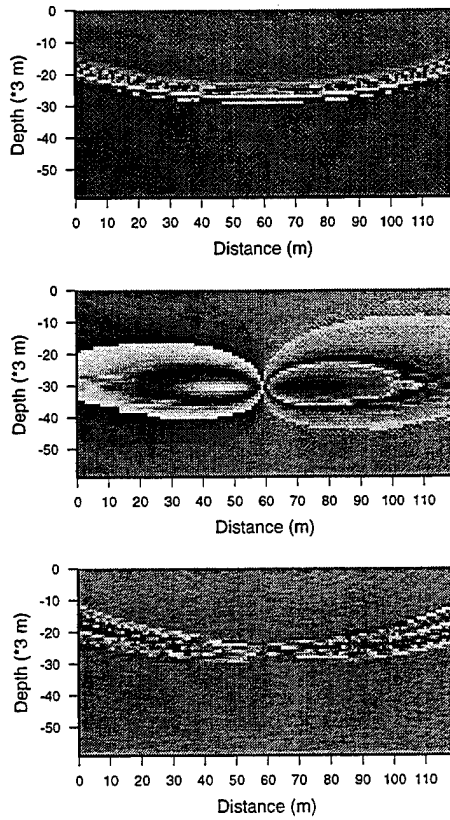


Figure 3: Converted electric and magnetic root mean square wavefield amplitudes versus antenna offsets calculated at 20, 50 and 95 m from a mechanical contrast generated by an explosive point source.

Time slice  $t = 26.6$  msec, wavefield components  $U_z$ ,  $H_y$  and  $E_x$



Time slice  $t = 28.9$  msec, wavefield components  $U_z$ ,  $H_y$  and  $E_x$

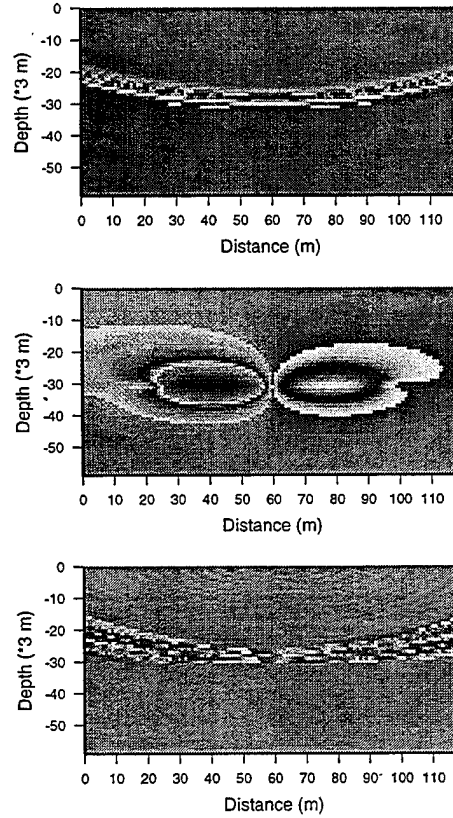
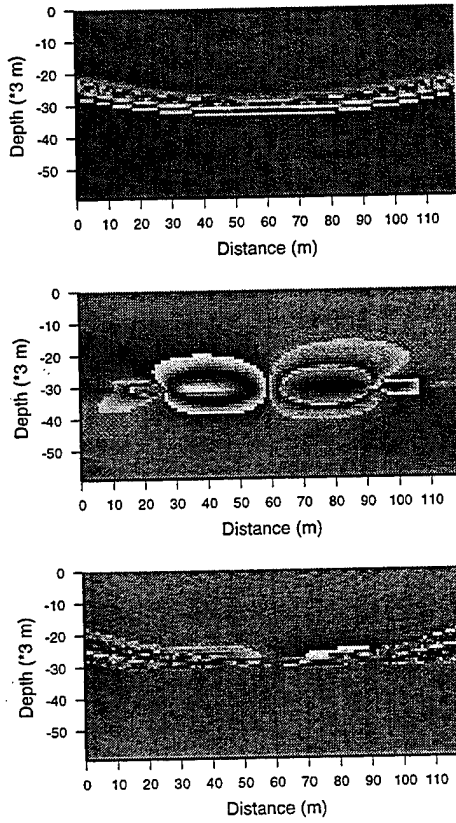


Figure 4: Time slice snapshots calculated at 120 by 60 geophone/receiver positions around a mechanical contrast at  $t = 26.6$  msec and  $t = 28.9$  msec after explosion. Top snapshot is  $u_z$  component of mechanical displacement wavefield, center snapshot is  $H_\phi$  component of electromagnetic  $TM$  mode, bottom snapshot is  $E_r$  component of electromagnetic  $TM$  mode. The complementary coloring of the electromagnetic field snapshots indicate the polarity reversal at opposite sides of the snapshot.

Time slice  $t = 30.5$  msec, wavefield components  $U_z$ ,  $H_y$  and  $E_x$



Time slice  $t = 32.0$  msec, wavefield components  $U_z$ ,  $H_y$  and  $E_x$

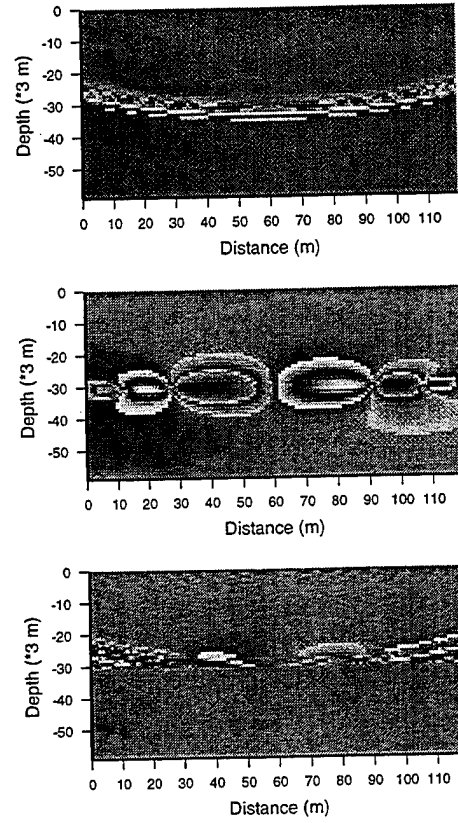


Figure 5: Time slice snapshots calculated at 120 by 60 geophone/receiver positions around a mechanical contrast at  $t = 30.5$  msec and  $t = 32.0$  msec after explosion. Top snapshot is  $u_z$  component of mechanical displacement wavefield, center snapshot is  $H_\phi$  component of electromagnetic  $TM$  mode, bottom snapshot is  $E_r$  component of electromagnetic  $TM$  mode. The complementary coloring of the electromagnetic field snapshots indicate the polarity reversal at opposite sides of the snapshot.

## Fresh Water / Brine

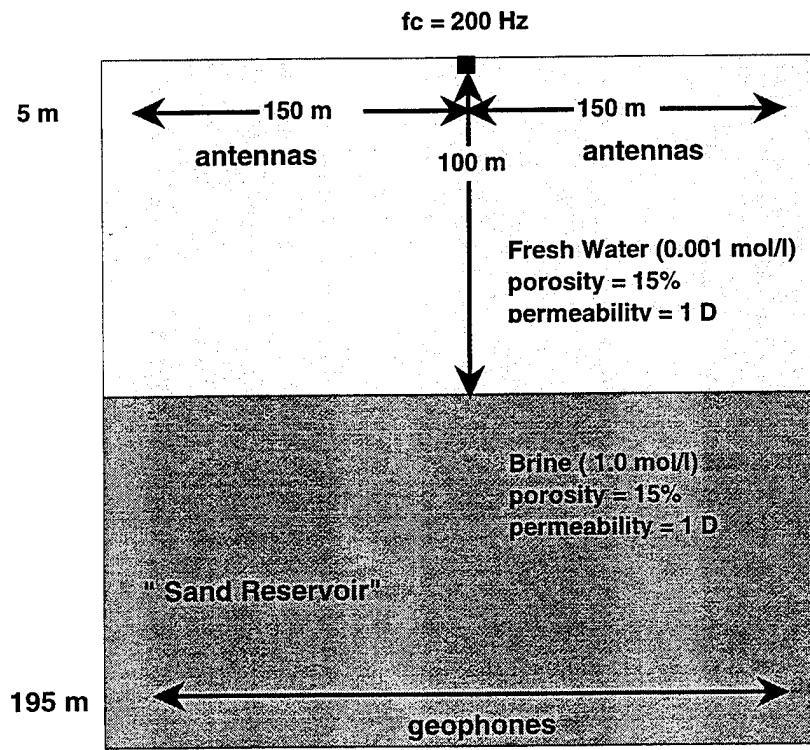


Figure 6: The fresh water-brine medium configuration.



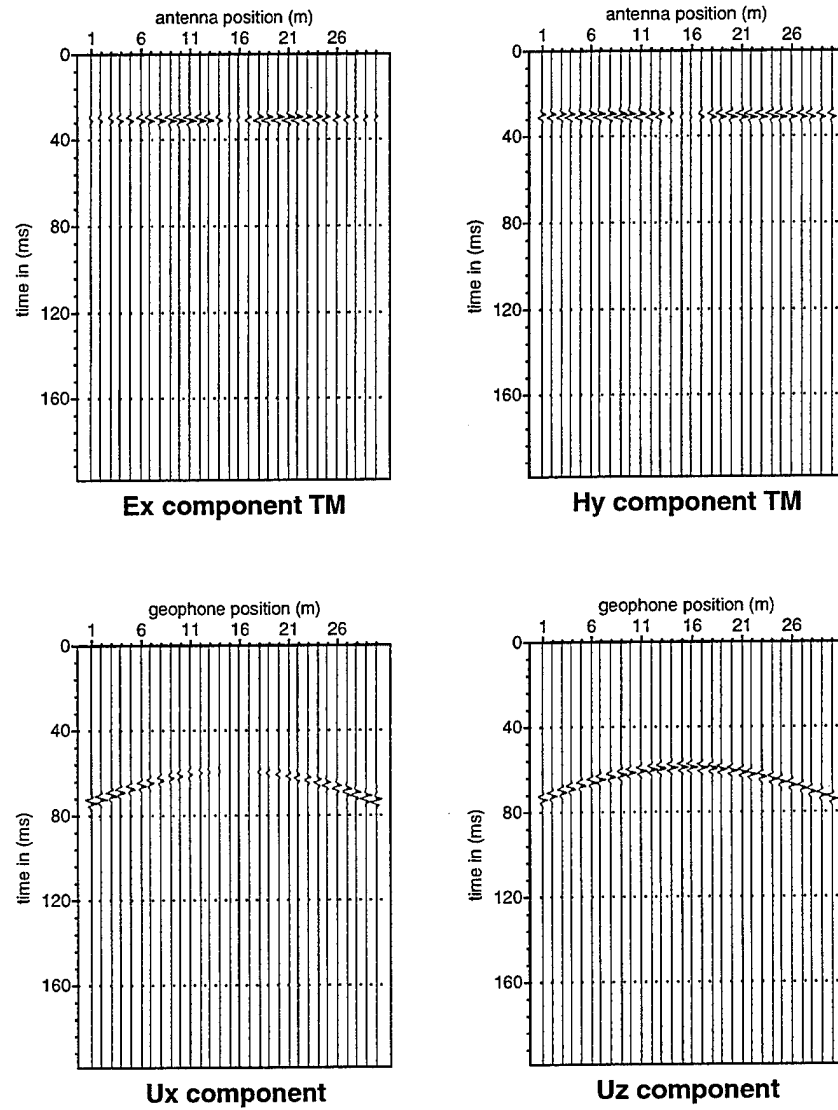


Figure 7: The mechanical displacement component seismograms and the  $TM$  mode component electroseismograms calculated for the fresh water - brine medium configuration.

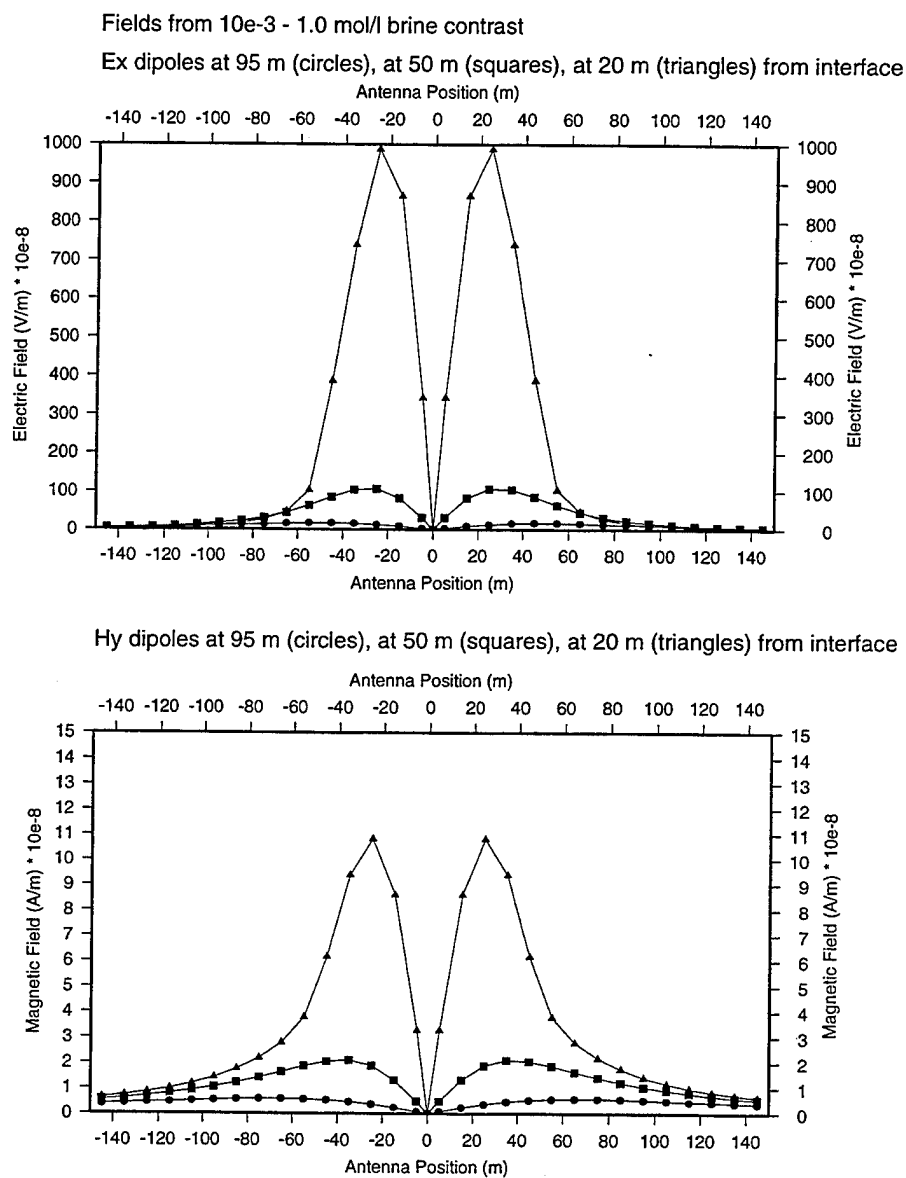
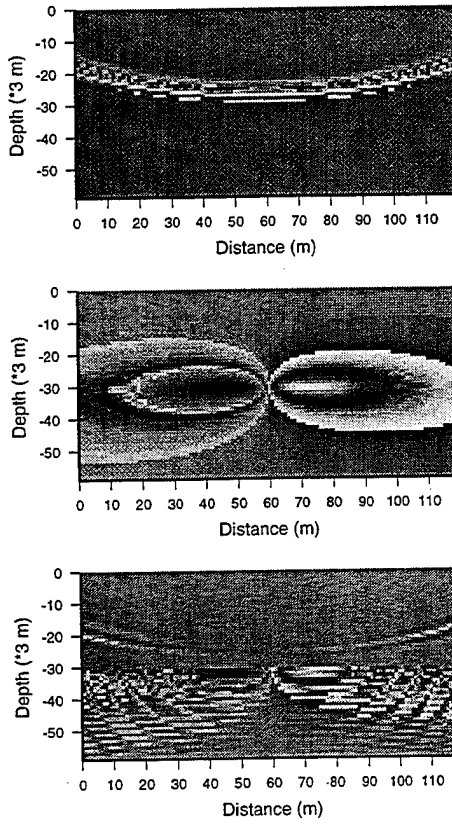


Figure 8: Converted electric and magnetic root mean square wavefield amplitudes versus antenna offsets calculated at 20, 50 and 95 m from an electrical contrast generated by an explosive point source.

Time slice  $t = 26.6$  msec, wavefield components  $U_z$ ,  $H_y$  and  $E_x$



Time slice  $t = 28.9$  msec, wavefield components  $U_z$ ,  $H_y$  and  $E_x$

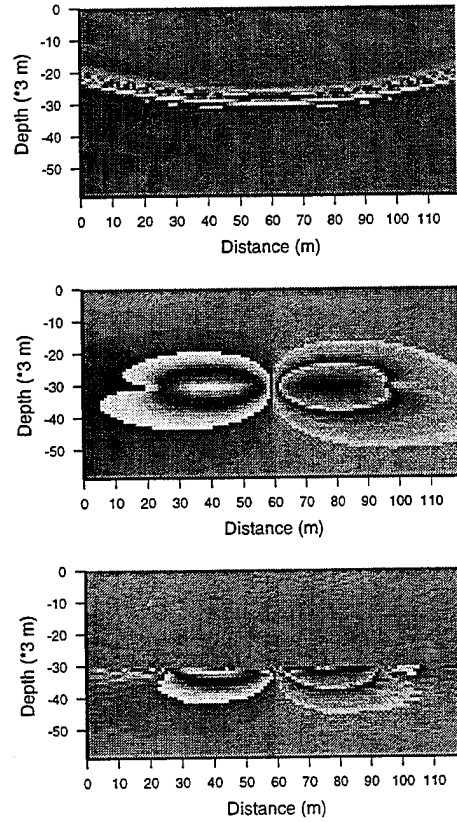
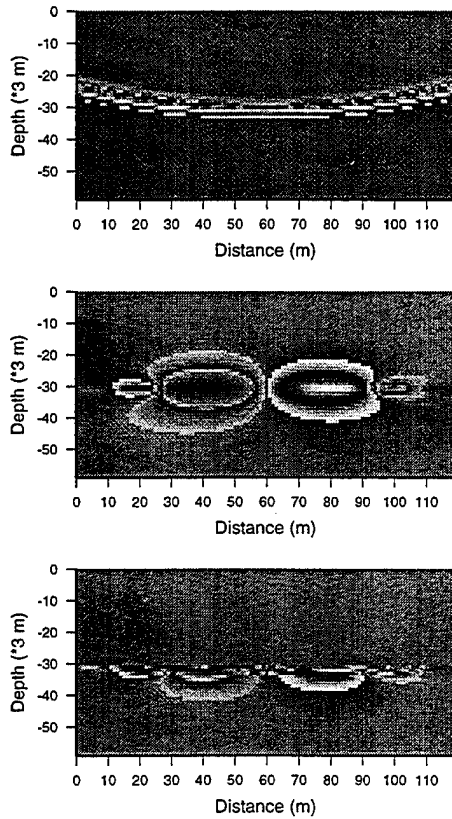


Figure 9: Time slice snapshots calculated at 120 by 60 geophone/receiver positions around an electrical contrast at  $t = 26.6$  msec and  $t = 28.9$  msec after explosion. Top snapshot is  $u_z$  component of mechanical displacement wavefield, center snapshot is  $H_\phi$  component of electromagnetic  $TM$  mode, bottom snapshot is  $E_r$  component of electromagnetic  $TM$  mode. The complementary coloring of the electromagnetic field snapshots indicate the polarity reversal at opposite sides of the snapshot.

Time slice  $t = 30.5$  msec, wavefield components  $U_z$ ,  $H_y$  and  $E_x$



Time slice  $t = 32.0$  msec, wavefield components  $U_z$ ,  $H_y$  and  $E_x$

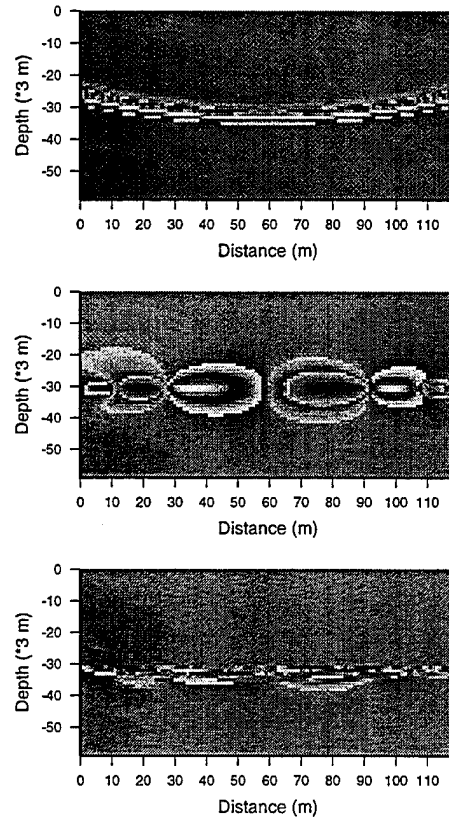


Figure 10: Time slice snapshots calculated at 120 by 60 geophone/receiver positions around an electrical contrast at  $t = 30.5$  msec and  $t = 32.0$  msec after explosion. Top snapshot is  $u_z$  component of mechanical displacement wavefield, center snapshot is  $H_\phi$  component of electromagnetic  $TM$  mode, bottom snapshot is  $E_r$  component of electromagnetic  $TM$  mode. The complementary coloring of the electromagnetic field snapshots indicate the polarity reversal at opposite sides of the snapshot.

## Vertical ElectroSeismic Profiling (VESP)

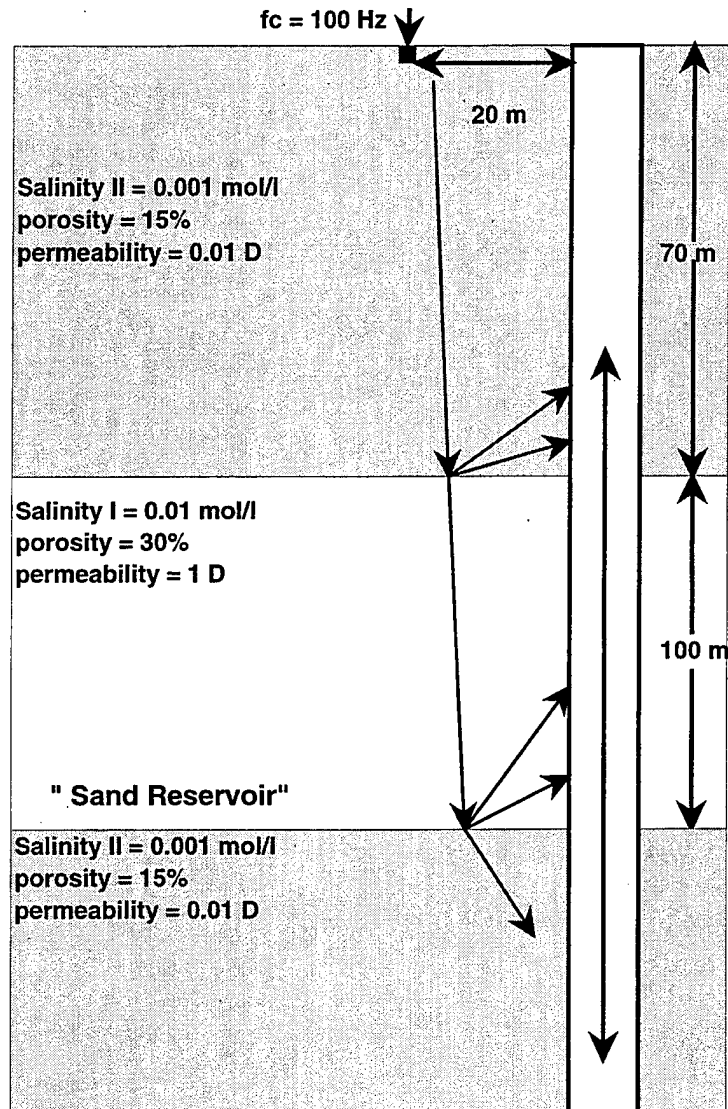


Figure 11: Vertical ElectroSeismic Profiling medium configuration.

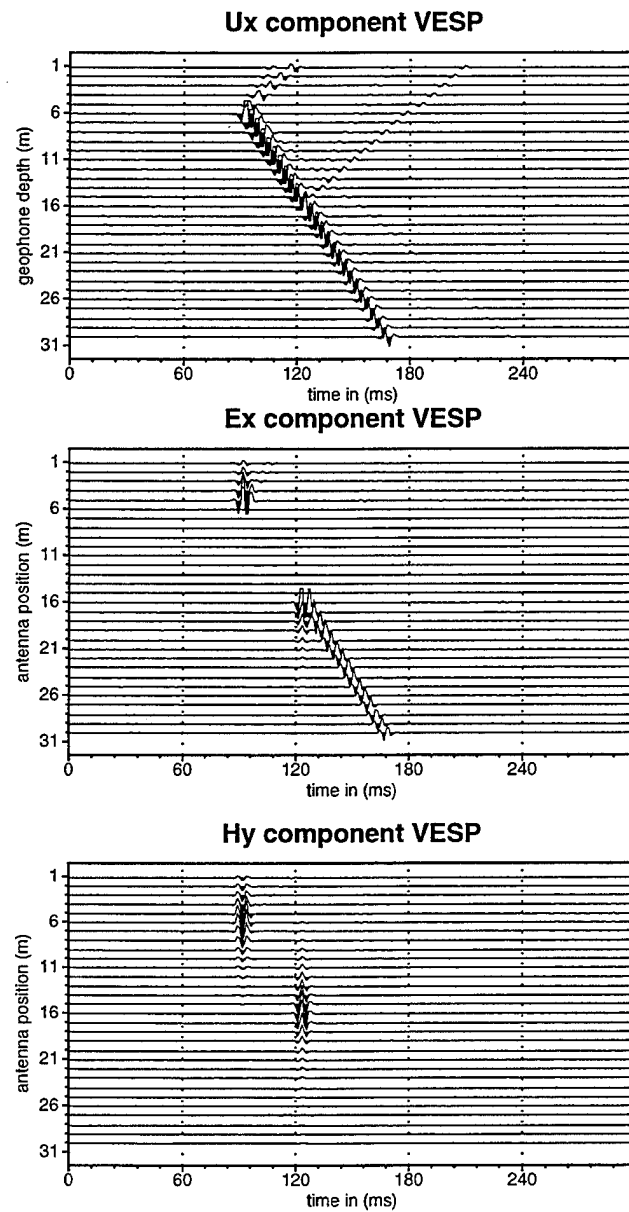


Figure 12: The mechanical displacement component seismogram and the  $TM$  mode component electroseismograms calculated for a Vertical ElectroSeismic Profiling medium configuration.

## Vertical ElectroSeismic Profiling (VESP)

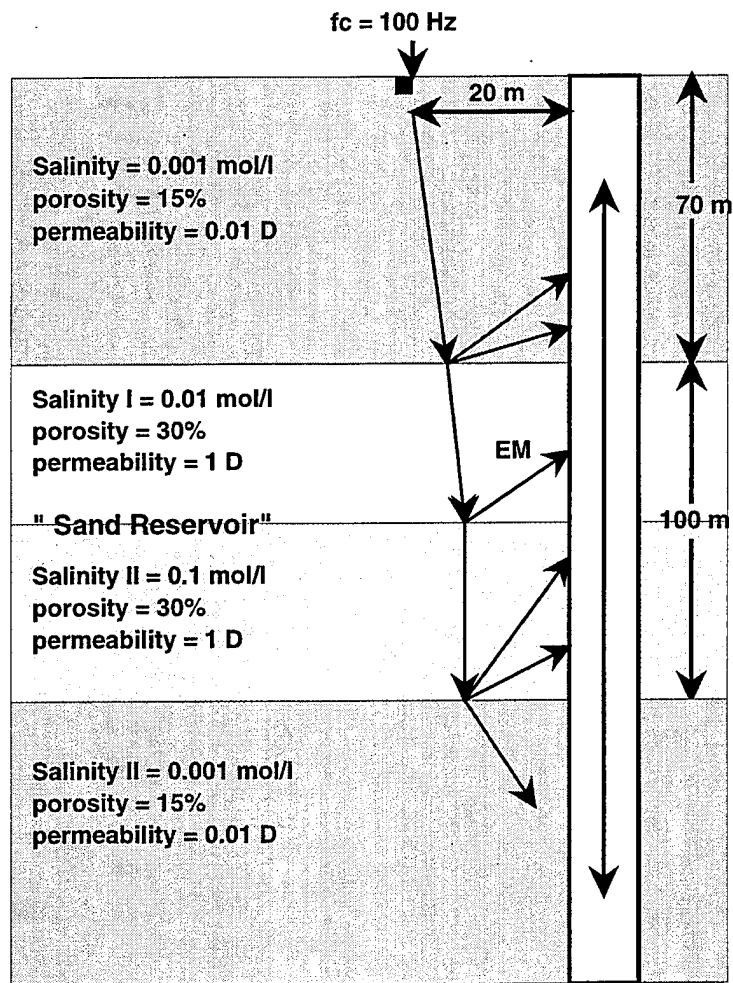


Figure 13: Vertical ElectroSeismic Profiling medium configuration with additional electrical contrast.

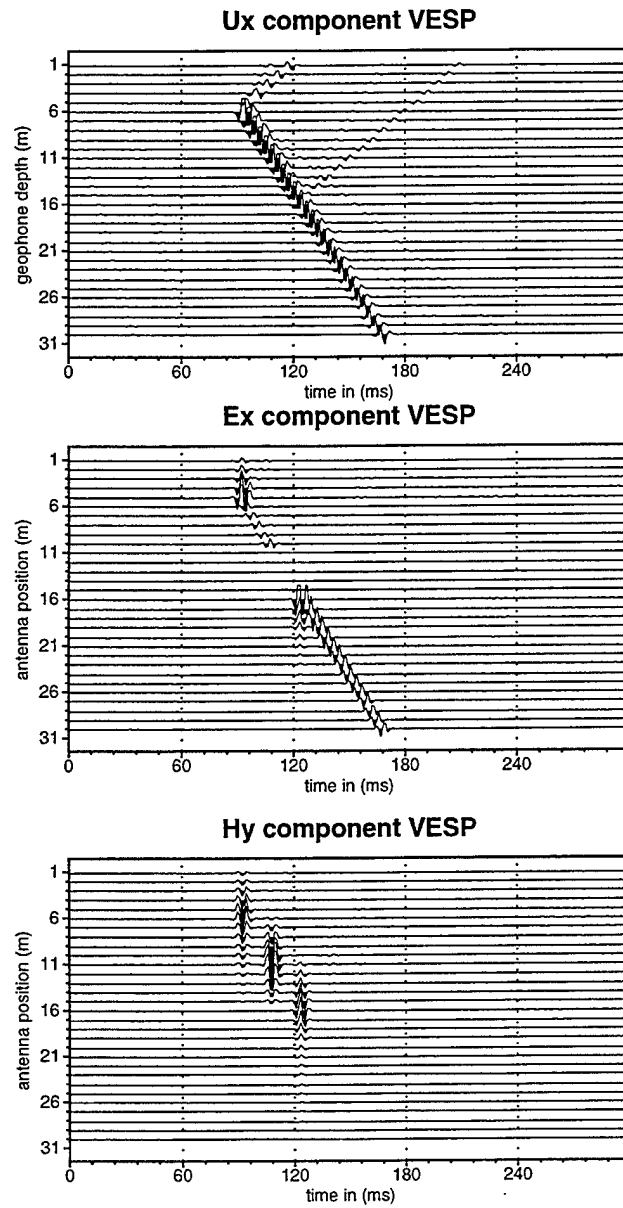


Figure 14: The mechanical displacement component seismogram and the  $TM$  mode component electroseismograms calculated for a Vertical ElectroSeismic Profiling medium configuration with additional electrical contrast inside the sand reservoir.



Defense Technical Information Center  
8725 John J. Kingman Road  
Ft Belvoir, VA 22060-6218  
(2 copies)

Phillips Laboratory  
ATTN: PL/SUL  
3550 Aberdeen Avenue SE  
Kirtland AFB, NM 87117-5776 (2 Copies)

David T. Borup  
Techniscan, Inc.  
958 West Levoy Drive  
Suite 210  
Salt Lake City, UT 84123

Steven J. Cardimona  
Phillips Laboratory/GPE  
29 Randolph Road  
Hanscom AFB, MA 01731

Jim Chang  
AFOSR/NA  
110 Duncan Ave.  
Suite B115  
Bolling AFB, DC 20332-0001

Anthony J. Devaney  
Northeastern University  
Department of Elec.  
c/o Computer Engineering  
Boston, MA 02115

Leopold Felsen  
Boston University  
Dept. of Aerospace & Mech. Eng.  
110 Cummington Street  
Boston, MA 02215

Robert J. Greaves  
MIT/Earth Resources Laboratory  
42 Carleton Street  
Cambridge, MA 02142 (8 Copies)

Russell S. Harmon  
United States Army  
Research Office  
Research Triangle Park, NC 27709-2211

Steven A. Johnson  
Techniscan, Inc.  
958 West Levoy Drive  
Suite 200  
Salt Lake City, UT 84123

Phillips Laboratory  
ATTN: TSML  
5 Wright Street  
Hanscom AFB, MA 01731-3004

Warren Barrash  
Boise State University  
1910 University Drive  
CGISS, MG206  
Boise, ID 83725

Dwain K. Butler  
United States Army  
Eng. Waterways Exp. Station  
3909 Halls Ferry Road  
Vicksburg, MS 39180

Lawrence Carin  
Polytechnic University  
Six Metro Tech Center  
Brooklyn, NY 11201

John O. Curtis  
United States Army  
Eng. Waterways Exp. Station  
3909 Halls Ferry Road  
Vicksburg, MS 39180

Earl V. Edris  
United States Army  
Eng. Waterways Exp. Station  
3909 Halls Ferry Road  
Vicksburg, MS 39180

Ben G. Fitzpatrick  
North Carolina State University  
Box 8205  
Raleigh, NC 27695-8205

Brian J. Harkins  
Rome Laboratory/ERCS  
31 Grenier Street  
Hanscom AFB, MA 01731-3010

Donald E. Hunton  
Phillips Laboratory/GPID  
29 Randolph Road  
Hanscom AFB, MA 01731-3010

Katharine Kadinsky-Cade  
Phillips Laboratory/GPE  
29 Randolph Road  
Hanscom AFB, MA 01731-3010

Rosemary J. Knight  
University of British Columbia  
129-2219 Main Mall, U.B.C.  
Vancouver, B.C. V6T 1Z4

John F. Lennon  
Rome Laboratory/ERC  
31 Grenier Street  
Hanscom AFB, MA 01731-3010

Richard A. Marr  
Rome Laboratory/ERCS  
31 Grenier Street  
Hanscom AFB, MA 01731-3010

Rex Morey  
Applied Research Associates  
Box 120A, Waterman Road  
South Royalton, VT 05068

John B. Morris  
Rome Laboratory/ERCS  
31 Grenier Street  
Hanscom AFB, MA 01731-3010

Jack Murphy  
S-CUBED  
Maxwell Laboratory  
11800 Sunrise Valley Dr., Suite 1212  
Reston, VA 22091

Bruce Nielson  
Armstrong Laboratories/EQW  
139 Barnes Drive  
Suite 2  
Tyndall AFB, FL 32403-5323

Gary R. Olhoeft  
Colorado School of Mines  
Dept. of Geophysics  
1500 Illinois Street  
Golden, CO 80401-1887

Jeff W. Rish III  
Wright Laboratory/FIVCO-OL  
139 Barnes Drive  
Suite 2  
Tyndall AFB, FL 32403-5323

Martin L. Smith  
New England Research  
76 Olcott Drive  
White River Junction, VT 05001

Victor F. Labson  
U.S. Geological Survey  
Box 25046 Federal Center  
MS 964  
Denver, CO 80225

James F. Lewkowicz  
Phillips Laboratory/GPE  
29 Randolph Road  
Hanscom AFB, MA 01731-3010

Lisa M. Mockapetris  
Rome Laboratory/ERCE  
31 Grenier Street  
Hanscom AFB, MA 01731-3010

Dale F. Morgan  
MIT/Earth Resources Laboratory  
42 Carylton Street  
Bldg. E34-462  
Cambridge, MA 02142

Saba Mudaliar  
Rome Laboratory/ERC  
Arcon Inc.  
31 Grenier Street  
Hanscom AFB, MA 01731-3010

Arje Nachman  
AFOSR/NA  
110 Duncan Ave.  
Bolling AFB, DC 20332

Boston College Office of Research Administration  
140 Commonwealth Ave  
Middlesex County  
Chestnut Hill, MA 02167

George C. Papanicolaou  
Stanford University  
Department of Math  
Stanford, CA 94305

Lt Brent C. Roberts  
Armstrong Laboratory/EQ-OL  
Environics Directorate  
139 Barnes Drive, Suite 2  
Tyndall AFB, FL 32403-5323

William W. Symes  
Rice University  
6100 S. Main Street  
Houston, TX 77005

Roelof J. Versteeg  
University of Connecticut  
354 Mansfield Road  
Storrs, CT 06269-2045

Yun Wang  
Armstrong Laboratory/OES  
8308 Hawks Road  
Brooks AFB, TX 78235

I.J. Won  
Geophex, Ltd.  
605 Mercury Street  
Raleigh, NC 27603-2343

David L. Wright  
U.S. Geological Survey  
MS 964, Box 25046  
Federal Center  
Denver, CO 80225

Arthur D. Yaghjian  
Rome Laboratory/ERCS  
31 Grenier Street  
Hanscom AFB, MA 01731-3010